Fall 2016

Transient CFD simulations of pumping and mixing using electromagnetic

Fangping Yuan

Department: Mechanical and Aerospace Engineering

TRANSIENT CFD SIMULATIONS OF PUMPING AND MIXING USING ELECTROMAGNETIC/LORENTZ FORCE IN MICROFLUIDICS

by

FANGPING YUAN

A DISSERTATION

Presented to the Faculty of the Graduate School of the

MISSOURI UNIVERSITY OF SCIENCE AND TECHNOLOGY

In Partial Fulfillment of the Requirements for the Degree

DOCTOR OF PHILOSOPHY

in

AEROSPACE ENGINEERING

2016

Approved
Dr. Kakkattukuzhy M. Isaac, Advisor
Dr. Cheng Wang
Dr. Edward C. Kinzel
Dr. Kelly Homan
Dr. Matt Insall

ABSTRACT

In this dissertation, two dimensional and three dimensional, transient CFD simulations are conducted to investigate the active pumping and mixing in microfluidics driven by Electromagnetic/Lorentz force. Shallow disk/ring cylindrical microfluidic cell and shallow cuboid microfluidic cell with electrodes deposited on the bottom surface are modelled for mixing and pumping purposes respectively. By applying voltage across specific pair of electrodes, an ionic current is established in the weak conductive liquid present in the cell. The current interacts with an externally applied magnetic field generating a Lorentz force that causes fluid motion in the cell. Velocity vectors, electric potential distributions and ionic current lines are presented with high resolution in post-processing techniques. By switching on and off a pair of electrode, a “blinking vortex” is generated to induce the chaotic advection so as to enhance the mixing quality. Various particle trajectories based analyses using extensive post-processing of the simulation results show that the period T plays an important role in generating chaotic advection. Conducting polymer modified electrodes in microfluidics are also modeled and studied to build the bridge between the electrochemical properties of conducting polymer film and MHD flow manipulations in microfluidics. This dissertation establishes CFD simulation of MHD flow as a robust tool to study pumping and mixing in a microfluidic cell. The techniques developed in the present work are also applicable in MHD flow control in microfluidics.

ACKNOWLEDGMENTS

First, I would like to express my gratitude to my advisor, Dr. Kakkattukuzhy M. Isaac who guided me patiently through my doctoral program. He advised me not only on how to conduct research properly from the general ideas to the details in a figure, but also on the daily life in a foreign country. Without his motivation, help and support, I cannot finish my program and this dissertation. Also it was great to have him as one of the witness of my marriage here.

I would also thank to my committee members, Dr. Cheng Wang, Dr. Edward C. Kinzel, Dr. Kelly Homan and Dr. Matt Insall for their kind discussions and advices. I would also like to thank to Department of Mechanical and Aerospace Engineering at Missouri S&T and NSF grants for the support during my doctoral program. Special thanks to Ms. Katherine Wagner, Cathy Williams and the staff, faculty at MAE department for their invaluable help everywhere.

Finally, I want to thank to God who brought my beautiful wife Yao Cheng to my life. Without her encouragement and support, I will not succeed. Most importantly, I would like to thank to my wonderful parents who always stand by my side and support me, without their love none of these would be possible.

TABLE OF CONTENTS

LIST OF ILLUSTRATIONS

Page

LIST OF TABLES

Page

1. INTRODUCTION

1.1. MICROFLUIDICS/LAB ON A CHIP

In recent years, there is a growing interest in lab-on-a-chip (LOAC) devices which hold promise in revolutionizing the diagnosis of illnesses, personalizing medical treatment, detection of chemicals in the environment, and synthesis of materials [1]. In many of these applications, the core purpose is to accomplish pumping, mixing and flow control functions. Among them, efficient and rapid mixing is an especially important task since it has an effect on chemical reaction rates when multiple species are present for purposes such as medical diagnostics and chemical detection by chemical reactions, which are often mass transfer limited. However, due to the small size of these devices which are usually of centimeter or even millimeter order, the flows are always laminar and turbulent mixing techniques would not be applicable.

1.2. MIXING IN MICROFLUIDICS

Fortunately, there is a variety of approaches that can be implemented to enhance mixing in lab-on-a-chip. Generally, these strategies can be categorized as either passive or active methods [2]. Passive micro-mixers are designed to use specific channel geometry configurations to increase the interface between the different constituents [3-5], while active ones are designed to control the flow by introducing non-intrusive driving forces or by actuating mechanical components to introduce flow patterns that would result in more efficient mixing. However, equally due to the small size of these applications, it becomes a real challenge to rely on moving mechanical components because of manufacturing complexity, high manufacturing cost and the increased likelihood of mechanical failures. Therefore, to introduce driving forces by other means to move fluid along desired trajectories to enhance mixing would be desirable. Electrostatic force and electromagnetic force are two main types of non-intrusive driving forces that have been widely studied in recent years. Compared to electromagnetic force, electrostatic force usually requires a higher voltage to produce the same order of flow rate. Furthermore, significant Joule heating, bubble generation and electrode erosion are also the major drawbacks of the electrostatic technique. Electromagnetic force, namely

the Lorentz force, provides a simple and flexible means to manipulate fluid flow in small devices, and the main requirement is that the fluid should be slightly conductive which can be easily met by most biological and chemical solutions [6].

1.3. WHAT IS MHD (MAGNETO-HYDRODYNAMICS)

Electromagnetic or Lorentz force takes advantage of the interaction between the electric current *j* and the external magnetic field *B*. The resulting electromagnetic or Lorentz force can be written as $F_{\mathrm{L}} = j \times B$. Therefore, in fluid flows, the Lorentz force is treated as a body force similar to the gravitational force. Using electromagnetic force to manipulate fluid flow is by no means new. Magneto-hydrodynamics (MHD) has been used in the past for pumping and flow control of highly conductive liquid metals and plasma [7]. In recent years, it has also been used to induce flow in weakly conductive electrolyte solution in redox (reduced species-oxidized species) MHD based systems. Electrochemical MHD based on redox electrode reactions has advantages such as negligible Joule heating and the absence of bubble generation. Experiments and CFD simulations show that the flow velocities of μm/s or even mm/s are feasible by applying electric potential of ~1V and magnetic flux density B ~0.5T [8-12]. Undoubtedly, using electromagnetic force becomes an effective tool to manipulate flow in LOAC devices.

1.4. THE CONCEPT OF MIXING AND STIRRING

Before we discuss how to improve mixing by using MHD in microfluidics, it is important to clarify the mechanisms underlying the terms “stirring” and “mixing.” Generally speaking, the two phrases “stirring” and “mixing” imply very different physical processes. As Eckert observed in 1948 [13], advection alone increases the mean value of any initial gradient, and this effect of advection is appropriately called stirring. On the other hand, the effect of conduction or diffusion is to decrease the mean value of the gradient, and this is called mixing. Viscosity tends to slow down stirring which leads to increased mixing [14]. In other words, if we want to mix two initially separated constituents by stirring, the early stage of the process should be dominated by advection to stretch and fold the fluid elements to increase the interface area between two constituents to increase the concentration gradient and then allow mixing to take place by

diffusion which will reduce the concentration gradient [15]. Researchers find it very insightful to use these two phrases to distinguish the “larger-scale” and “molecular-scale” processes that underlie mixing. Now the question is how to efficiently stir the fluid before molecular diffusion can smoothen the gradients. The first answer immediately comes to mind is to make the flow turbulent. Indeed, for large scale mixing, turbulent flow that provides the chaotic motion is useful and efficient. However due to the small size of the micro LOAC devices we study here, turbulent flow would not develop; instead a turbulent-like laminar flow which can produce similar chaotic motion would be of interest. This behavior of laminar flow is implied by the term “chaotic advection.”

The term “chaotic advection” was first introduced some thirty years ago by Aref as an outgrowth of the work on interacting point vortices in incompressible inviscid fluid [16]. A point vortex agitator inside a circular domain along with its image on the wall provided an unsteady potential flow. With the agitator being fixed at a certain position, the system is integrable and regular, and the system does not stir very efficiently. If, on the other hand, the agitator is moved in such a way (blinks between left and right repeatedly) that the potential flow is unsteady, chaotic motion can be induced and the system can stir very efficiently. This manner of agitation, now called “blinking vortex,” is a very simple way to produce chaotic motion, and has been the inspiration for many subsequent chaotic advection studies. Following Aref’s model, another model, the “journal bearing flow” has been widely investigated by experiments and numerical simulations by Aref [17], Swanson and Ottino [18] and Chaiken et al [19]. The devices are made up of an outer and inner cylinder that can rotate successively with a time period, and the process is repeated for several periods. With a specific range of time periods and rotation speeds, chaotic motion can be generated. Yet another type called “cavity flows” has been studied by Chien et al [20]. The “cavity flows” model relates to a two dimensional rectangular device with moving upper and lower walls which are switched on and off to start or stop successively with a time period, and the process is repeated for several periods. The common feature of the above three models is that they fall under potential flow [16] and Stokes flow [17-20], and their two dimensional flow fields can be exactly obtained by analytical tools. Once the velocity field is obtained, particle trajectories-based analyses can be conducted to investigate chaotic motion. The on/off

switching scheme is a simple way to produce an unsteady flow. The investigators of the above studies recognized that the two dimensional kinematics of advection by an incompressible flow is equivalent to the Hamiltonian dynamics of a one degree of freedom system which has been well understood as chaotic since the mid-1960s. These observations have helped build the theoretical bridge between chaotic advection in fluid mechanics and chaos in classical mechanics.

1.5. MHD CHAOTIC MIXING

It is not surprising that chaotic advection driven by electromagnetic force in microfluidics has been studied in the past decade since Lorentz force provides the possibility to manipulate fluid flow in a controlled manner instead of moving mechanical agitators or walls. Yi et al [21] perhaps were the first group to the best of our knowledge to study chaotic advection by using electromagnetic force. They investigated a microscale cylindrical cell with its axial dimension much smaller than the diameter. Switching the positions of the point electrodes placed on the bottom surface could produce the "blinking vortex" in their MHD stirrer. The governing equations under the Stokes flow and quasi-steady assumptions were solved and compared to their experiments. They also studied several rectangular ducts with electrodes deposited on the bottom or side walls to trigger chaotic motion by using switching schemes [22,23]. Another interesting work has been done by Rossi et al [24]. They conducted experiments in a small flat rectangular cell with a magnet moving underneath. By doing so, three typical flow sequences were created, and lamination, stretching and mixing performance were investigated. Dufour et al [25] performed experiments in a shallow cavity and compared their results to those using linearized equations under the Stokes flow assumption. Gopalakrishnan and Thess [26] studied glass melt homogenization by stirring and mixing of flow in a pipe mixer subjected to electromagnetic forces by using computational methods. Yuan and Isaac [27] studied mixing in microfluidics by chaotic advection by applying a sinusoidal potential difference across the electrodes by performing unsteady, two-dimensional CFD simulations. They found that off-axis placement of the working electrode cylinders and using various switching schemes made the flow more chaotic and enhanced mixing.

1.6. MHD REDOX SYSTEM AT CONDUCTING POLYMER MODIFIED ELECTRODE

As mentioned, it is by no means new to rely on the interaction between ionic current and magnetism to manipulate fluid flow. Several techniques including Magnetohydrodynamics, Ferrohydrodynamics, Magnetorheology and Magnetophoresis, among others, have been studied widely [6]. Lorentz force can be used in weakly conductive electrolyte solutions for pumping and mixing purposes in a controlled manner in microfluidics [28, 29]. In weakly conductive solution, the electric current path is completed with the ionic current due to ion movement through convection, diffusion and migration. However, due to the weak conductivities of commonly used biological and chemical solutions, the magnitude of ionic current is very small so is the resulting Lorentz force under an external magnetic field. And in order to obtain a higher electric current density, higher applied voltage is used but with the side effect of causing bubble generation and electrode degradation which is undesirable in chemical detection and analysis. Fortunately, this problem was solved by introducing additional redox species into the solution which allows it to generate high ionic current density with lower applied voltage and thus avoids bubble generation and electrode degradation [30, 31]. In the redox solution electrochemical system, the conversion between the oxidizer and reducer species at electrode surface leads to a species concentration gradient which contribute to the ionic current [8, 10, 32]. However, concerns of interaction of redox species with detection or undesirable chemical reaction have arisen.

In order to avoid the interference of redox species with detection and undesirable chemical reactions and still maintain the high electric current in the solution, one way is to confine the redox species on the surface of electrode [33]. Coincidentally, conducting polymer has recently become a promising candidate for solid capacitors, chemical sensors and field effect transistors because of its outstanding electrochemical properties, stability and high electrical conductivity [34-36]. Conducting polymer can be prepared by either traditional oxidative chemical or electrochemical polymerization in both aqueous and organic solutions, and the thickness can be controlled by number of growth cycles or the deposition time [37]. The conducting polymer film can be switched between its conducting state and neutral state by electrochemical methods and the bond conjugation

along the polymer backbone is responsible for its electrical conductivity [38]. Because of these promising properties, conducting polymer becomes a great candidate as surface confined redox material. Due to the high concentration of electroactive species inside the film, conducting polymer modified electrodes generates a much higher current density compared with bare electrodes in weakly conductive solutions, however, the trade-off is that the duration of electric current is shorter due to the limited total charge [33].

In recent years, a large number of studies including theoretical modeling and experiments have been conducted to investigate the electrochemical properties of conducting polymers including polythiophenes, polypyrrole and poly(3-4-ethylenedioxythiophene) et al. Generally, there are two major ways to establish models to study conducting polymers. One is to model governing equations to describe the fundamental mechanisms of ionic transport and electron transport inside the polymer films. For example, one is called multilayer model introduced by Laviron in which the polymer film is divided into several sublayers and homogeneous electron exchange reaction take place between the sublayers [39]. A porous polymer electrode model with capacitive current was introduced by Yeu et al, in which ion and electron transport inside and out of the porous polymer film are both taken into account [40]. Later, a conformational relaxation model was introduced by Otero et al to interpret the voltammetric behavior of polypyrrole and it is also applicable to other conducting polymers [41]. On the other hand, equivalent circuit models which use classic electronic elements such as capacitors and resistances to fit the electrochemical behavior of polymer modified electrodes is also widely studied. However, for different polymer films investigated by different groups, the equivalent circuit models can differ including different types of circuit elements used and their arrangement in the circuit [42-44].

1.7. RESEARCH STATEMENT

Since two-dimensional Stokes flow can be solved analytically, many researches therefore relied on this assumption to study the chaotic advection and mixing performance in microfluidics [15-18, 21]. However, three-dimensional full Navier-Stokes flow should reflect more insights, and more chaotic advection should be found in it because the nonlinear term in full Navier-Stokes flow should indicate more chaos.

Therefore, in this dissertation, a three-dimensional full Navier-Stokes model with MHD is established to study the pumping and mixing in microfluidics. Full Navier-Stokes flow model and Stokes flow model are compared to see the difference between them. Trajectories based analysis is then relied on to investigate the chaotic advection quantitatively once flow field is obtained by solving the three-dimensional full Navier-Stokes equations. Furthermore, the finite size of the electrodes deposited on the bottom surface of the microfluidic cell may affect the flow field and the trajectories based results compared with those by assuming point electrodes and agitators.

Though conducing polymer film is widely studied in recent years, researches are primarily focusing on fabrications and electrochemical properties of the conducting polymer. The applications of this kind of film are lack of investigating. In the second part of this dissertation, another three-dimensional full Navier-Stokes model is developed to study the MHD pumping and mixing using film-confined Redox system (conducting polymer film). This model is to connect the electrochemical properties of the conducting polymer film and MHD induced flow using conducting polymer-modified electrodes in microfluidics.

1.8. ORGANIZATION OF THIS DISSERTATION

This dissertation consists of two main parts, modeling of MHD chaotic advection and modeling of MHD flow manipulation with conducting polymer modified electrode.

The dissertation is organized as follows. Chapter two presents the mathematical models and governing equations of the electrochemical MHD flow system. Chapter three presents the results of 2D and 3D chaotic advection. Chapter four presents the results of modeling of conducting polymer modified electrode and future work.

2. MATHEMATICAL MODEL

2.1. OVERVIEW

This section presents the full mathematical model for the MHD flow system including the electric current and electric potential in the aqueous solution, the governing equations of fluid flow and species transport.

2.2. ELECTRIC CURRENT AND POTENTIAL IN THE SOLUTION

The Lorentz force is the cross product between the electric current in the solution and the external magnetic field. Therefore, it is important to model the electric current in the solution first. This section briefly describes the mathematical model of electric current and electric potential in the solution with excessive supporting electrolyte. The mass transfer is governed by the Nernst-Planck equation for the flux, N_i, of species, i,

$$\bar{N}_i = C_i\bar{V} - D_i\bar{\nabla}C_i - z_i\frac{F}{RT}D_iC_i\bar{\nabla}\phi \qquad i = 1, 2, ..., I \tag{2.1}$$

where C is the concentration, D is the diffusivity, $\bar{V}$ is the velocity vector, ϕ is the electric potential, F is the Faraday constant, R is the universal gas constant, T is the absolute temperature, and z is the charge number. Subscript i stands for the species. Eqn. (2.1) shows that there are three contributions to mass transfer: convection, diffusion and migration, represented by the first, second and the third term in eqn. (2.1), respectively. The current flux density is proportional to the sum of the fluxes of the charge-carrying species. It can be easily shown that convection does not contribute to the current flux under the condition of electroneutrality, a common assumption in electrochemistry. Further, since the present model is for the fluid domain outside the double layer, the potential at the outer edge of the double layer is used for the boundary condition, the only significant contribution to current in the bulk solution is due to migration represented by the third term in eqn. (2.1). Thus, the equation for current flux simplifies to

$$\bar{J} = \bar{\nabla}\phi\underbrace{\frac{F^2}{RT}\sum_i z_i^2 D_i C_i}_{-\sigma} \tag{2.2}$$

where σ is the electrical conductivity. When a magnetic field is applied, it will induce an electric field, and the equation for the current flux will be modified as

$$\overline{J} = \sigma(-\overline{\nabla}\phi + \overline{V} \times \overline{B}) \tag{2.3}$$

where $\overline{B}$ is the magnetic field intensity vector, and the second term on the right-hand-side of eqn. (2.3) represents the induced electric field. In this study we consider the model where the applied electric field gradient $\nabla\phi$ is ~1 V/cm, the maximum velocity is ~10 mm/s, and the applied magnetic field intensity is ~1 T. For these values, the induced electric field is approximately 4 orders of magnitude less than the applied field, and can be neglected.

The electric potential in the bulk solution satisfies the Laplace equation

$$\nabla^2\phi = 0 \tag{2.4}$$

once appropriate boundary conditions of potential are specified, the electric potential on the whole computation domain can be obtained.

Note that the electric potential ϕ for the electrode boundary condition in the simulations is the electric potential at the outer edge of the double layer. The electrical double layer is a very thin layer (~1 to ~100nm thick) across which the electric potential drops dramatically. By using Gouy-Chapman Theory and Poisson-Boltzman equation, we calculate the potential at the outer edge of the double layer to specify the electrode boundary condition to solve eqn. (2.4). The ionic concentrations around a central ion is assumed to be related to the potential by the Boltzmann distribution

$$c_i = c_i^* \exp\left(-\frac{z_i F\phi}{RT}\right) \tag{2.5}$$

where c_i^* is the average concentration of species *i* in the electrolyte solution, and ϕ is the electrostatic potential established around the central ion. The product $z_i F\phi$ is the electric interaction energy per mole; other contributions to the interaction energy are ignored. Poisson's equation relates the potential variation to the charge density. The potential distribution has contributions from other ions which is described by Poisson's equation

$$\nabla^2\phi = -\frac{\rho_e}{\varepsilon} = -\frac{F}{\varepsilon}\sum_i z_i c_i = -\frac{F}{\varepsilon}\sum_i z_i c_i^* \exp\left(-\frac{z_i F\phi}{RT}\right) \tag{2.6}$$

For the double layer we use the one-dimensional form of Poisson's equation.

$$\frac{d^2\phi}{dx^2} = -\frac{F}{\varepsilon}\sum_i z_i c_i^* \exp\left(-\frac{z_i F\phi}{RT}\right) \tag{2.7}$$

where x is the distance from the electrode. The boundary conditions are

$$\phi = \phi_0 \quad \text{at} \quad x = 0 \tag{2.8}$$

and

$$\frac{d\phi}{dx} \to 0 \quad \text{as} \quad x \to \infty \tag{2.9}$$

The solution to equation (10) with the boundary conditions, equations (11) and (12), is

$$\frac{\tanh(K\phi)}{\tanh(K\phi_0)} = \exp(-\kappa x) \tag{2.10}$$

where $K = Fz/(4RT)$ and $\kappa = \left(2F^2/\varepsilon RT\right)^{1/2} z\sqrt{c^*}$, z is the magnitude of the charge number, ε is the permittivity of the medium, and T is the temperature. For dilute aqueous solutions, the ratio of the permittivity to the permittivity of free space at 25°C, $\varepsilon/\varepsilon_0$ = 78.49. Substituting for the constants, we get the following expression for κ (cm^{-1}).

$$\kappa = 0.329\times10^8 z\sqrt{c^*} \tag{2.11}$$

where c^* is in M (moles/liter). Using this model, we estimated $\phi = 0.0379\text{V}$ at the outer edge of the double layer with c* = 0.1M, x = 1 nM (10^{-7} cm), and externally applied potential ϕ_0 = 1V, indicating a ~96% potential drop in the double layer. Because it is only an estimate, we rounded off ϕ to 0.04V. Our approach appears to be reasonable based on satisfactory agreement with reported experiments.

2.3. ELECTROMAGNETIC/LORENTZ FORCE

The electromagnetic/Lorentz force is defined as the cross product of the electric current and magnetic flux density. The corresponding mathematical form without the induced electric current can be written as

$$\bar{F}_{\mathrm{L}} = \bar{J} \times \bar{B} = -\sigma \bar{\nabla} \phi \times \bar{B} \tag{2.12}$$

2.4. NAVIER-STOKES AND SPECIES TRANSPORT EQUATIONS

In this dissertation, incompressible Newtonian fluid flow is considered, and therefore the velocity is divergence free,

$$\bar{\nabla} \cdot \bar{V} = 0 \tag{2.13}$$

The Lorentz force is treated as a body force like gravitation force which is included in the momentum equation,

$$\rho \frac{D\bar{V}}{Dt} = -\bar{\nabla} p + \mu \nabla^2 \bar{V} + \bar{F}_{\mathrm{L}} \tag{2.14}$$

where ρ is the fluid density, p is the pressure, and μ is the dynamic viscosity. Since the current density generated in this system is quite low, Joule heating effect can be neglected. Therefore it is appropriate not to solve the energy equation. Also because of negligible Joule heating, buoyancy due to temperature gradients can be neglected. Therefore the gravity term is not included in eqn. (2.14). However, density gradients and natural convection can exist due to the tendency to attain electroneutrality in a conducting medium. Isaac et al [8] have proposed a non-dimensional parameter called the TN number to help determine if natural convection will be important in mixed convection problems. Including a model for this effect requires careful consideration, and it is beyond the scope of this work, but is a topic of ongoing effort.

In order to study the mixing performance in such a system, two or more species are assumed to be in the device. The species transport equation (also known as the convection-diffusion equation) is given by,

$$\frac{\partial C_i}{\partial t} + \bar{\nabla} \cdot (C_i \bar{V}) = \bar{\nabla} \cdot (D_i \bar{\nabla} C_i) \tag{2.15}$$

2.5. ADVECTION EQUATION

Since the analyses of chaotic advection are based mostly on particle trajectories, accurate positions of the particles which are initially injected into the computation domain are required, and need to be updated at each time step. The motion of a passive particle can be tracked by numerically integrating the advection equation shown below,

$$\frac{d\mathbf{X}(t)}{dt} = \bar{V}(\mathbf{X}, t) \tag{2.16}$$

where $\boldsymbol{X}(t)$ is the particle position vector at time t which has the initial condition $\boldsymbol{X}(0)$ = x0. The velocity vector $\bar{V}$ is first obtained by solving eqns. (2.12), (2.13) and (2.14) with appropriate boundary conditions, and equation (2.16) is then integrated to obtain the positon vector. And then, the particle trajectories can be visualized.

3. MODELING AND SIMULATIONS OF CHAOTIC MIXING

3.1. CHAOTIC MIXING IN TWO DIMENSIONAL MICROFLUIDICS

This section presents the results of MHD based chaotic advection to enhance mixing in two-dimensional microfluidics.

3.1.1. Geometry and Mesh. In this section, we describe the two-dimensional model of our MHD stirrer. Several different configurations are considered to compare their mixing performances.

Our MHD stirrer consists of a cylindrical cavity with cylindrical rods placed inside the cavity. The cavity and the rods extend to $\pm\infty$. The entire cavity side wall serves as the counter electrode and the entire curved surfaces of the inner cylinders, when activated, serve as working electrodes. Thus, different configurations of the working electrodes can be obtained by changing the radii of the inner cylinders, their number, and their locations within the cavity. Figures 3.1 (a) – (e) show the different configurations. In all the five configurations the radius of the cavity (Ro) = 2000 μm, and the radii of the rods (Ri) = 160 μm. Configurations (a) and (b) shown in Figure 3.1 (a) and Figure 3.1 (b), respectively, are referred to as concentric and eccentric. For the eccentric case (b), the working electrode is at Ro/2 from the center of the cavity. Similarly, if we place several working electrodes at different locations, several additional configurations can be obtained. Figure 3.1 (c) – (e) show these additional configurations designated (c) – (e), respectively. For each of these configurations, the radii of the cavity and the rods are the same as in Configurations (a) and (b), and the rods are placed at a distance of Ro/2 from the center of the cavity. For the configuration (c) with two working electrodes, they are located at 6 o'clock and 9 o'clock positions, and the other configuration with two working electrodes, (d), they are placed at 3 o'clock and 9 o'clock positions. Finally, a configuration with four electrodes, (e), is considered with the electrodes located at 3 o'clock, 6 o'clock, 9 o'clock and 12 o'clock positions. In all the above configurations, the counter electrode is the cavity wall. A magnetic field (B) of constant strength and direction is applied as shown in Figure 3.1 (b). It is directed along the axis of the cavity, along +z. The cavity is filled with an electrolyte solution. See Figure 3.1 (a) – (e) for schematic views of all the configurations.

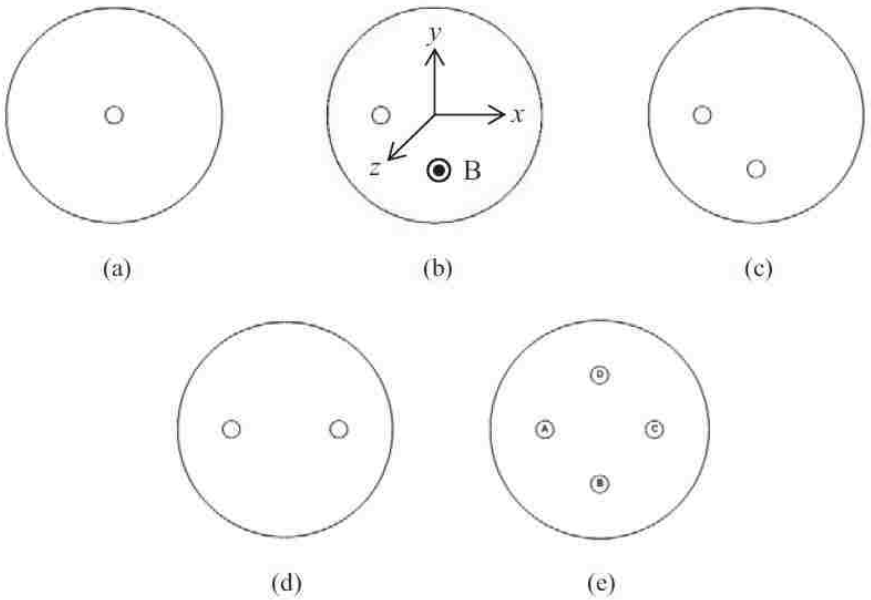

Figure 3.1. A schematic view of the electrode configurations. (a) concentric cylinder, (b) eccentric cylinder, (c) two working electrodes which are at 6 and 9 o'clock positions, (d) two working electrodes that are at 3 and 9 o'clock positions and (e) four electrodes which are at 3.

The mesh is generated through software Pointwise. Influenced by the physical features of the configurations considered in this study, our unstructured mesh is distributed from fine at the working electrode to coarser away from it. Such a mesh distribution allows having a denser mesh in regions where the gradients of the solution variables such as the velocity are large. If necessary, a hybrid mesh consisting of regions of structured and unstructured mesh can also be used. Figure 3.2 shows the hybrid mesh of the case (d) in Figure 3.1. In Figure 3.2, structured and fine mesh is used around two holes in the middle region in order to capture the potential gradient adjacent to the disk electrodes, while unstructured and coarser mesh is used in the rest of area. The choice of structured or unstructured mesh could be determined by the different models with different solvers. For example, in VOF model in ANSYS FLUENT, structured mesh is preferred.

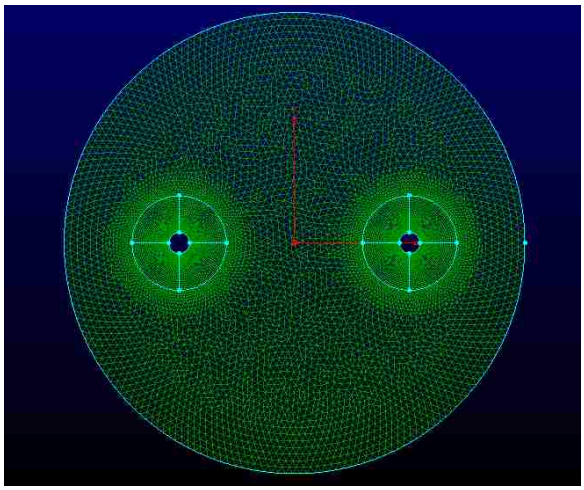

Figure 3.2. Hybrid mesh of two working electrodes placed symmetrically along axis y, case (d) in Figure 3.1.

3.1.2. Simulation Setup.

3.1.2.1 Initial and boundary conditions. For the simulation of transient phenomena, we start with the fluid initially at rest, and therefore the velocity components everywhere in the solution are set to zero. To study mixing, two species, which are initially unmixed, are considered. They occupy the top and bottom halves of the solution domain. Mathematically, for species 1, the initial concentration distribution can be written as

$$C_1(x, y, 0) = \begin{cases} 0, & y > 0 \\ 1, & y < 0 \end{cases} \tag{3.1}$$

where the x and y coordinates are as shown in Figure 3.1. (b).

Since the Reynolds number of the flow is very small, the governing equations are for laminar flow. We use the non-slip boundary conditions for the tangential velocity components, in addition to the normal components being set zero as wall. Note that, for all the cases included in our study, there are no inflows or outflows. Mathematically, the hydrodynamic boundary condition is,

$$\bar{V}_{\text{wall}} = 0. \tag{3.2}$$

In order to deliberately manipulate the flow in the computational domain, time-dependent boundary conditions for the electric potential can be specified for the working electrode. For the cavity wall which acts as the counter electrode, the potential is set as follows

$$\phi = 0. \tag{3.3}$$

At the working electrodes, time-dependent boundary conditions for the electric potential are specified. In all cases, a sinusoidal function for the potential is applied as follows

$$\phi = \phi_0 \sin(2\pi t / T). \tag{3.4}$$

where, T is the period and ϕ_0 is the amplitude.

It is worth noting that the potential ϕ we apply at the working electrode is the electric potential at the outer edge of the double layer rather than at the electrode surface. The double layer is very thin (~10 to 100 nm thick), and the electric potential drops dramatically across it. Using the Gouy-Chapman Theory and Poisson-Boltzmann equation, we can calculate the electric potential at the outer edge of the double layer and use it for the electrode boundary condition. The calculation procedure is discussed in detail in section 2.2. This approach is used to avoid a multi-physics, multi-scale formulation, which would require solving the Poisson-Boltzmann equation in two-dimensions with a large number of grid points in the double layer.

3.1.2.2 Fluent setup. As we can see in chapter 2, the governing equations including electric potential (eqn. 2.4), Navier-Stokes (eqns. 2.13-2.14) and species transport (eqn. 2.15) are strongly coupled, and therefore their solution will require coupled solvers. In our simulations, the commercial software package Ansys Fluent [46] is chosen to simultaneously solve the governing equations.

Fluent employs a finite volume method in which the conservation equations are discretized in the integral form for each volume element and the variable are solved for at the nodes located at the center of the volume elements. The specific aspects of the MHD simulations such as the presence of the Lorentz force term in the momentum equation (eqn. 2.14) and time dependent boundary conditions can be accomplished by using UDFs

(user defined functions) that can be added to the standard Fluent solver. UDFs are functions coded in C, which are then compiled and linked to make them part of the standard solver. They are invoked as desired via graphical or text user interfaces. Using this approach, we have successfully solved a wide range of problems including adsorption [47], multiphase flow [48], and thermophoresis [49]. The Laplace equation (eqn. 2.4) for the electric potential, which is not a transport equation, is solved as a user defined scalar (UDS), an option provided in Fluent to avoid using multiple solvers when equations such as the field equation for ϕ are present in the model.

3.1.3. Model Validation. A three-dimensional simulation is also conducted to validate our CFD model by comparing with the experimental results [25]. A 3D cylindrical cell with three circular electrodes deposited concentrically on the bottom surface is studied. The geometry details and parameters for this case can be found in [25]. In the simulation, 40,000 passive tracer particles are tracked in order to visualize the flow. In this validation case, only the middle electrode is activated, which leads to a counter-rotating flow. Figure 3.3 shows the material lines at t=50s, 110s and 170s in our simulations (first row), and the snapshots of a material blob taken every 50s from the numerical simulations and dye experiments (second and third rows, respectively) [25]. Quantitatively agreement between our 3D simulation and the dye experiment can be seen. The differences between them may be attributed to the non-uniformity of the applied magnetic field in the experiments, and the differences in the electrolyte properties.

Aref's pioneering work shows that the chaotic advection can occur in time-dependent two-dimensional flows and three-dimensional steady and unsteady flows [16]. Our 2D model should be reasonable for the parametric studies reported in this work, since under our 2D formulation, we have very similar flow structures compared with those from experiments and 3D simulations from previous work [21]. The full 3D simulations will be presented in the next chapter.

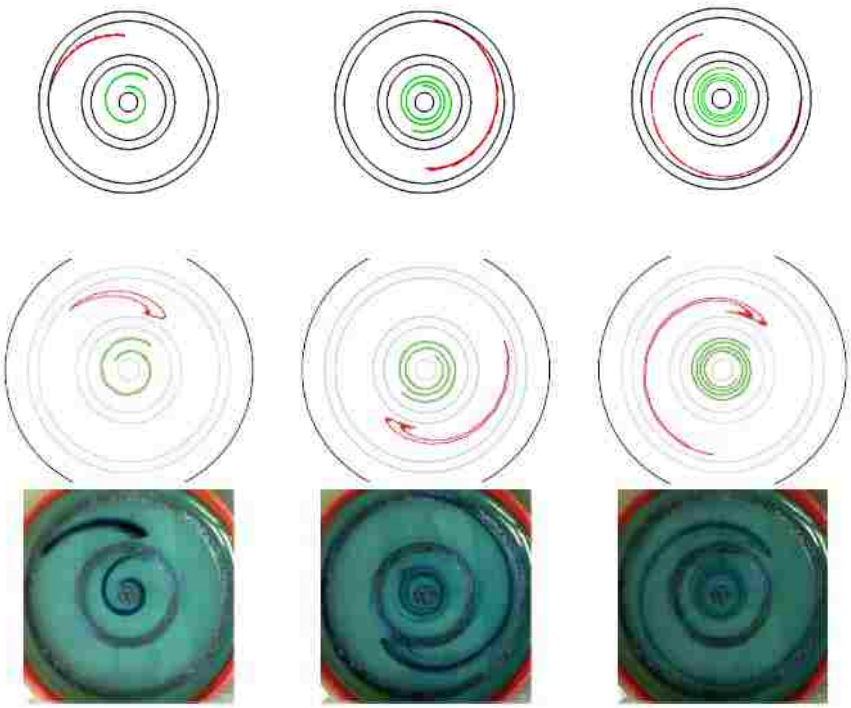

Figure 3.3. First low: Material lines at t=50s, 110s and 170s by using our CFD model. Second and third rows: Numerical simulations and dye experiments [25], snapshots taken every 50s.

3.1.4. Results.

3.1.4.1 Overview. In this section, we present the results of simulation-based parametric studies. The results are divided into subsections depending on the numbers of electrodes pairs used, the placement of the working electrodes, the period of the sinusoidal potential boundary condition, the electrode potential switching scheme, and the strength of the magnetic density flux.

First, mixing for the configurations with one electrode pair, shown in Figure 3.1 (a) and Figure 3.1 (b), is discussed. In these cases, the Lorentz force reverses direction periodically between clockwise and counter-clockwise. This reversal is accomplished by applying a sinusoidal potential in the form of eqn. (3.4). The effects of varying the time period T and the magnetic field strength B on the mixing quality are discussed. Next, cases that include two and four electrode pairs are discussed. Having more than one electrode pair allows applying potentials to the different electrode pairs according to a

pre-determined scheme to induce more complex chaotic advection and achieve higher mixing quality.

In all the simulations, we choose 0.1 M KCl solution as the electrolyte which has an electrical conductivity, σ =1.29 S/m. The diffusion coefficient D and the dynamic viscosity μ of the mixture are 1.0×10^{-11} m^2/s and 0.001003 kg/m-s, respectively. In all cases considered in this study, the amplitude of the sinusoidal potential applied on the working electrode after considering the double layer drop is 0.04V. The discussion of the results can be aided by estimating the relevant non-dimensional parameters of the problem. The Reynolds number which is defined as Re = $\rho Ud/\mu$ in our simulations ranges from ~1 to ~10, where d is the diameter of the stirrer, and U is characteristic velocity. For this Reynolds number range, the flow is clearly laminar. The Peclet number, defined as Pe = Ud/D is of order 10^6 which indicates that convection would be dominant. Another relevant non-dimensional parameter is the Hartman number Ha which is defined as $\mathrm{Ha} = Bd\sqrt{\sigma/\mu}$. The Hartman number can be interpreted as the square root of the ratio of Lorentz force to the viscous force. In our case, it is of order 0.1 which indicates that viscous effects have strong influence on the flow. Finally, in order to quantify the stirrer's performance, a mixing quality α is defined as [23].

$$\alpha(t) = 1 - \frac{\delta^2(t)}{\delta^2(0)} \tag{3.5}$$

where $\delta^2(t)$ is the standard deviation of the dimensionless concentration distribution at time t, which can be written as

$$\delta^2(t) = \iint_S \left[C(x,y,t) - \bar{C}(x,y,t) \right]^2 dxdy \tag{3.6}$$

where $\bar{C}(x,y,t)$ is the volume average concentration of the entire domain. When the fluids are completely mixed, $\delta^2(t) \to 0$ and $\alpha \to 1$.

3.1.4.2 Mixing under one, two and four working electrodes.

3.1.4.2.1 <u>Configuration (a): T=8s, t_{max}=8s</u>. In this subsection, we discuss simulations of Set 1. First, the results of the concentric cylinder (Figure 3.1 (a)) are presented. The time-dependent boundary condition applied at the working electrode has

the form of eqn. (3.4), where the period T and total flow time t_{max} are both chosen as 8s. The magnetic field strength B is 1.75T. The peak current on the cavity wall is ~0.127 A/m. The time evolution of the electric current and voltage on the working electrode is shown in Figure 3.4, which shows that the voltage and the current change sign once during the 8s period. In other words, the direction of the current is first from working electrode to the counter electrode and then it is reversed.

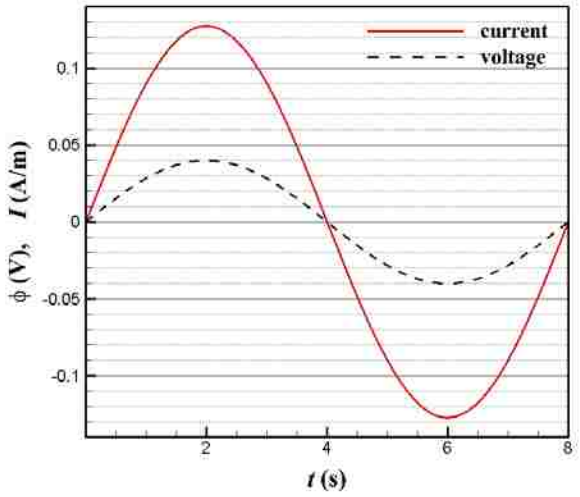

Figure 3.4. Time evolution of the electric current and voltage on the working electrode. Concentric cylinder, T=tmax=8s and B=1.75T.

As a result, according to the right hand rule of the Lorentz force $\overline{F}_{\mathrm{L}} = \overline{J} \times \overline{B}$, we see that it would induce a clockwise motion during the first half of the cycle and then the direction of motion would reverse. Thus, the variations of the potential, current flux and the magnitude of the Lorentz force have the same shape and they differ only by a scale factor due to the linear relationship among them (recall that the magnetic field intensity is constant in magnitude and direction in each case). However, it is important to note that the fluid motion may not be in phase with the applied potential, since the fluid motion will be influenced also by inertia and viscous effects. Figure 3.5 shows the variation of

the maximum velocity magnitude during one period. Note that the two halves of the curve are not identical, nor is each half symmetrical about its peak. The maximum velocity is ~11.5 mm/s for this case. Figures 3.6 (a) and (b) display the velocity vectors at t = 3s and t = 6s showing flow reversal, which, as expected, follows nearly the sinusoidal variations of the potential, current and Lorentz force.

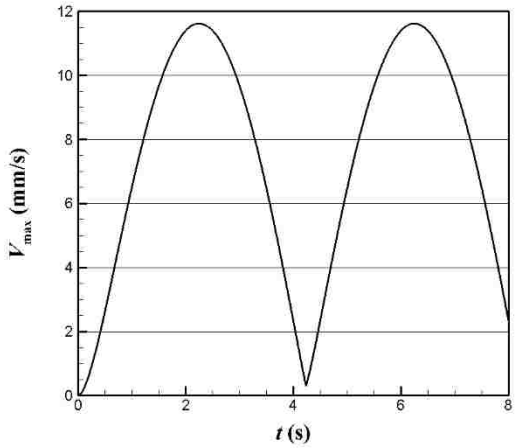

Figure 3.5. Time evolution of the maximum velocity magnitude. Concentric cylinder (Figure 3.1 (a)), T=t_{max}=8s, B=1.75T.

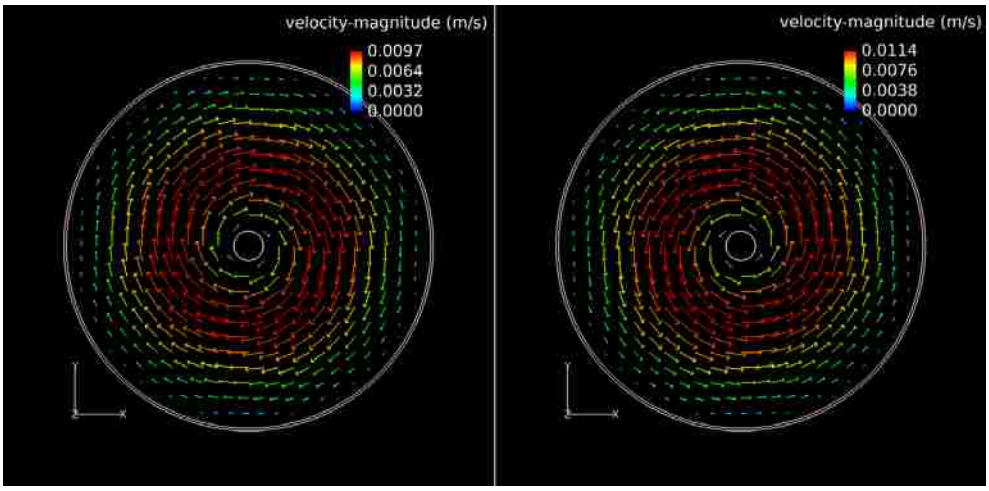

Figure 3.6. Velocity vectors at t=3s (a) and 6s (b). Concentric cylinder T=t_{max}=8s and B=1.75T.

Figure 3.7 (a) shows the velocity profile at y=0, t=2s. We see that, to the left and right of the working electrode, the velocity magnitude increases from the working electrode to reach a maximum value and then decrease to zero at the counter electrode. In most electrochemical setups, the counter electrode has a larger area than the working electrode, and therefore the current density at the working electrode is much larger than that at the counter electrode. As a result of the difference in the electrode areas, the larger current density near the working electrode generates a larger Lorentz force, which therefore influences the velocity magnitudes and the development of the the velocity field in the fluid domain. However, note that the maximum velocity occurs at the location of the maximum current density. Due to the no slip condition at the working electrode where viscous effects constrains the velocity to be zero, the maximum velocity is located slightly away from the working electrode showing a steep gradient from zero to maximum. Figure 3.7 (b) shows the associated current density profile and Lorentz force profile at y=0 and t=2s, respectively. At the working electrode, the current density is maximum, and so is the Lorentz force density. The maximum values of the current density and Lorentz force density are 126.686 A/m^2 and 221.665 N/m^3.

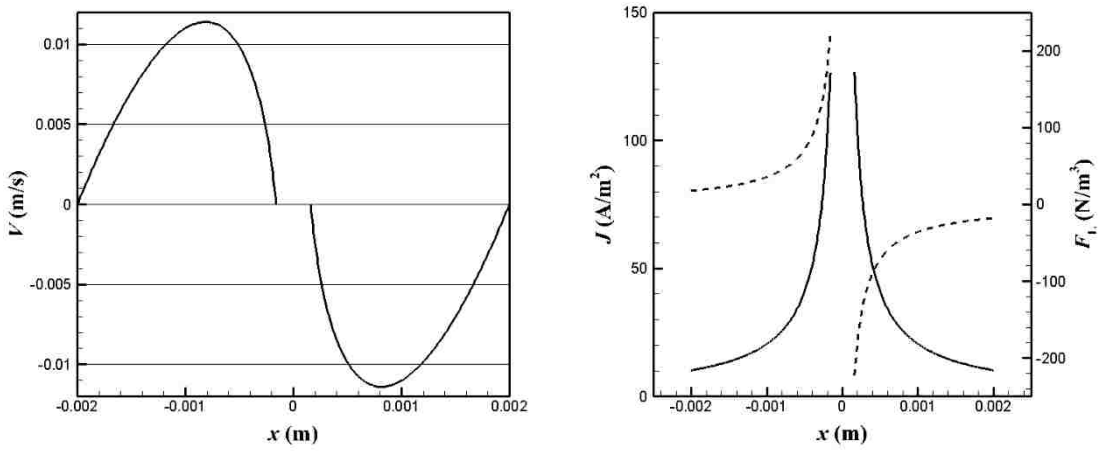

(a) (b)

Figure 3.7. (a): Velocity profile at y=0 at t=2s. (b): Current density (solid line) and Lorentz force density (dashed line) at y=0 at t=2s. Concentric cylinder T=t_{max}=8s and B=1.75T.

Figure 3.8 depicts the time evolution of species mass fractions at t=0s (a), 1s (b), 2s (c), 3s (d), 4s (e), 5s (f), 6s (g) and 8s (h). It can be clearly seen that the interface between the two species distorts and stretches by the action of the Lorentz force. More striations develop as time t increases, and for t > 4s, the distinction between two species begins to disappear in the region away from the walls indicating that the two fluids are well-mixed there. Figure 3.8 (h) shows that pockets of unmixed fluids are still present near the walls after the completion of one cycle of the potential wave. Obviously, the walls act as a damper on mixing, as chaotic structures which act as an agent for mixing do not develop as extensively near the walls as away from them.

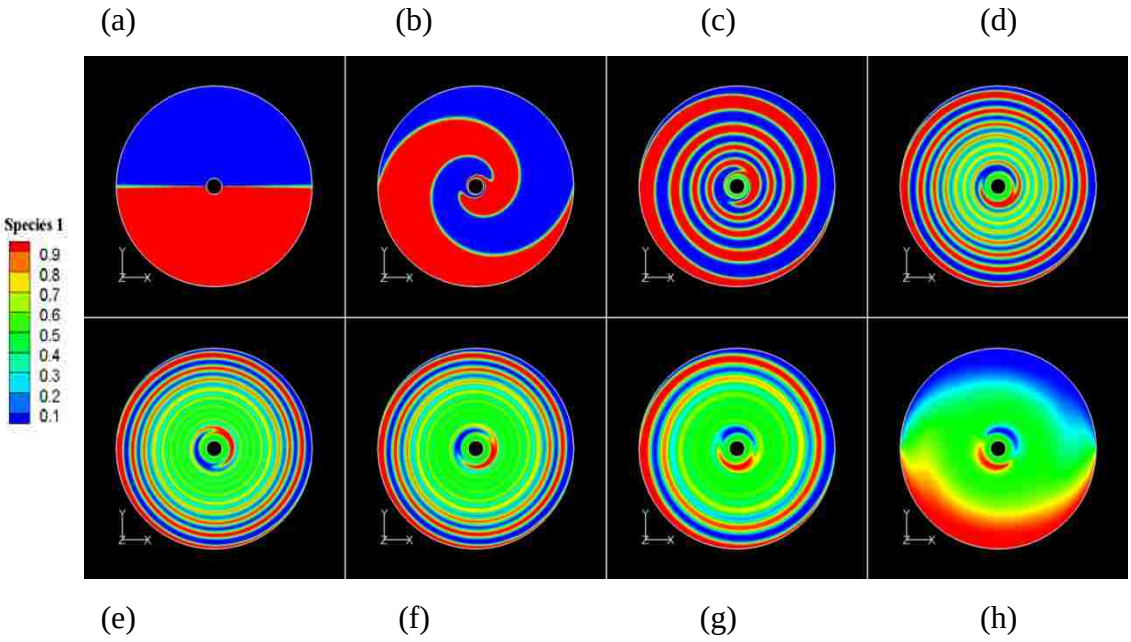

Figure 3.8. Time evolution of species mass fraction at t=0s (a), 1s (b), 2s (c), 3s (d), 4s (e), 5s (f), 6s (g) and 8s (h). Concentric cylinder, T=tmax=8s and B=1.75T.

Figure 3.9 shows the mixing quality $\alpha(t)$ (eqn. 3.5) as a function of time, and its value reaches ~0.661 at the end of the cycle. However, it is worth noting that during the second half of the cycle (t > 4s) during which the Lorentz force direction reverses, the mixing quality increases only slightly. The reason for this asymptotic behavior will be

discussed later. Based on Figures 3.8 and 3.9, we can propose that it is possible to mix two fluids by introducing a cyclically varying Lorentz force that periodically reverses the flow that gives rise to stretching and folding. For this case, the mixing performance α = ~0.65 was attained within time $t < T$ starting with the two fluids completely unmixed (α = 0) at t = 0.

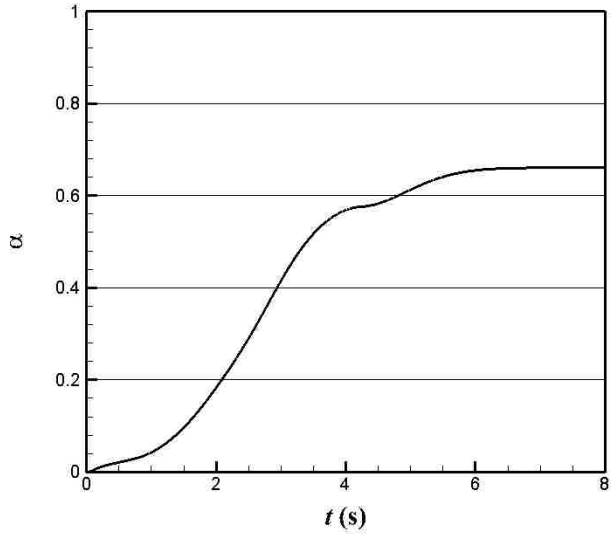

Figure 3.9. Mixing quality α as a function of time t. Concentric cylinder T=t_{max}=8s and B=1.75T.

3.1.4.2.2 <u>Configuration (a), variable *T*, t_{max}=15s</u>. Next the mixing duration t_{max} is extended to 15s, and different values of period T are considered to investigate its effect on the mixing performance, where the cyclical boundary condition at the working electrode is still in the sinusoidal form of eqn. (3.4) with the same amplitude of electrode potential and the magnetic field strength. Figure 3.10 (a) shows the mixing quality values vs. time under different time periods T=2s, 3s, 4s, 5s, 8s, 10s and 15s. Figure 3.10 (b) depicts the final mixing quality values and the maximum velocity magnitudes as a function of time period T.

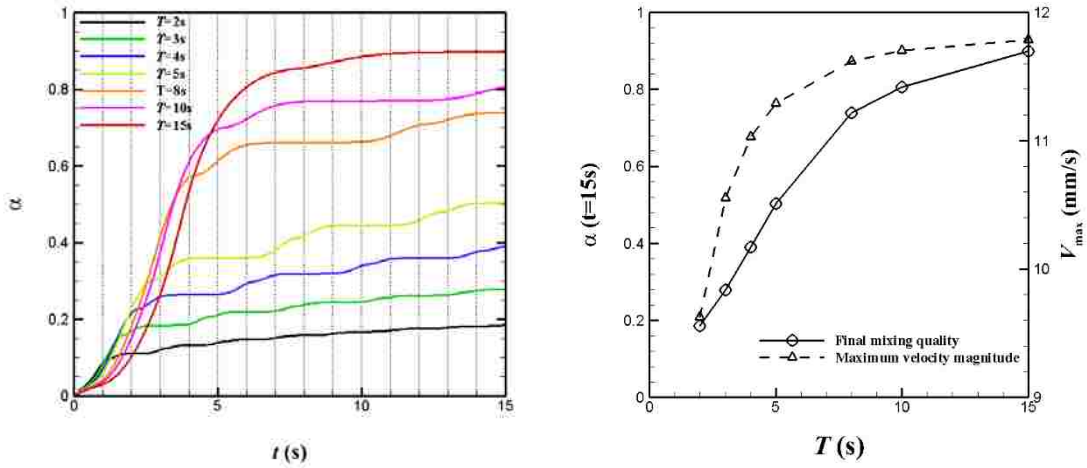

(a) (b)

Figure 3.10. (a): Time evolution of mixing qualities with different time period *T*. (b): Final mixing quality (solid line with circle symbol) and the maximum velocity magnitude (dashed line with delta symbol) as a function of time period *T*. Concentric cylinder, t_{max}=15s and B=1.75T.

From Figures 3.10 (a) and (b), we can conclude that a large time period *T* corresponds to better mixing quality. The reason why a large value of *T* leads to better mixing may be that at larger *T* the interface between the fluids stretches for a longer time, and therefore more striations can be generated. Roughly stated, stretching and folding are the two mechanisms that underlie mixing, and stretching would dominate at larger values of *T* and folding would dominate when *T* is shorter. For shorter time period *T*, the flow only rotates for a few loops during the first half period *T*/2, as a result the interface between the species is not well stretched and only a few striations are created. Thus, during the next half of the cycle, the flow will get reversed and bring the species concentration distributions to almost the original state, thus partially nullifying the stretching of the previous half cycle. Furthermore, it is worth noting here that for configuration (a) with a specific period *T*, mixing performance does not improve significantly at larger flow times (see Figure 3.10 (a)). For each value of *T*, the α vs. *t* curve reaches a plateau after the initial steep rise, which suggests that reversing the flow has little effect on mixing enhancement. The reason may be that though the flow is

periodically reversed, it does not generate any chaotic patterns, but the fluid is just "pumped" back and forth creating a repeating pattern. Once the fluid continues to be stretched during a long half period, say $T/2$=5s, most of the mixing is accomplished during this time. However, if the flow is not well mixed during the half period time $T/2$, then even a long total flow time does not lead to a significant improvement of the mixing performance.

Figure 3.11 depicts the mass fractions of the cases with T=2s, 3s, 4s and 10s at $t=T/2$, T, $3T/2$ and $2T$ respectively. We see that for larger time period T, more striations are created during the first half cycle. For a smaller T (2s, 3s and 4s), if the flow is not well mixed during the first of the cycle, then in the second half, the original state is nearly restored. For T=10s, in the first half cycle, the flow is already well mixed. The corresponding animations of species mass fractions provide further visual confirmation of these aspects of the mixing behavior.

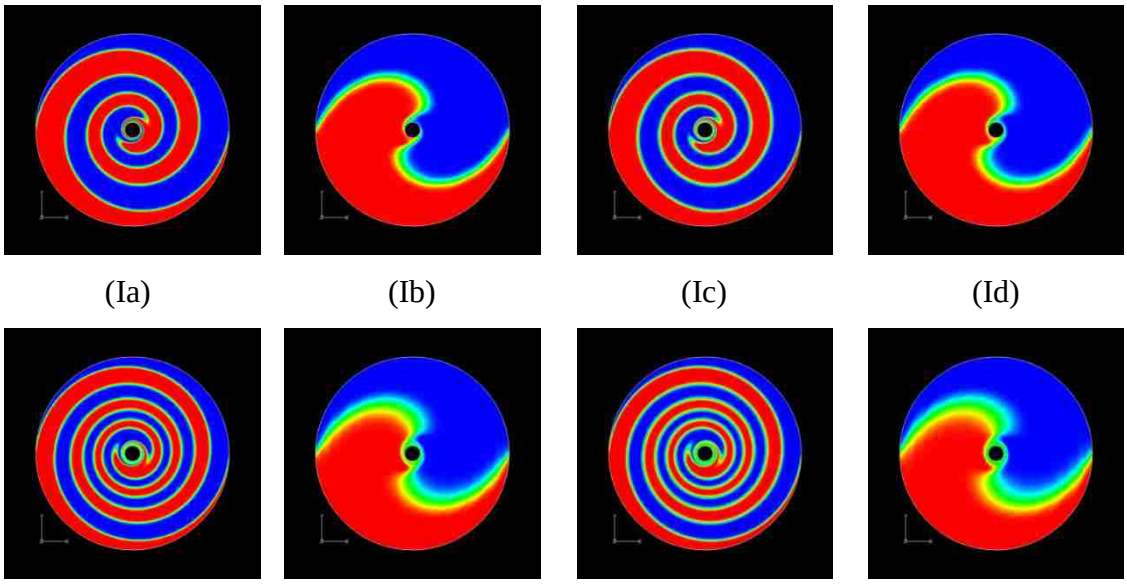

Figure 3.11. Species mass fractions for T=2s (I), 3s (II), 4s (III) and 10s (IV) at t=$T/2$ (a), T (b), $3T/2$ (c) and $2T$ (d). For T=10s, the total flow time is 15s so the (IVd) frame is absent for $t=2T$. Concentric cylinder, t_{max}=15s and B=1.75T.

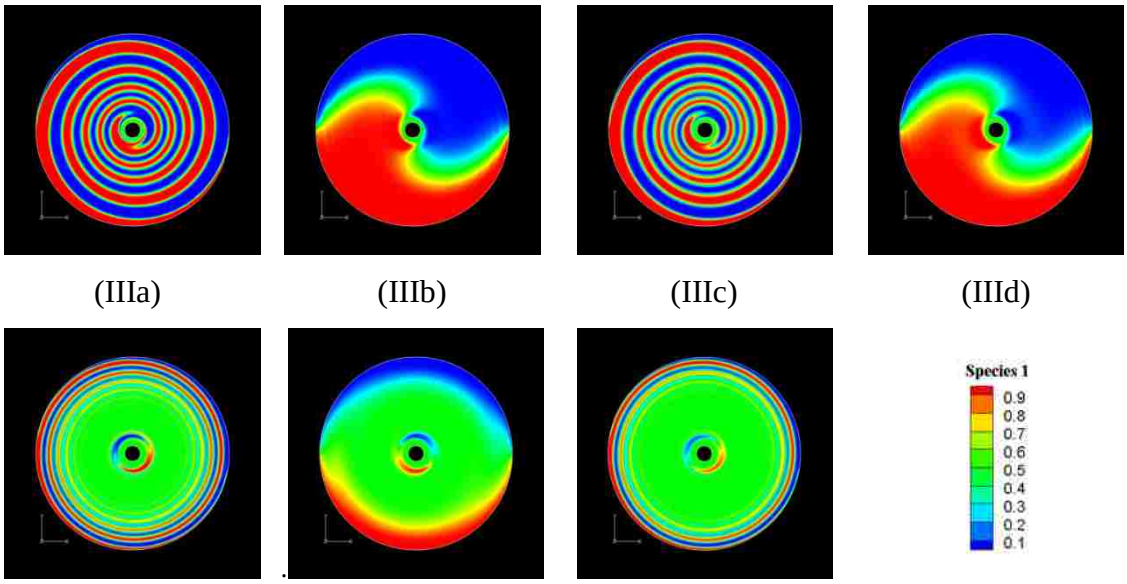

(IIIa) (IIIb) (IIIc) (IIId)

(Iva) (IVb) (IVc) Color bar

Figure 3.11. Species mass fractions for T=2s (I), 3s (II), 4s (III) and 10s (IV) at t=T/2 (a), T (b), 3T/2 (c) and 2T (d). For T=10s, the total flow time is 15s so the (IVd) frame is absent for t=2T. Concentric cylinder, t_{max}=15s and B=1.75T (cont.).

3.1.4.2.3 Configuration (a): T=8s, t_{max}=16s, variable B. The effect of magnetic field strength on mixing performance is also of interest.

Figure 3.12 (a) presents α vs. t for different magnetic field strengths: B=0.5T, 0.75T, 1.0T, 1.25T, 1.5T and 1.75T, all the cases are for T=8s and t_{max}=16s. Obviously, magnetic field strength plays an important role in mixing performance since the Lorentz force is directly proportional to it, and therefore it strongly affects the velocity magnitude. Larger Lorentz force can drive the flow to form more loops in a half period T/2, and thus more striations are created leading to higher mixing quality. Figure 3.12 (b) shows the final mixing qualities and the maximum velocity magnitudes vs. magnetic field intensity B. It is clear that stronger magnetic field strength B increases the velocity magnitude and improves the mixing quality.

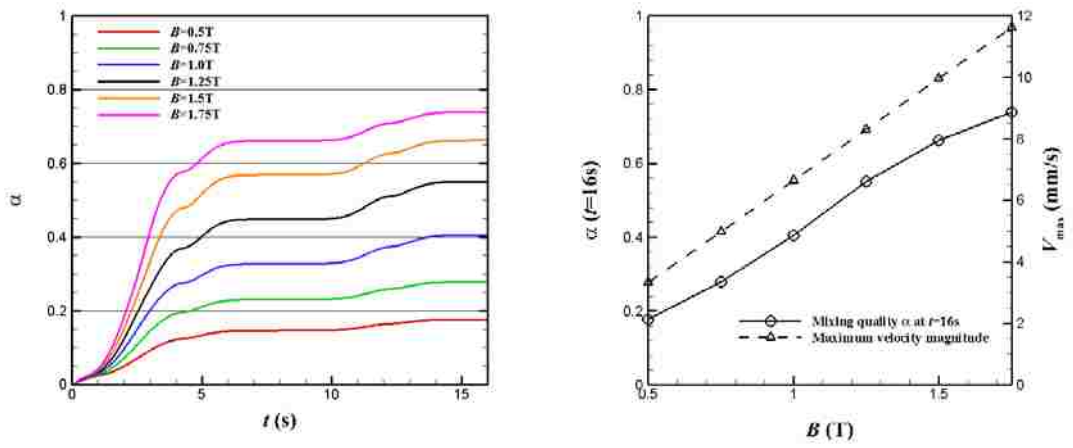

(a) (b)

Figure 3.12. (a): Mixing quality as a function of time t with different magnetic field intensity B. (b): Final mixing quality (solid line with circle symbol) and maximum velocity magnitude (dashed line with delta symbol) as a function of magnetic field intensity B. Concentric cylinder, T=8s and t_{max}=16s.

3.1.4.2.4 <u>Configurations (b)-(d): $T=t_{max}$=8s, φ in-phase and 180° out-of-phase</u>.

In this subsection, the other configurations in Figures 3.1 (b)-(d) are investigated by applying a cyclically varying potential at the working electrode pairs. A zero potential boundary condition is applied at the counter electrode in all cases and the potentials applied on the working electrodes are all in the sinusoidal form of eqn. (3.4) with $T=t_{max}$=8s and B=1.75T. For Configuration (c) that has two working electrodes located at the 6 and 9 o'clock positions (Figure 3.1 (c)), the potential boundary conditions are identical. For Configuration (d) (Figure 3.1 (d)), two different schemes are studied. For the first, both working electrodes are at identical potential boundary condition of eqn. (3.4), and thus a clockwise motion is obtained during the first half of the potential cycle. For the second type, the sign in eqn. (3.4) is reversed for one pair of electrodes to induce two counter-rotational motions. Figure 3.13 depicts the electric potential contours, stream functions and the corresponding velocity profiles at y=0 of each case at t=2s. The flow structures have good agreements with the experimental flow visualizations in literature [21].

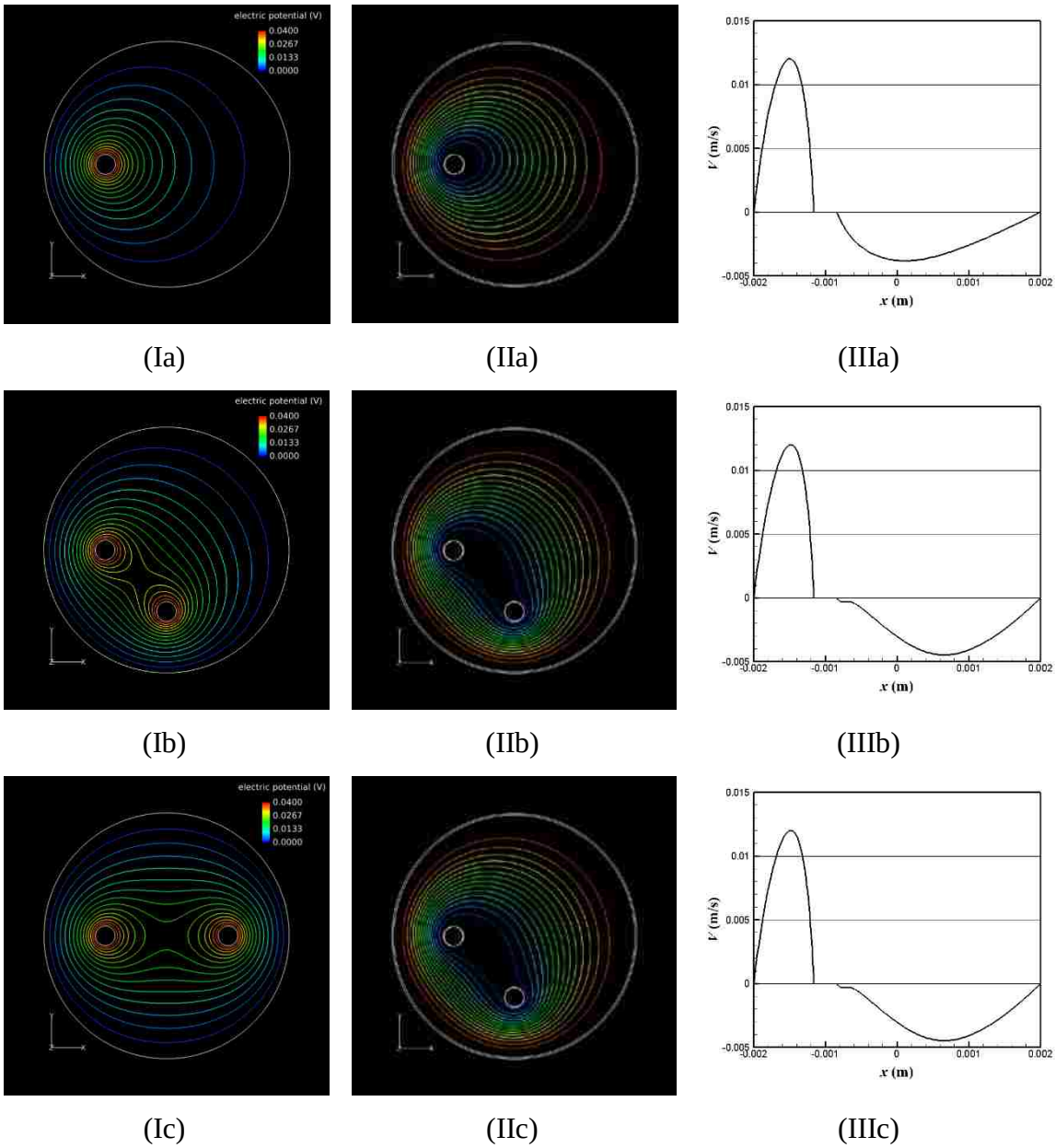

Figure 3.13. Electric potential contours (I), stream function contours (II) and velocity profiles (III) at y=0 at t=2s. (a): eccentric cylinder, (b): two electrodes at 6 and 9 o'clock positions with identical potential boundary conditions, (c): two electrodes at 3 and 9 o'clock positions with identical potential boundary conditions and (d): two electrodes at 3 and 9 o'clock positions with potential boundary conditions with the sign reversed. $T=t_{max}$=8s and B=1.75T.

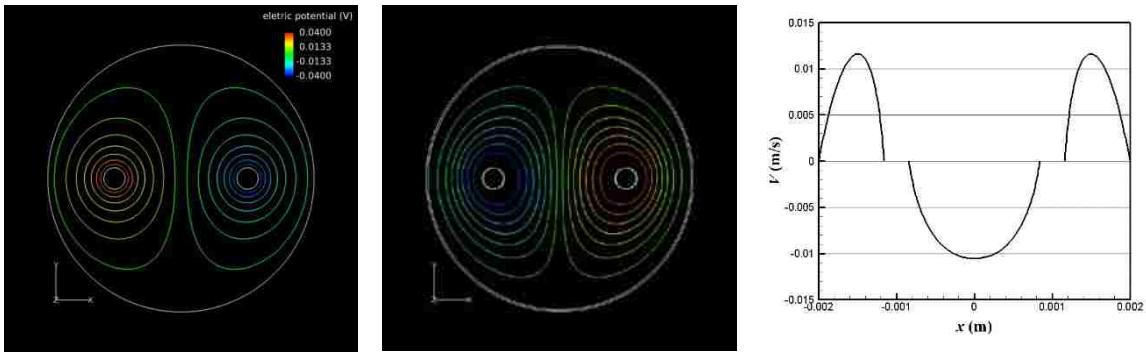

(Id) (IId) (IIId)

Figure 3.13. Electric potential contours (I), stream function contours (II) and velocity profiles (III) at y=0 at t=2s. (a): eccentric cylinder, (b): two electrodes at 6 and 9 o'clock positions with identical potential boundary conditions, (c): two electrodes at 3 and 9 o'clock positions with identical potential boundary conditions and (d): two electrodes at 3 and 9 o'clock positions with potential boundary conditions with the sign reversed. $T=t_{max}$=8s and B=1.75T (cont.).

Figure 3.14 shows α vs. t, where $T = t_{max}$ = 8s. It shows that case (d), Figure 3.13 (two electrodes with opposite signs for potential boundary conditions) has the best mixing performance. The probable reason is that two counter-rotating regions are created when the electrode potentials are of opposite sign. As a result, the stretching of the interface between the two fluids is more effective and more striations form during the first half period. Figure 3.15 depicts the mass fraction contours at $t=T/4$, $T/2$ and T of each case, respectively. It also shows that the last case generates most striations and thus has the best mixing performance. It is worth noting that, even in the last case, there are still some largely unmixed regions near the walls.

So far, we have discussed the mixing performances of all the configurations except the one with four working electrodes. We have seen that periodically reversing the flow by applying sinusoidal boundary conditions is a way to accomplish mixing. The time period T plays a strong role in enhancing mixing. The larger the period, the better the mixing performance is achieved. However, for a specified period T, increasing the total flow time t_{max} only slightly improves the mixing quality. The magnetic field strongly affects the mixing performance through the Lorentz force and velocity magnitude.

Finally, we see that by introducing two counter-rotational flow regions through appropriate choices of potential boundary condition schemes on the electrode pairs, mixing performance can be further improved.

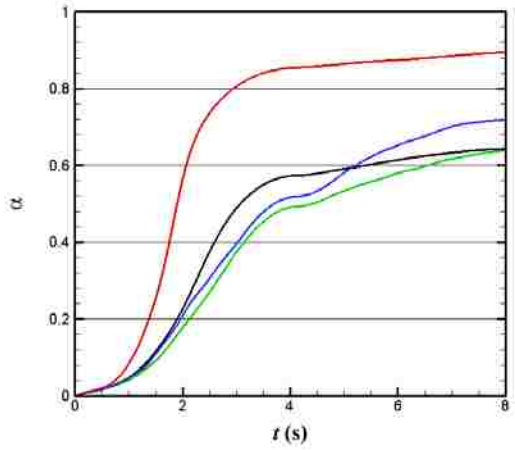

Figure 3.14. Mixing quality α as a function of time t. Color coding for online version: Black: eccentric cylinder, Green: two electrodes at 6 and 9 o'clock positions with same sign for potential boundary conditions, Blue: two electrodes at 3 and 9 o'clock positions with same sign for potential boundary conditions and Red: two electrodes at 3 and 9 o'clock positions with opposite signs for potential boundary conditions.

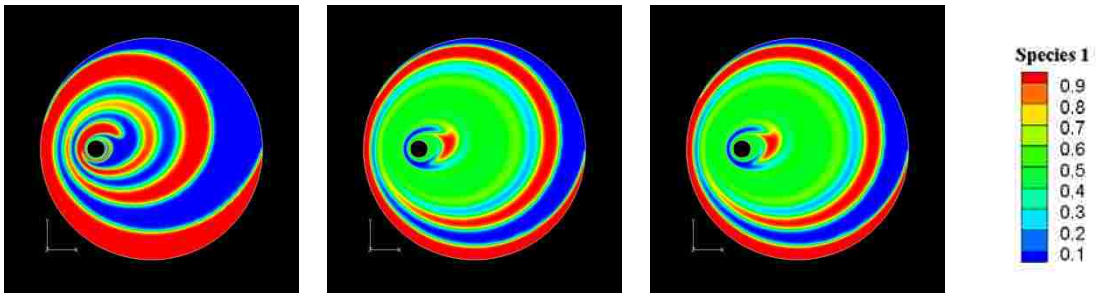

(Ia) (Ib) (Ic)

Figure 3.15. Species mass fraction contours for (I): eccentric cylinder, (II): two electrodes at 6 and 9 o'clock positions, (III): two electrodes at 3 and 9 o'clock positions with same signs for potential boundary conditions and (IV): two electrodes at 3 and 9 o'clock positions with opposite signs for potential boundary conditions. $t=T/4$ (a), $T/2$ (b) and T (c). $T=t_{max}=8$s and B=1.75T.

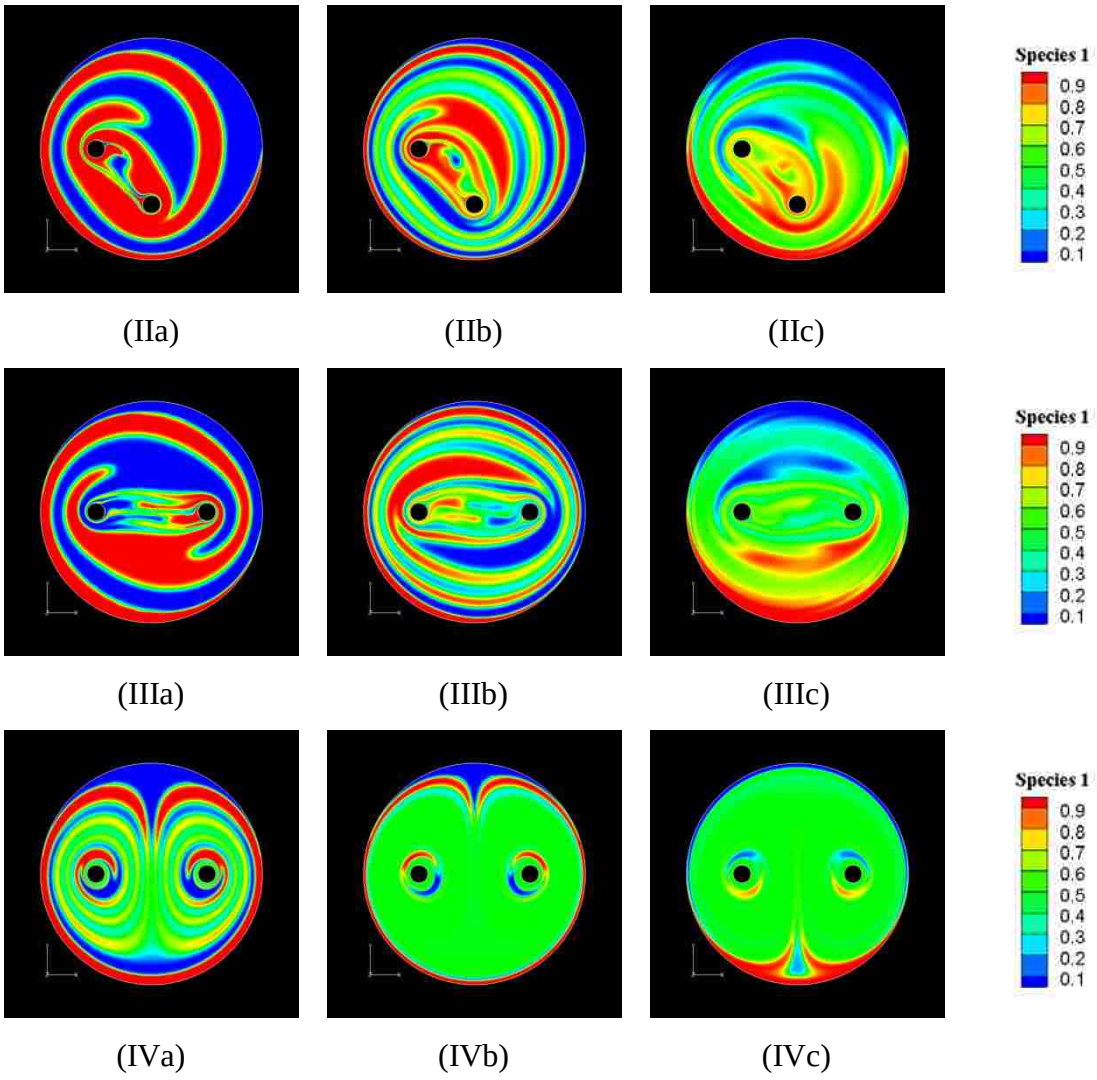

Figure 3.15. Species mass fraction contours for (I): eccentric cylinder, (II): two electrodes at 6 and 9 o'clock positions, (III): two electrodes at 3 and 9 o'clock positions with same signs for potential boundary conditions and (IV): two electrodes at 3 and 9 o'clock positions with opposite signs for potential boundary conditions. $t=T/4$ (a), $T/2$ (b) and T (c). $T=t_{max}$=8s and B=1.75T (cont.).

3.1.4.2.5 <u>Configuration (e): four working electrodes, different potential boundary Conditions</u>. In this set, configuration (e) (Figure 3.1 (e)) that has four working electrodes is studied. Here two groups of counter-rotational flows which periodically alternate, are created. This configuration is inspired by the two-electrode

configuration with counter-rotating flows discussed in the previous section. Figure 3.1 (e) shows the schematic view of the configuration, where the four electrodes are labeled A, B, C and D, respectively, starting at the 9 o'clock position and proceeding in the counter clockwise direction. The potential boundary condition schemes are as follows.

Scheme 1

$$\phi_{\mathrm{A}} = \phi_0 \sin(2\pi t / T), \quad \phi_{\mathrm{C}} = -\phi_0 \sin(2\pi t / T), \quad \phi_{\mathrm{B}} = \phi_{\mathrm{D}} = 0 \quad (kT \le t \le kT + T/2) \qquad (3.7)$$

Scheme 2

$$\phi_{\mathrm{A}} = \phi_C = 0, \quad \phi_{\mathrm{B}} = \phi_0 \sin(2\pi t / T), \quad \phi_{\mathrm{D}} = -\phi_0 \sin(2\pi t / T) \quad (kT + T/2 \le t \le (k+1)T) \qquad (3.8)$$

where ϕ_0 is the amplitude and the subscripts A, B, C and D, represents the electrodes in Figure 3.1 (e). k is an integer (= 0, 1, 2, …).

The time evolution of the electrode currents at the four working electrodes is shown in Figure 3.16 below. Note that the potential also will have similar variations since the current is proportional to the potential. The other data that apply to the cases in this section are: B=1.75T, T=8s and $t_{\max}$=16s. During the first half period (T/2), activating electrodes A and C can generate two counter-rotational flows and then activating electrodes B and D generates two other counter-rotational flows. This process is controlled by the alternating boundary conditions with period T, which induces complex chaotic advection. Note that when electrodes A and C are activated during the half period, electrodes B and D are inactive, and vice versa.

In this case we find that the final mixing quality is 0.986, close to complete mixing. Figure 3.17 presents the velocity vectors at times from 2s to16s at 2s interval. We see that during the first 4s, two counter-rotational regions form due to the activation of electrodes A and C and then two other counter-rotational regions form by activating electrodes B and D, and deactivating electrodes A and C. This switching scheme alternates 2 times during the 16s time span considered. Figure 3.18 in supporting material depicts the time evolution of the mass fractions. From that, we see that the unmixed regions near the walls found in previous case can be reduced and even completely eliminated by using activation/deactivation schemes similar to the one described in this section.

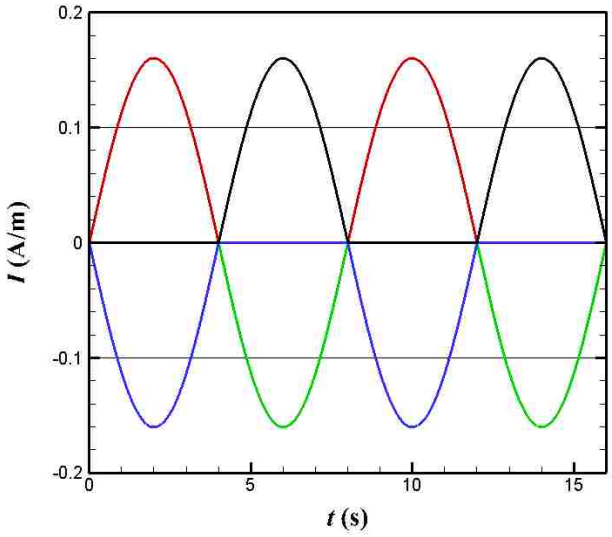

Figure 3.16. Time evolution of the electric currents on the working electrodes. T=8s and t_{max}=16s. Color coding for online version: Red: electrode A, Blue: electrode C, Green: electrode B and Black: electrode D.

(a) (b) (c) (d)

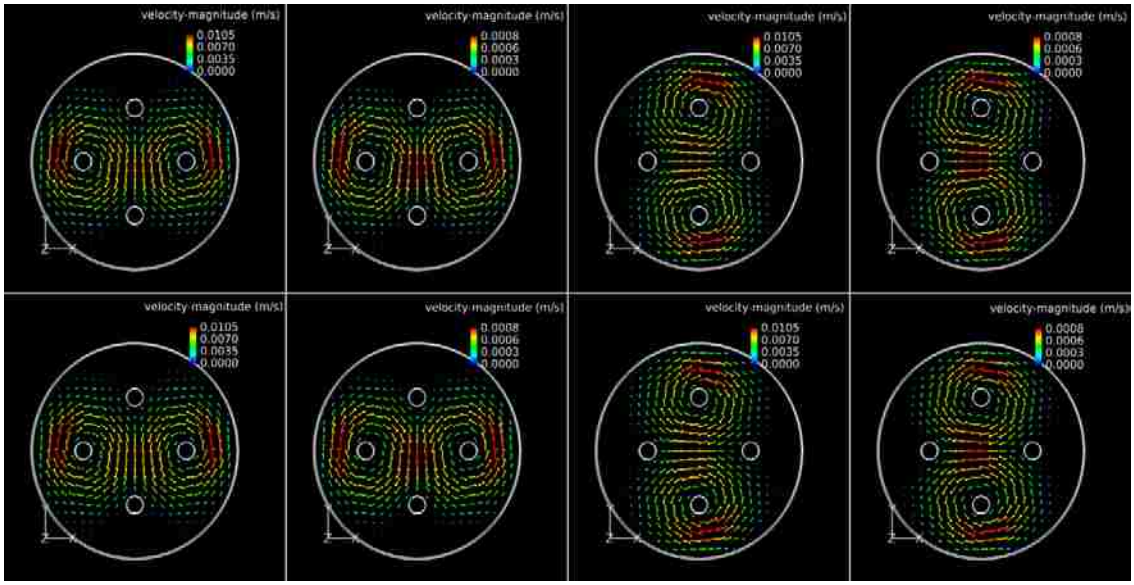

(e) (f) (g) (h)

Figure 3.17. Time evolution of velocity vectors with B=1.75T, T=8s and t_{max}=16s. Frames (a)-(h) represent, sequentially, t=2s-16s at 2s interval.

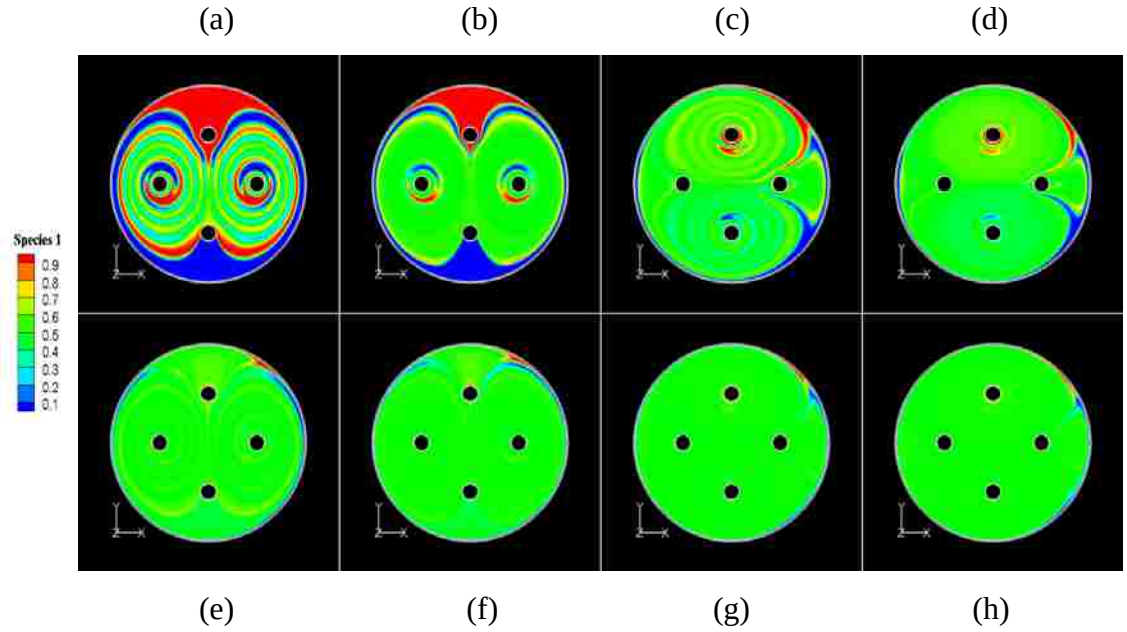

Figure 3.18. Time evolution of species mass fractions with B=1.75T, T=8s and t_{max}=16s. (a)-(h) stands for t=2s-16s at 2s interval.

This is an indication that the use of multiple electrodes and various activation/deactivation schemes allow more chaotic flow to develop due to the stretching of the interfaces between the fluids in a more complex pattern enabled by increasing the number of electrodes and choosing suitable switching schemes for the electrode potential boundary conditions.

Figure 3.19 (a) depicts the mixing quality vs. time t for different time periods, T=2s, 4s, 6s and 8s. t_{max}=16s, and B=1.75T. We see that all the cases have very good mixing performance after about 5s. Figure 3.19 (b) shows the maximum velocity magnitudes in the domain vs. T. The maximum velocity with different periods varies in the range 10.1 mm/s to 10.56 mm/s, which is of the same order as in previous case, indicating that it is not very sensitive to the time period.

As we discussed previously, the magnetic field intensity B has a strong influence on mixing performance, because it directly affects the magnitude of Lorentz force, thus resulting in higher velocity magnitudes. We now consider smaller values of the magnetic field intensity to investigate its effect on mixing. We will use the same switching scheme

as in the case with 4 working electrodes, but with a smaller value of B = 0.5T. Figure 3.20 (a) gives a comparison of the corresponding mixing qualities vs. time for T=2s, 4s, 6s and 8s. These results indicate that the mixing quality does not go down significantly as the magnetic field intensity is reduced to 0.5T. It is interesting to note that for all 4 values of T in Figure 3.20 (a), the mixing quality follows similar trend and reaches a final value of ~0.9. Recall the results in Figure 3.12 where the mixing quality with B=0.5T is only ~0.2. Results from Figures 3.12 (b) and Figure 3.20 (b) also show that under these two mixing scenarios with B=0.5T, the maximum velocity magnitudes are both ~3mm/s, which suggests that higher values of the velocity do not necessarily lead to significant increase in mixing enhancement, whereas, the complex chaotic flow induced by the potential switching scheme in the four-electrode configuration is seen to have a strong influence on increasing the mixing performance.

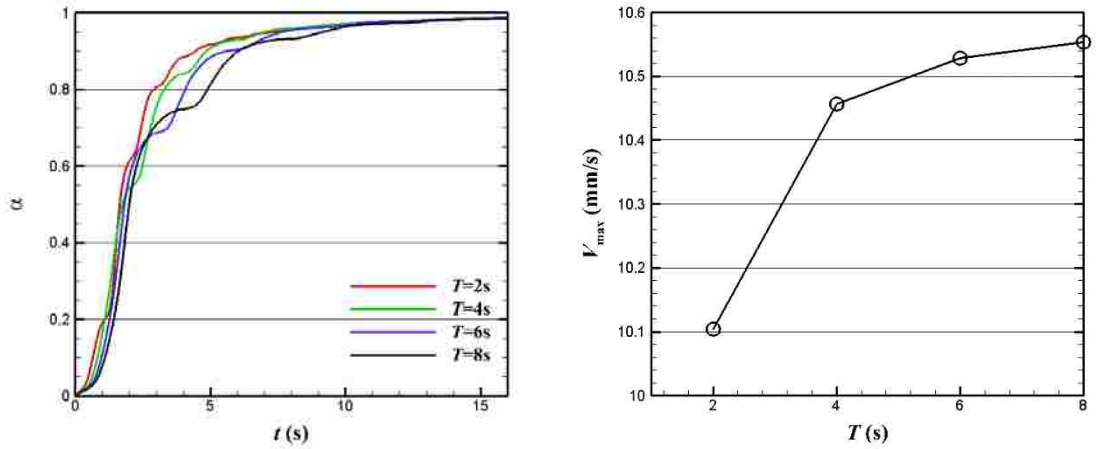

(a) (b)

Figure 3.19. (a): Mixing quality vs. time for different time periods T. Color coding for online version: Red: T=2s, Green: T=4s, Blue: T=6s and Black: T=8s. (b): Maximum velocity magnitude in the computational domain vs. time periods T. t_{max} = 16s and B=1.75T.

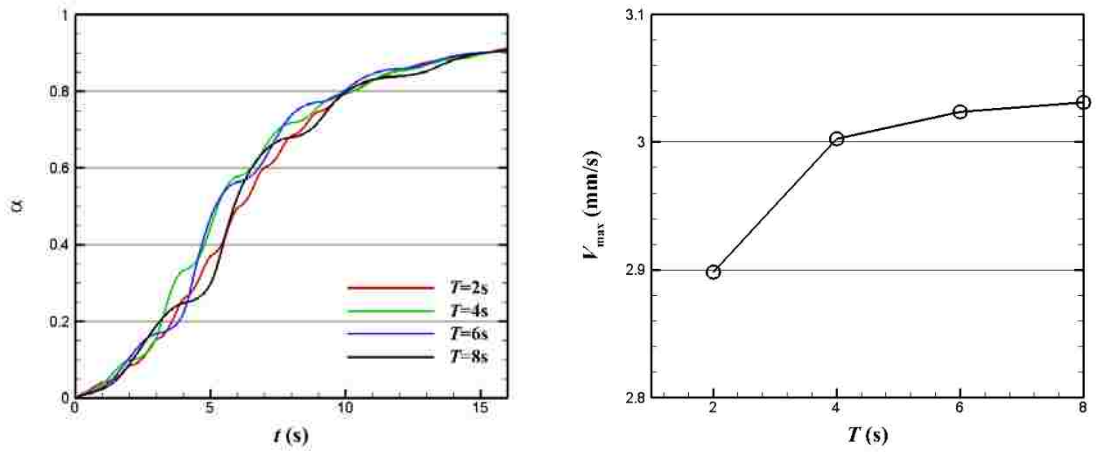

(a) (b)

Figure 3.20. (a): Mixing quality vs. time for different time periods T with B=0.5T and t_{max}=16s. Color coding for online version: Red line: *T*=2s, green line: *T*=4s, blue line: *T*=6s and black line: *T*=8s. (b): Maximum velocity magnitudes vs. different time periods *T*.

The time evolution of species mass fraction with *T*=4s is shown in Figure 3.21. As we can see, though during the first 2s the flow generates only a few striations, the fluids are well mixed subsequently. This can be attributed to the fact that after the first 2s the fluid moves in the next 2s in a pattern that is not just a reversal of the pattern in the first two seconds. This mode is repeated four times during the 16s observation time resulting in a more chaotic flow.

3.1.4.2.6 <u>Results highlights</u>. This section highlights and interprets the results of our previous two-dimensional chaotic mixing in microfluidics.

The results from the simulations of this study show that by applying a sinusoidal potential boundary condition in the configurations with one or two electrode pairs and *B*=1.75T, a mixing performance, α = ~0.65 can be obtained, though there are some unmixed regions near the wall. The time periods *T* of the sinusoidal electrode potential, and the magnetic field intensity *B* both play strong roles in the mixing performance. However, to obtain even better mixing ($\alpha \geq$ ~0.9) with smaller values of *B*, more than one flow structure and more complex chaotic flow are necessary. The four electrodes

configuration with the electrode potential switching scheme implemented for Configuration (e) is a way to achieve complex chaotic flow. However, the choices for the number and locations of the electrodes, magnitude and orientation of the magnetic field intensity, type of electrolytes and the switching scheme for the sinusoidal potential imposed on the electrode pairs create a large set of options to choose from. Narrowing down the selections from the vast array of options would be dictated by the specific LOAC application [21-26]. The presented results suggest that even more complex flow structures can be created by straight forward extensions of the techniques used in this study. However, other aspects such as energy consumption, feasibility of fabrication and cost should be also taken into account when designing micro stirrers.

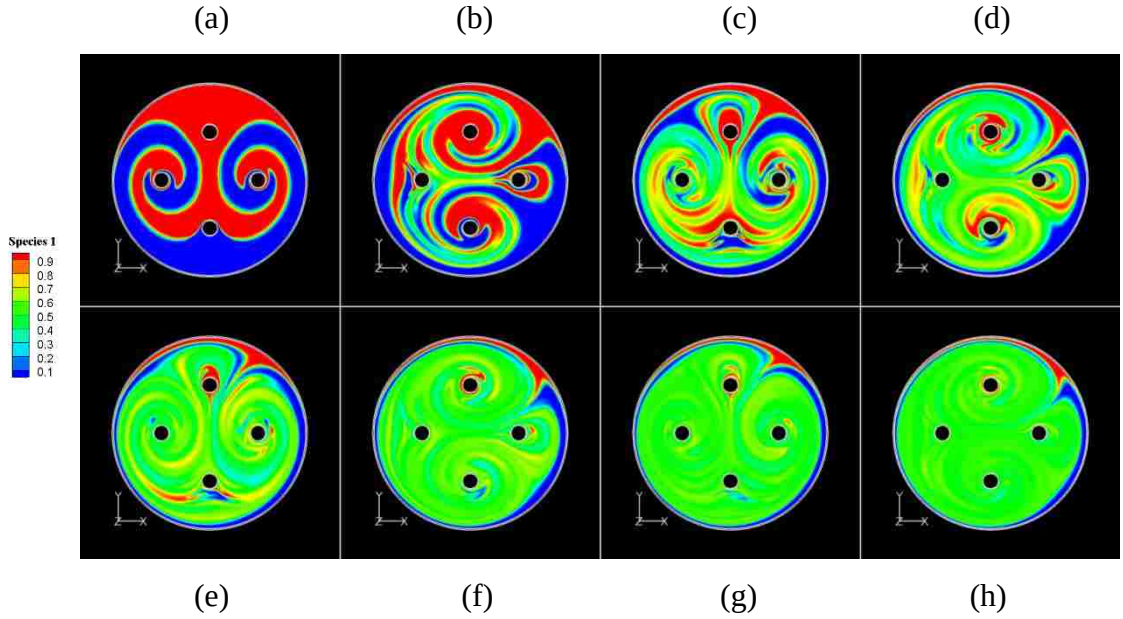

Figure 3.21. Time evolution of species mass fractions. T=4s, t_{max}=16s and B=0.5T. (a)-(h) represents from t=2s to 16s at 2s interval.

3.1.5. Conclusions. This section briefly concludes the result of two dimensional chaotic mixing using Electromagnetic/Lorentz force in microfluidics.

The results show that a certain level of mixing can be accomplished by the simple use of the sinusoidal potential boundary conditions on one pair of electrodes. Once a

potential is applied on the electrode pair in the presence of the magnetic field, the flow is driven to move clockwise and counter-clockwise periodically, by the Lorentz force. As a result, the interface between the fluids stretches rapidly, and therefore good mixing can be achieved. Parametric studies show that the time period has a strong influence on the mixing quality. Better mixing performance was observed for larger values of the sinusoidal potential wave period. Furthermore, for the cases considered, increasing the total operation time beyond where the mixing quality vs. time plot plateaus, the marginal increase in the mixing quality is small. Finally, as expected, the Lorentz force magnitude plays an important role in mixing performance. The mixing performance can be enhanced by increasing the current or the magnetic field strength, thereby increasing the Lorentz force.

The results show that a certain level of mixing can be accomplished by the simple use of the sinusoidal potential boundary conditions on one pair of electrodes. Once a potential is applied on the electrode pair in the presence of the magnetic field, the flow is driven to move clockwise and counter-clockwise periodically, by the Lorentz force. As a result, the interface between the fluids stretches rapidly, and therefore good mixing can be achieved. Parametric studies show that the time period has a strong influence on the mixing quality. Better mixing performance was observed for larger values of the sinusoidal potential wave period. Furthermore, for the cases considered, increasing the total operation time beyond where the mixing quality vs. time plot plateaus, the marginal increase in the mixing quality is small. Finally, as expected, the Lorentz force magnitude plays an important role in mixing performance. The mixing performance can be enhanced by increasing the current or the magnetic field strength, thereby increasing the Lorentz force.

By introducing two flow structures having opposite sense of rotation with the use of two electrode pairs, one can enhance mixing even better. By applying sine wave potentials with opposite signs on two working electrodes, two counter-rotational flows can be generated and better mixing quality obtained with a shorter mixing time (Scheme 1). This idea was then extended to 4 electrode pairs in which two pairs were active at a given time by switching between two schemes identical to Scheme 1. This scheme (Scheme 2) in which the electrode pairs are made active or inactive during a half period

according to the switching schedule shown in Figure 3.21, allows more complex chaotic advection that enhances mixing performance even with a smaller magnetic field intensity. In Scheme B, the unmixed regions near the wall found in previous cases are mostly eliminated.

Though excellent works on mixing in MHD flows have been reported previously by other researchers, our present work brings additional insights facilitated by the power of CFD simulations and high resolution graphics and animations. We have paid special attention to transient phenomena with our time-accurate simulations. The complex model geometries considered in our study have special relevance to real lab-on-a-chip applications. However, since the Lorentz force is volumetric, the force magnitude required to achieve the same velocity magnitude may increase when the cell has a finite height due to the additional viscous forces exerted by the floor and the ceiling, which scales with surface area, increase relative to the Lorentz force as the volume shrinks. Fortunately, our results suggest that the expected loss of mixing effectiveness due to the smaller velocity magnitude generated in three-dimensional geometries can be compensated by introducing complex chaotic advection. Future work will focus on studying mixing and micro-fluidic flow control in three-dimensions. To summarize, the simulation-based approach described in this work can provide an efficient tool to estimate the mixing quality in MHD micro-chips, and guide their optimal designs.

3.2. CHAOTIC MIXING IN THREE DIMENSIONAL MICROFLUIDICS

Though the previous section shows that mixing performance can be improved by using electromagnetic force in a two-dimensional microfluidics, three-dimensional simulations are needed to better understand the chaotic advection induced by the MHD effect with particle trajectory techniques. This section we extend the previous work into three-dimension. In this work, three dimensional numerical experiments are conducted in a microfluidic cell to investigate mixing performance by chaotic advection driven by electromagnetic force. An uncapped shallow cylindrical cell with gold electrodes deposited on the bottom surface is used. By judiciously choosing the number of active electrodes and the switching scheme, a “blinking vortex” and other types of chaotic motion are produced. Once the flow field is obtained by numerical solution of the Navier-

Stokes equations, particle trajectories-based analyses are conducted to investigate the degree of chaotic advection and mixing performance, including Poincaré maps, particle concentration maps, material line deformations and stretching maps. Comparisons to selected Stokes flow simulations are also included to show the advantages of using fully Navier-Stokes model.

3.2.1. Simulation Model Description. This section describes the simulation model and numerical method we used in this work. A three dimensional uncapped cylindrical microfluidic cell with a ring serving as the counter electrode and four disks serving as the working electrodes is used. The electrodes all made of gold are deposited on the bottom surface. This cylindrical cell has a radius r_1 = 3mm, the outer and inner radii of the ring counter electrode, respectively, are r_2 = 2.4mm and r_3 = 2mm, respectively, and four disks with a radius r_d = 0.16mm are located at 3, 6, 9 and 12 O'clock positions with their centers located on a circle concentric with the circular bottom face having a radius r_4 = 1mm. The cell height H = 0.5mm. The model geometry is shown in Figure 3.22.

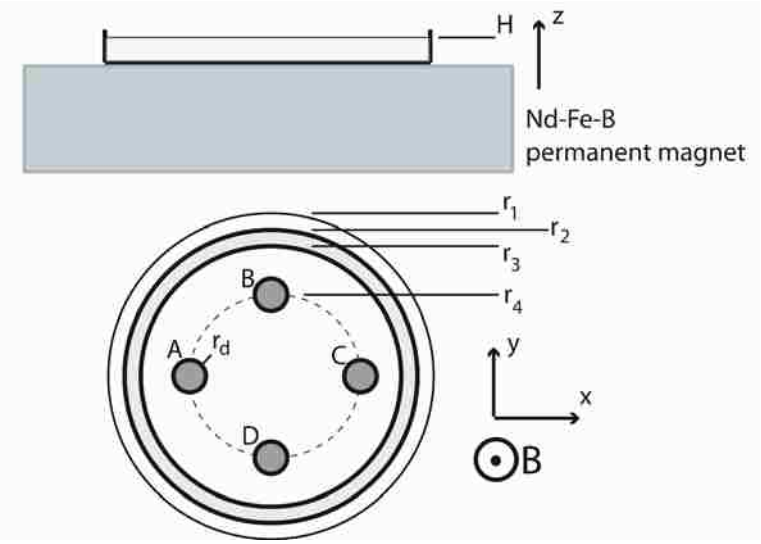

Figure 3.22. Cylindrical cell in top view and side view. One ring electrode and four disk electrodes are deposited on the bottom surface. The dimensions are: r_1 = 3 mm, r_2 = 2.4 mm, r_3 = 2 mm, r_4 = 1 mm, r_d = 0.16mm, H = 0.5 mm. The Nd-Fe-B permanent magnet is placed underneath the cell as shown. The direction of the magnetic field B is also shown.

By selectively activating the disks (working electrodes) labeled A, B, C and D, regular or chaotic flows can be achieved. For example, by switching on and off disks A and C and keeping disks B and D are at their floating potential, the "blinking vortex" can be reproduced. Because electrodes B and D are at their floating potential, no current will be flowing through them.

3.2.2. Simulation Setup. In all simulations, the cell is filled with NaCl solution. The simulation data are given in Table 3.1. Note that the potential ϕ for the electrode boundary condition in the simulations is the electric potential at the outer edge of the double layer. The electrical double layer is a very thin layer (~1 to ~100nm thick) across which the electric potential drops dramatically. The procedure for calculating the adjacent potential is shown in section 2.2 in detail. The externally applied potential we use in the simulations is ϕ_0 = 1V, and the adjacent potential is rounded off to 0.04V after the calculation.

Table 3.1. Simulation data

Density (kg/m^3)	1000
Viscosity (kg/(m.s))	0.001
NaCl solution concentration (M)	0.1
Electrode potential difference (V)	0.04
Solution conductivity (S/m)	1.29
Magnetic density flux (T)	0.36

The magnetic field is in +z direction with an intensity B = 0.36T. Previous experimental studies have shown that a uniform magnetic field in the cell region of the size similar to ours is possible by using a rectangular ~25 mm x ~25 mm x ~12.5 mm, Nd-Fe-B permanent magnet [11]. Their measurements showed a maximum variation of ~5% in B_z over the cell height of 650 μm. Note that our cell height, H = 500 μm. Due to the larger lateral dimension of the magnet compared to the 3 mm radius of our circular

cell floor, variation in the B_x and B_y components across the cell diameter would be much smaller.

3.2.2.1 Initial and boundary conditions. The initial and boundary conditions for the three-dimensional simulations are quite similar with those in two-dimensional ones in the previous section.

As we mentioned, the "blinking vortex" is a simple model that provides chaotic advection in Stokes flow proposed by Aref [16]. Inspired by the "blinking vortex" model problem, we have designed the disk and ring configuration. By activating the ring and disk A during the first half of the period, a clockwise rotating flow is generated, which can be treated as an agitator in Aref's model [16]. During the second half of the period, deactivating disk A while activating disk C produce another clockwise rotating flow on the right, which can be considered as another agitator. This process is repeated over several periods to achieve chaotic flow. Both disks B and D are at their floating potential in these simulations. Mathematically, the potential boundary conditions for the Laplace equation are

$$\begin{cases} \phi_{\mathrm{A}} = 0.04\mathrm{V} \quad \phi_{\mathrm{C}} = 0 \quad kT < t < kT + \dfrac{T}{2} \\ \phi_{\mathrm{A}} = 0 \quad \phi_{\mathrm{C}} = 0.04\mathrm{V} \quad kT + \dfrac{T}{2} < t < (k+1)T \end{cases} \tag{3.9}$$

where k =0,1,2,… is an integer and the resulting flow field is periodic in time with period T. The time period T is an important parameter which determines whether the flow is regular or chaotic. We call it scheme 1.

In order to create more chaotic flow which will cause more efficient mixing, we introduce another on and off switching scheme that employs all four working electrodes. The corresponding electric potential boundary conditions are

$$\begin{cases} \phi_{\mathrm{A}} = 0.04\mathrm{V} \quad \phi_{\mathrm{C}} = -0.04\mathrm{V} \quad \nabla\phi_{\mathrm{B}} = \nabla\phi_{\mathrm{D}} = 0 \quad kT < t < kT + \dfrac{T}{2} \\ \nabla\phi_{\mathrm{A}} = \nabla\phi_{\mathrm{C}} = 0 \quad \phi_{\mathrm{B}} = 0.04\mathrm{V} \quad \phi_{\mathrm{D}} = -0.04\mathrm{V} \quad kT + \dfrac{T}{2} < t < (k+1)T \end{cases} \tag{3.10}$$

we can it scheme 2. By doing so, during the first half period, disks A and C generate a pair of counter-rotating flows, and then by activating disks B and D during the second

half period, another pair of counter-rotating flows is generated. For simulations of this nature, the choices are infinite. Here we do not address the optimization of the schemes, which is beyond the scope of the present work. However, our experience shows that various switching schemes lead to interesting flow patterns, indicating the strong dependence of mixing performance on the number of electrodes and the switching schemes. One important contribution of this work is in the use of larger number of electrodes and more complex switching schemes than used by previous investigators.

Zero current flux ($\nabla\phi = 0$) boundary condition is specified on all surfaces except the active electrodes. This is also the boundary condition for the electrodes at their floating potentials. For the hydrodynamic boundary condition, the no-slip boundary condition is used at the walls and the top surface is treated as a free surface with no motion perpendicular to it.

3.2.2.2 Discrete phase model. In order to study and visualize the chaotic advection, massless particles trajectories need to be calculated at each time step. And this process can be achieved by integrating advection equation (eqn. 2.16) through DPM (Discrete phase model) in Fluent.

In order to integrate the advection equation (eqn. 2.16), the Discrete Phase Model (DPM) available in Fluent [46] is used. In DPM, massless particles are injected into the computational domain at specific initial positions selected by the user. After the main solver yields the flow field, advection equation (eqn. 2.16) is integrated by using a 5^{th} order Runge-Kutta method to obtain the successive particle positions. More information can be found in FLUENT theory tutorials. The next section presents the analyses on mixing performance including the Poincaré map, concentration of numerical particles, deformation of material line and stretching plots.

3.2.3. Results.

3.2.3.1 Navier-Stokes flow versus Stokes flow. As we mentioned in the introduction part 1.4., two-dimensional Stokes flow was mostly used to investigate the chaotic advection in microfluidics because the two-dimensional kinematics of advection by an incompressible flow is equivalent to the Hamiltonian dynamics of a one degree of freedom system which has been well understood as chaotic since the mid-1960s. These

observations have helped build the theoretical bridge between chaotic advection in fluid mechanics and chaos in classical mechanics.

In order to present the advantages of our models and techniques, the three-dimensional full Navier-Stokes simulation results are compared to the Stokes flow results under potential step for 3 values of the Reynolds number Re_H in Figure 3.23. The details about how to obtain Stokes flow in Fluent is shown in Appendix B.

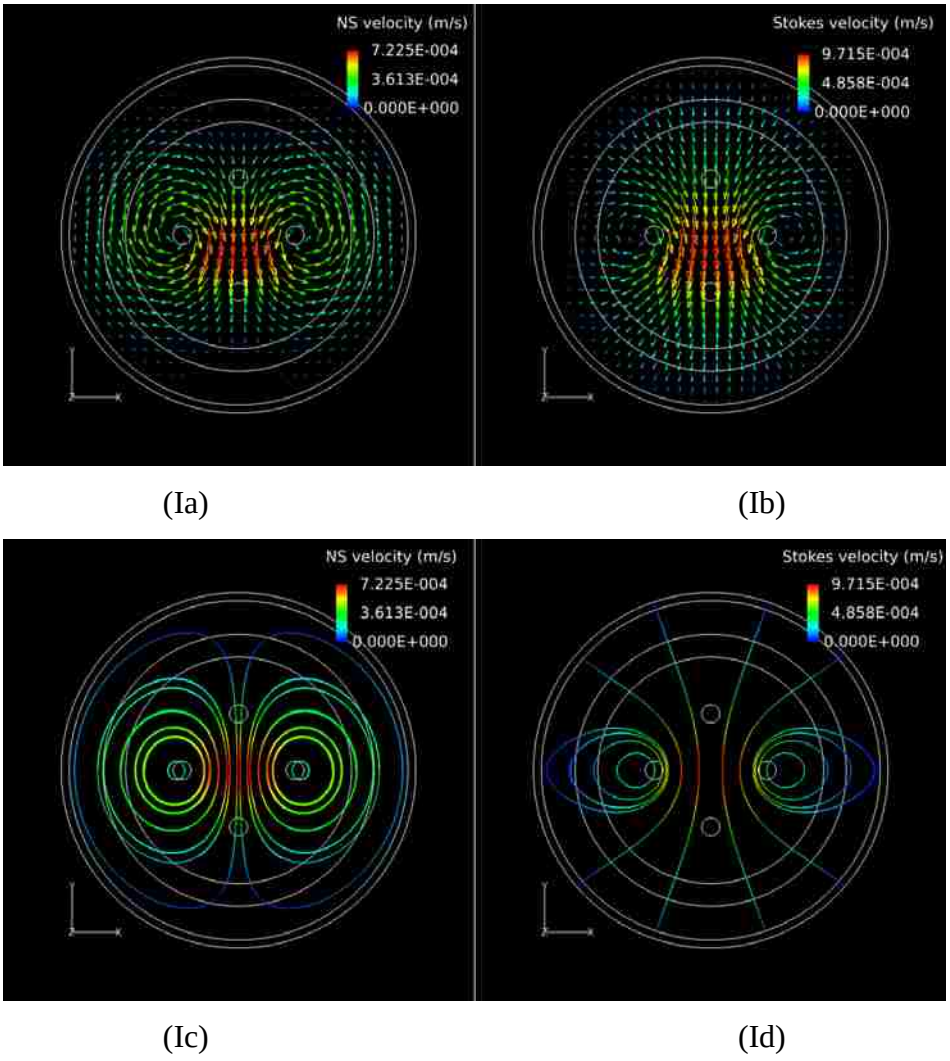

Figure 3.23. Velocity vector maps and streamlines from Navier-Stokes ((a) and (c)) and Stokes flow ((b) and (d)). in z=0.4mm plane. Potential step solution at *t*=8s. (I): ReH = 0.1, (II): ReH = 1.07, (III): ReH = 14.98.

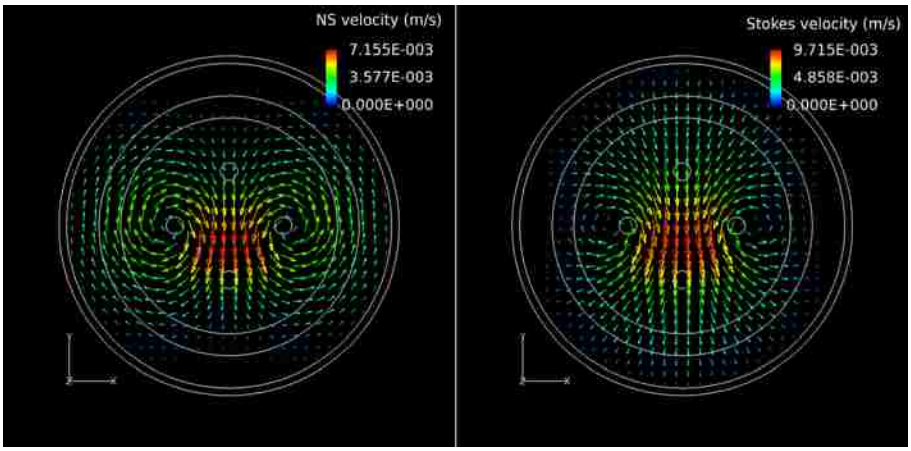

(IIa) (IIb)

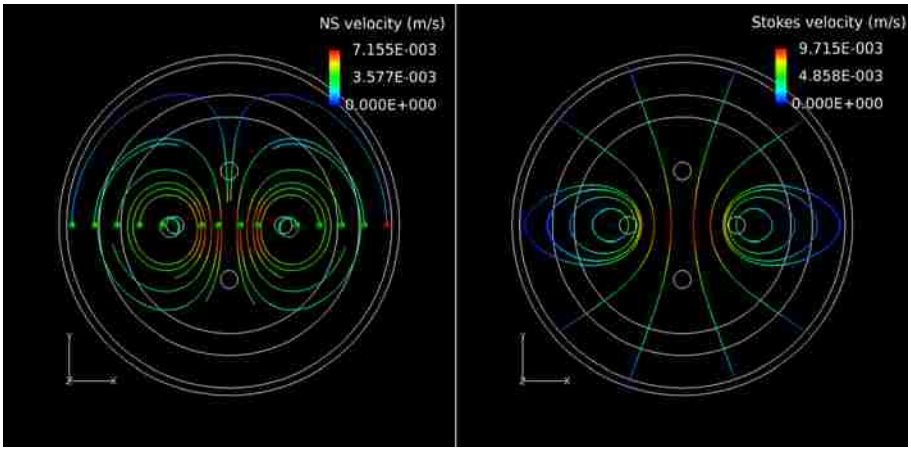

(IIc) (IId)

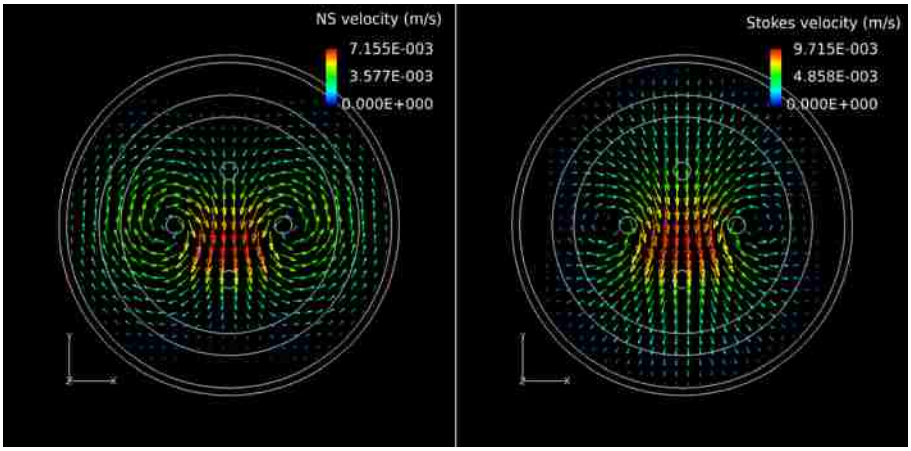

(IIIa) (IIIb)

Figure 3.23. Velocity vector maps and streamlines from Navier-Stokes ((a) and (c)) and Stokes flow ((b) and (d)). in z=0.4mm plane. Potential step solution at *t*=8s. (I): ReH = 0.1, (II): ReH = 1.07, (III): ReH = 14.98 (cont.).

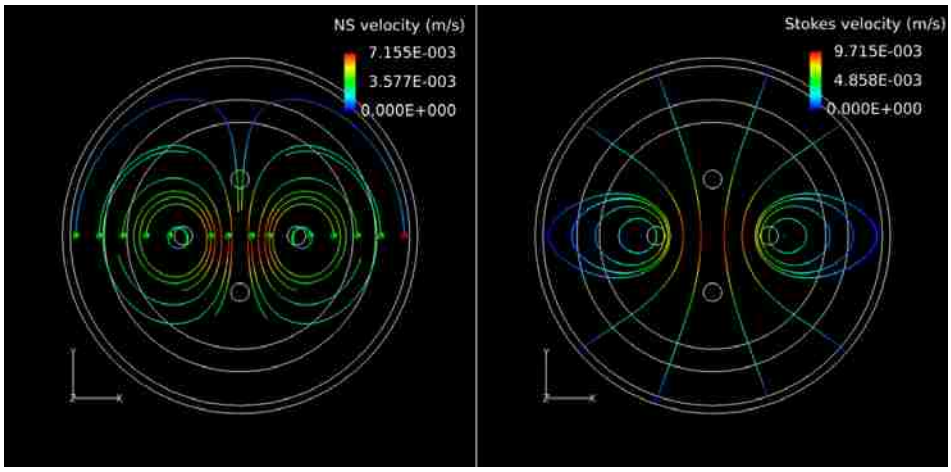

(IIIc) (IIId)

Figure 3.23. Velocity vector maps and streamlines from Navier-Stokes ((a) and (c)) and Stokes flow ((b) and (d)). in z=0.4mm plane. Potential step solution at *t*=8s. (I): ReH = 0.1, (II): ReH = 1.07, (III): ReH = 14.98 (cont.).

The potential difference between the electrode pair A and C is applied to different values in order to obtain difference magnitude of electric current and the rest electrodes and wall are set to be insulated. The corresponding equipotential lines and electric current flux are shown in Figure 3.24. The velocity vectors and the streamlines at t = 8s show clear differences between the two as the Reynolds number increases. The loss of symmetry about the y = 0 plane is clear in the Navier-Stokes results compared to the Stokes flow results. These results show similarity to those from flow over a cylinder. When Stokes flow assumptions are valid, the streamlines show symmetry between the upstream. The explanation for this behavior is that Stokes flow is dominated by the diffusion of vorticity, whereas at higher Reynolds numbers, vorticity is swept downstream by convection resulting in loss of symmetry, also evident in Figure 3.23 (III) for Re_H = 14.98. However, since these results are given only to demonstrate the differences between the two models, a comparison of mixing quality would require simulations using Schemes 1 and 2 for larger values of t, which is beyond the scope of this paper.

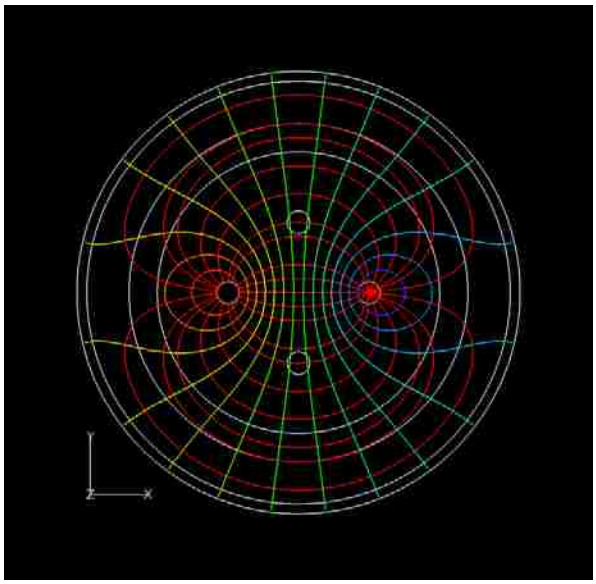

Figure 3.24. Equipotential lines and current flux lines from potential step simulation in z=0.4mm plane. Current paths are in red.

3.2.3.2 Overall features of flow and electric field. This subsection shows the overall feathers of flow field and electric field for Scheme 1 and 2.

Scheme1: In this scheme, disks A and C are activated. Figure 3.25 below shows velocity vectors (a), velocity profile along the *x*-axis (b), electrical potential contours and ionic current flux vectors (c) in the z = 0.4 mm plane, and the potential contours, current flux lines, velocity vectors in the $y = 0$ plane (d), and velocity profile in the $x = 0$ plane (e), for case $T = 4$s at the end of the first half period. From Figures 3.25 (c) and (d), in top view and side view, respectively, the electric potential has the largest value at disk A and decays toward disk C and the ring. The ionic current flux vectors are shown in Figures 3.25 (c) and (d), and the ionic current flux lines which are perpendicular to the equipotential lines are shown in Figure 3.25 (c). From Figure 3.25 (d), we see that that current flux vectors are pointing outward from the disk, and with the magnetic field vector **B** pointing in the +*z* direction, a clockwise Lorentz force is generated by virtue of the cross-product rule and causes a clockwise rotating flow as shown in Figure 3.25 (a). As we expect, we see from Figure 3.25 (d) that the current flows from the activated disk A to the ring and disk C. The total current has a value $I = 30.1\mu$A. Figure 3.24 shows the

potential contours and current lines when electrodes A and C are active and all other electrodes are at their floating potential.

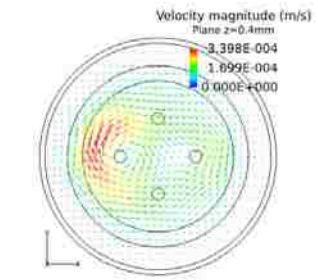

(a)

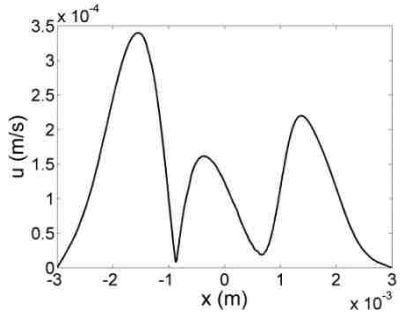

(b)

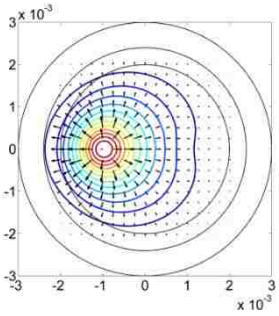

(c)

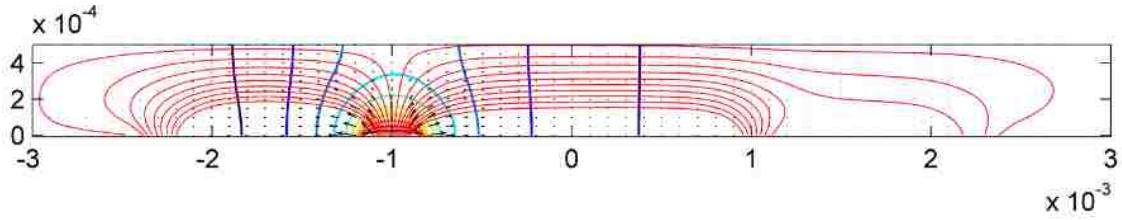

(d)

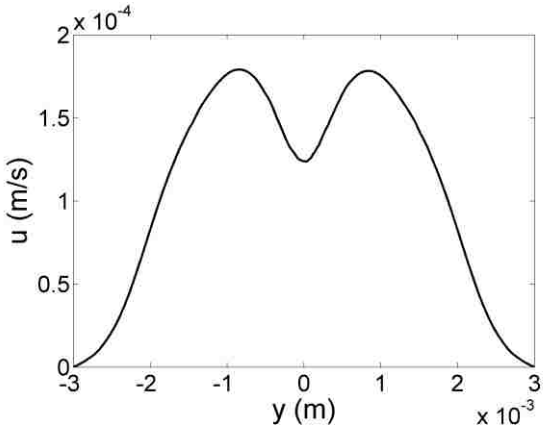

(e)

Figure 3.25. (a): velocity vectors. (b): Velocity magnitude vs. x. (c): electrical potential contours and current flux vectors (black) in plane z = 0.4mm. (d): electrical potential contours (blueish), current flux vectors and current flux lines (red) in cross-sectional view in plane y = 0. x and z units are m. (e): Velocity magnitude vs. y. T = 4s.

Scheme 2: In order to create more chaotic flow which will cause more efficient mixing, we introduce another on and off switching scheme that employs all four working electrodes. The corresponding electric potential boundary conditions are in eqn. (3.10). By doing so, during the first half period, disks A and C generate a pair of counter-rotating flows, and then by activating disks B and D during the second half period, another pair of counter-rotating flows is generated. For simulations of this nature, the choices are infinite. Here we do not address the optimization of the schemes, which is beyond the scope of the present work. However, our experience shows that various switching schemes lead to interesting flow patterns, indicating the strong dependence of mixing performance on the number of electrodes and the switching schemes. One important contribution of this work is in the use of larger number of electrodes and more complex switching schemes than used by previous investigators. Figures 3.26 present the flow properties for Scheme 2 at the end of the first half period. Figure 3.26 (c) shows the equipotential contours and the current flux vector map at the end of the first half period, while the corresponding current flux lines are shown in Figure 3.26 (d) in cross-sectional view.

The root mean square velocity and the maximum velocity in the computation domain for schemes 1 and 2 are U_{rms}~0.1mm/s and U_{max}~0.5mm/s, which gives the Reynolds number based on U_{rms} , $\text{Re}_H = U_{\text{rms}}H/\nu \sim 1$. For this order of magnitude of Re_H, the flow is clearly laminar which guarantees that the chaotic characteristics arising in the cases considered in this study are not contributing to the development of turbulent flow. The Hartmann number appropriate for the present work can be defined as $Ha = \sqrt{\sigma\phi BH / \mu U_{rms}}$, the square root of the ratio M of the Lorentz force to viscous force. In our case, Ha ~1 which indicates that both the forces exert more or less equal influence on the flow. Though other researchers investigated the impact of Hartmann number on chaotic advection in microfluidics, it is reasonable to assume that the Lorentz force and viscous force are in the same order due to the small size of the microfluidics, the weakly conductivity of the supporting electrolyte, and the small applied potential in order to avoid the bubble generation and degradation of electrodes.

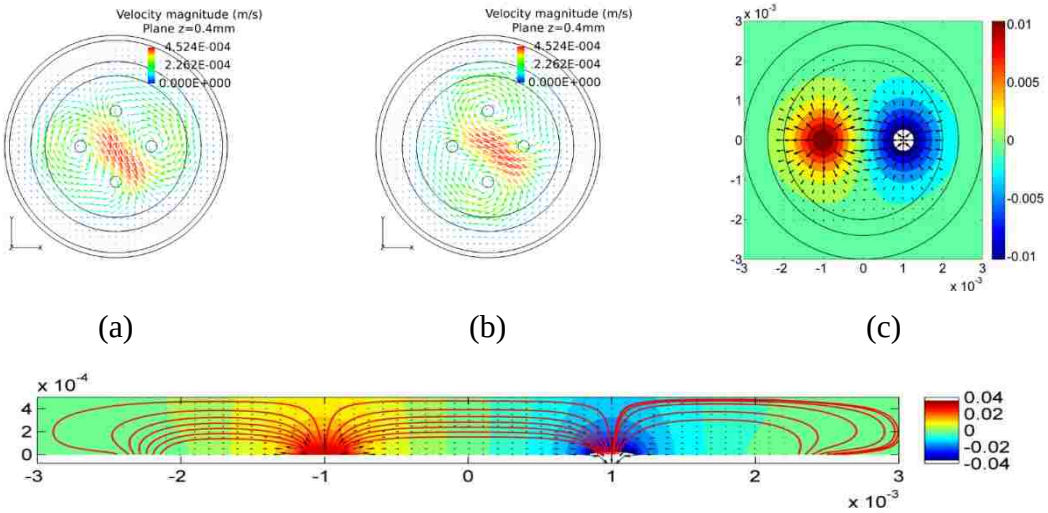

Figure 3.26. (a), 3(b): velocity vector maps at the end of the first and second half periods, respectively. (c): electric potential contours and current flux vector map in z=0.4mm plane at the end of the first half period. (d): electrical potential, current flux vector map and current flux lines in cross-sectional view in y=0 plane. T=2s.

3.2.3.3 Poincaré maps. A Poincaré map shows the long term behavior of trajectories of several different particles starting from their initial positions. If the initial points are selected appropriately they will indicate the behavior of all particles originating from everywhere in the domain. After the initial points are selected, the new particle positions at the end of each time period will be recorded after each time period and then all particle positions at each time period will be aggregated in one map. Generally, there are two types of behavior a Poincaré map can indicate, 'regular' and 'chaotic'. A 'regular' behavior implies that the particle trajectories are confined to regular curves. While a 'chaotic' behavior is indicated by the particle positions that are scattered throughout the domain. It is worth mentioning that a Poincaré map shows regions where the initially placed particles go through or are forbidden from entering regardless of how many time periods are considered. If the system is chaotic, the forbidden regions will get smaller and finally disappear as the number of periods increase.

To create Poincaré maps, five initial points are selected as follows: P_1(x=0.2, y=0, z=0.4)mm, P_2(x=0.5, y=0, z=0.4)mm, P_3(x=0.8, y=0, z=0.4)mm, P_4(x=1.2, y= 0,

z=0.4)mm and P_5(x=1.5, y=0, z=0.4)mm (Figure 3.27 (a)). Figures 3.27 (b) – (f) show the Poincaré maps with different time period T=1s, 2s, 4s, 8s and 10s. The corresponding elapsed periods are shown in Table 3.2. From Figure 3.27 (b), we see regular behavior for case T=1s since all five tracks are confined in five distinct regular curves. Note that if T=0, the system yields the steady two fixed-agitator system with its pathlines and streamlines coinciding. The streamlines of the two fixed-agitator system are similar to those in Figure 3.27 (b). Therefore, as the time period T approaches zero, the system will look more and more like the two fixed-agitator system, hence the similarities between the Poincaré map in Figure 3.27 (b) and the streamlines of the two fixed-agitator system. For case T=2s, the system becomes a little more chaotic since the innermost particles start to scatter to the outer region, hence the innermost regular curves begin to become more irregular while the outer curve still remains regular. This behavior has good agreement with the results from Aref's "blinking vortex" experiments [16]. For case T=4s, the system becomes more chaotic with the particles appearing mostly everywhere in the part of the domain inside the ring. However, two distinct islands mostly devoid of particles can be found. The appearance of the particle-free islands indicates that the particles placed at the locations to create the maps do not enter the islands regardless of how many periods are considered. This is likely to be due to the disk electrode being of finite size whereas Aref [16] used point vortices. Furthermore, one can see that the particles distinguished by their colors are restricted in some specific tracks though some hint of dispersion can be recognized (black circles). However the existences of this kind of clustering is not found neither in Aref's [16] results nor in Bau's results [21], which is not surprising since Aref [16] and Bau [21] relied on the results of their approximate analytical models which might have missed some features that appear in the present CFD simulations based on the full Navier-Stokes equations. It is reasonable to expect that when the full Navier-Stokes equations are considered, the system would be more prone to chaos since non-linear systems have a greater tendency toward chaos. For cases T=8s and 10s, the system can be considered globally chaotic, and the particles are dispersed almost everywhere in the region inside the ring, and no distinct clusters are found.

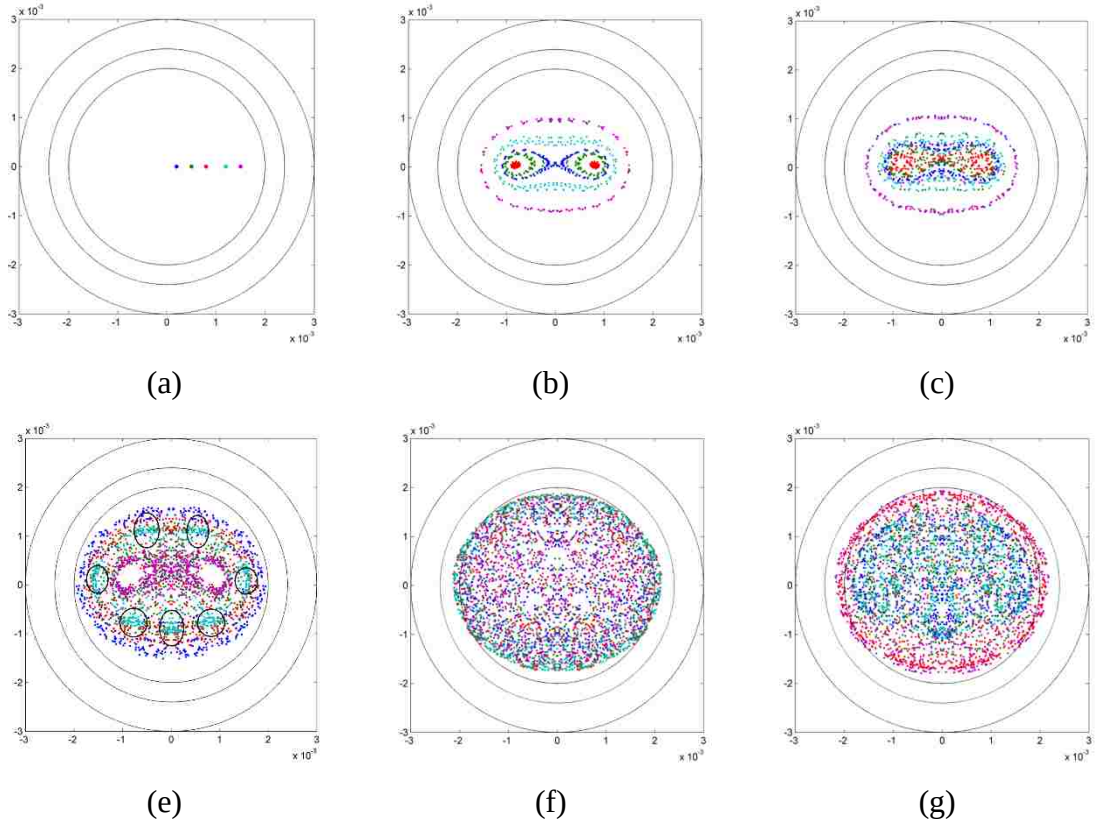

Figure 3.27. Poincaré maps for different time periods T in plane z=0.4 mm. (a): Initial conditions, (b): *T*=1s, (c): *T*=2s, (d): *T*=4s, (e): *T*=8s and (f): *T*=10s.

Table 3.2. Number of elapsed periods for each case in Figures 3.27(b)-(f)

T(s)	Number of periods (n)
1	75
2	100
4	300
8	400
10	400

3.2.3.4 Concentration of numerical particles. In order to quantify mixing performance, we designate the two halves of the domain randomly seeded with particles

of two different colors. Totally 500,000 black and grey numerical particles which represent two non-diffusive dyes are seeded into the z=0.4 mm plane. The black and grey particles are initially distributed evenly in the left and right halves (Figure 3.28 (a)) of the domain, and then the particles are tracked at each time step through integrating the advection equation (eqn. 2.16). Figures 3.28 (b) – (f) present the particle distributions for different time periods T at t=200s. A good agreement between the particle distribution maps and Poincaré maps can be found. For case T=1s (Figure 3.28 (b)), we see a regular structure which is very similar to that in the corresponding Poincaré map. Obviously, for this case, the mixing is not efficient since the black and grey particles are segregated into bands. For case T=2s (Figure 3.28 (c)), the situation becomes better since some particles in the interior begin to scatter and mix in the region enclosing the two disks, which is also reflected in the corresponding Poincaré map (Figure 3.27(c)). For case T=4s, mixing performance is higher, and the mixed region is larger. It is interesting that the islands seen in the Poinaré maps also appear in the particle distribution maps. For cases T=8s and 10s, the mixed region continues to grow. Gopalakrishnan and Thess [26] have presented similar maps for a range 0 -1000 of M, the square of the Hartmann number defined in section 3.2.3.2. As their results show, mixing performance improves at higher values of M. For our system $M \sim 1$, and the flow is driven only by the Lorentz force without any inflow or outflow boundaries. As a result, only a qualitative comparison between the two is possible, which shows that the concentration maps of the passive scalars are similar in both.

After obtaining the distribution of the black and grey particles numerically, the local species concentration can be calculated by accounting the number of black and grey particles in each mesh box. In this work, the resolution of the mesh is discretized into 200×200 of the 30μm side length. The local concentration C then can be calculated by the expression shown below

$$C_{\text{black}} = n_{\text{black}} / (n_{\text{black}} + n_{\text{grey}}) \tag{3.11}$$

where the n_{black} and n_{grey} are the number of black and grey particles.

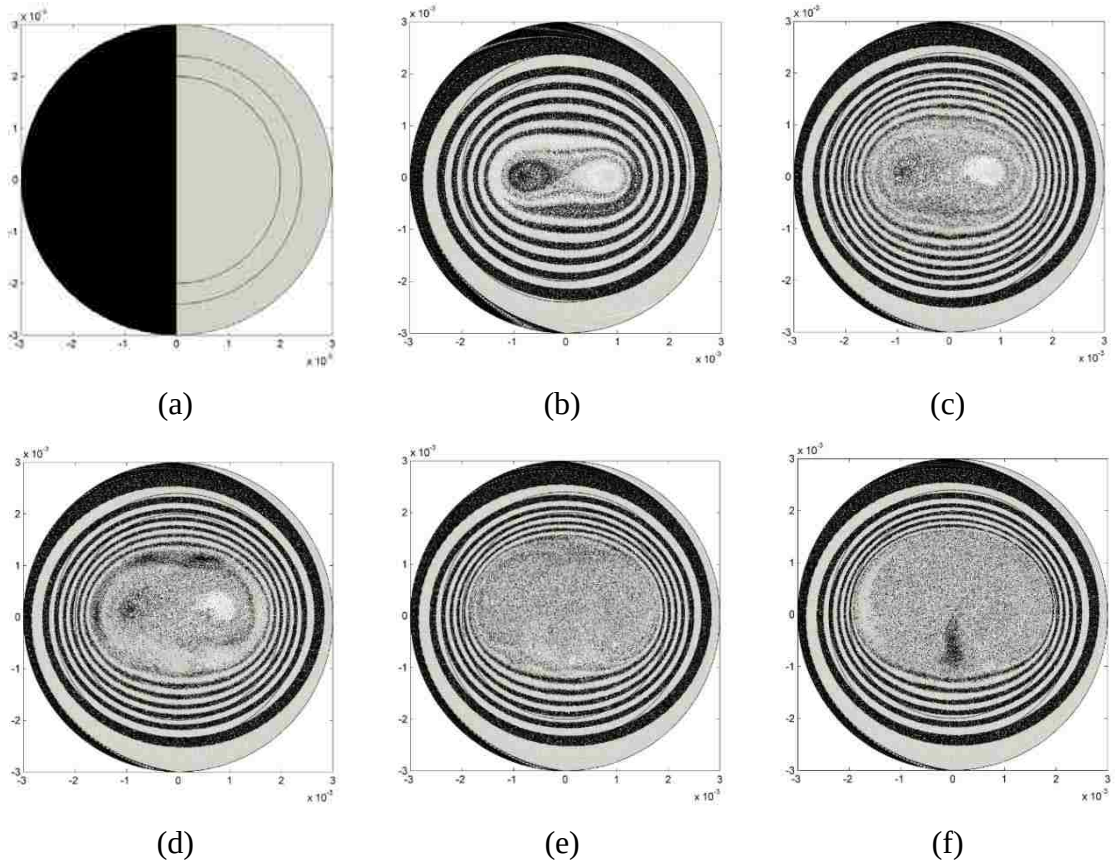

Figure 3.28. Numerical particle distributions for different time period T at t=200s at plane z=0.4 mm. The black and grey particles represent two non-diffusive dyes. (a): Initial distribution, (b): *T*=1s, (c): *T*=2s, (d): *T*=4s, (e): *T*=8s and (f): *T*=10s.

Figure 3.29 shows the corresponding species concentration contour for *T*=1s, 2s, 4s, 5s, 8s and 10s at *t*=200s while the red and blue colors represent two different species seeded by black and grey particles. These figures provide us a better understanding of how good the mixing is since the region with green color (*C*=0.5) indicates a good mixing. It is easy to see that the good mixing region is increasing when *T* is increasing. Furthermore, the concentration contour here gives us an alternative way to understand the islands in the corresponding Poincaré maps. As we mentioned before, the islands are the regions which the initial conditions are forbidden from entering into. From Figures 3.29 (c) and (d), we can find that the blue color (grey particles) inside the correspond island on the right are not allowed to get into the left island in which the red color (black particles)

is and vice versa. Therefore, inside the islands no mixing occurs even though very good mixing can be found surrounding these islands. And one may find that there are some unmixed patterns outside the islands which are consistent with the black circled regions in the corresponding Poincaré maps. Besides, for case T=10s, one may find two unmixed stripes which are not reflected by the corresponding Poincaré map. That is because the species concentration maps only run for 200s (20 periods for T=10s) while the Poincaré maps run for hundreds periods (Table 3.2). It is reasonable to expect that these two unmixed stripes will vanish if total periods increase.

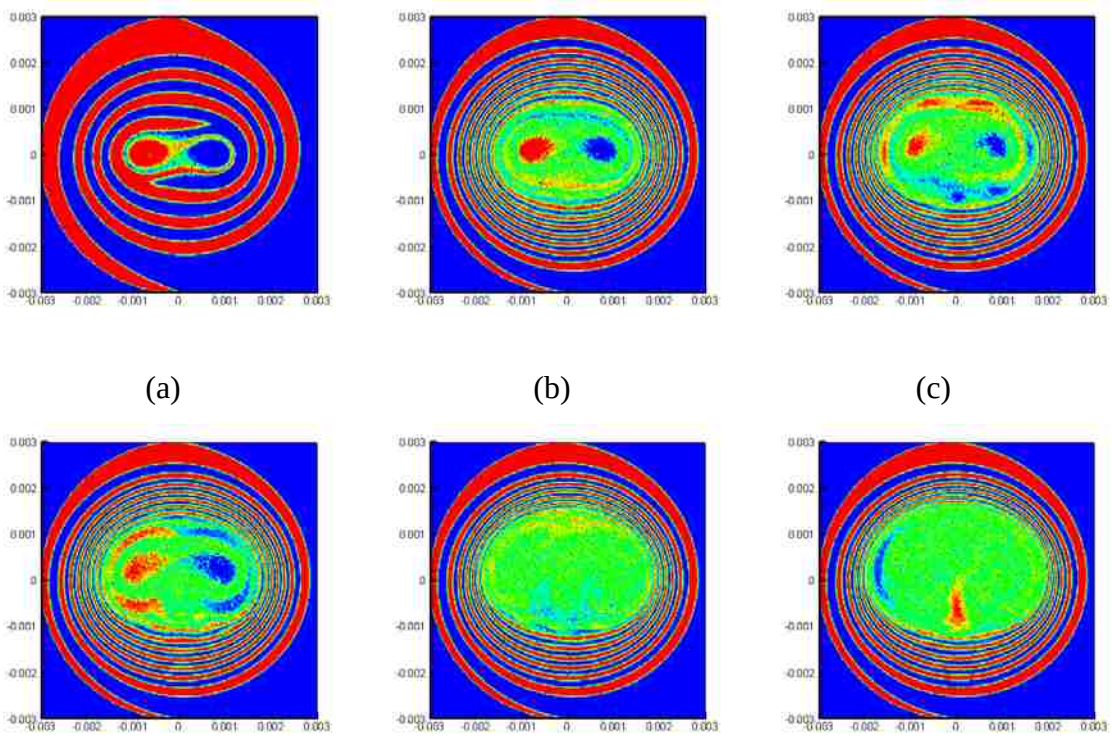

(a) (b) (c)

(e) (f) (g)

Figure 3.29. Corresponding species concentration contours obtained from the particle color method in Figure 3.28. (a): T=1s, (b): T=2s, (c): T=4s, (d): T=5s, (e): T=8s and (f): T=10s. All cases are presented at t=200s.

In order to quantify the mixing performance, a parameter called mixing quality has been defined which is the same as that in our 2D case,

$$\alpha(t) = 1 - \frac{\delta^2(t)}{\delta^2(0)} \tag{3.12}$$

where $\delta^2(t)$ is the standard deviation of the dimensionless concentration C at time t which can be expressed as:

$$\delta^2(t) = \iiint_s \left[C(x,y,t) - \bar{C} \right]^2 dxdy \tag{3.13}$$

where $C(x,y,t)$ is the local concentration that varies with time and $\bar{C}$ is the constant average concentration. The concentration is computed from the particle number density displayed in Figure 3.28.

Table 3.3 lists the mixed area (mm^2) and its percentage of the total area for different cases in plane z=0.4 mm. Figure 3.30 shows the time-evolution of mixing quality $\alpha(t)$ for different values of T. The set of curves shows that increasing the time period T improves $\alpha(t)$. The reason why the mixing quality is not close to unity even in the best case (T = 10s) for which it is slightly less than 0.4, is that the integration domain in equation (3.13) is the entire rectangular cut surface in the vertical plane passing through the center. However, mixing only take place in the region inside the ring counter electrode even for the best case, and little mixing occurs near the side walls even for the longest time, t=200s (Figure 3.30).

Table 3.3. Mixed area in plane z=0.4 mm at t=200s for T ranging from 1s to 10s

Time period T (s)	Mixed area (mm^2)	% of total area
1	0.523075E-05	18.5
2	0.124047E-04	43.9
4	0.130527E-04	46.2
8	0.135999E-04	48.2
10	0.140859E-04	49.8

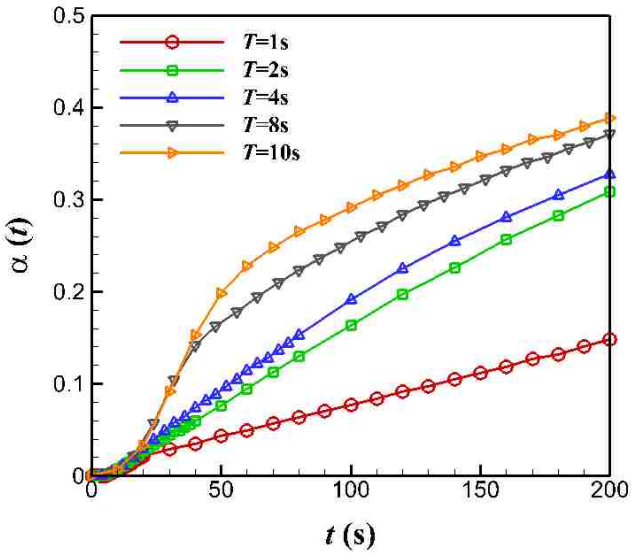

Figure 3.30. Evolution of mixing quality with time t for different time periods *T* at plane z=0.4 mm

3.2.3.5 Stretching and deformation of material lines. Dramatically stretching and folding of material lines is another feather of chaotic advection [18]. In this subsection, an elliptic material line is placed at the center of the domain at plane *z*=0.4mm. Figure 3.31 below shows the stretching and deformation of this material line for different *T*=1s, 2s, 4s, 8s and 10s at *t*=*T*, 5*T*, 10*T* and 20*T*. For cases *T*=1s and 2s, the materials have been stretched only a little a bit, and the structures show the regular patterns which can be found in the corresponding Poincaré maps. For case *T*=4s, the material line begins to spread throughout the plane and the islands can be found as well. For cases *T*=8s and 10s, the material line diverges throughout the domain only after 5 time periods.

The stretching of the material line can be quantified by dividing the line's length *l* to its initial length l_0, the expression is given by

$$l / l_0 = \frac{1}{l_0} \sum \| l_i \| \tag{3.14}$$

where l_i are the vectors defined between the two interconnected particles. Figure 3.32 presents the temporal evolution of the stretching l/l_0 for different time periods T. It shows that increasing T can increase the stretching immediately. For cases T=1s and 2s, the stretching history seems to be linear, and even after 100 periods for T=1s, the stretching is still not efficiently. For large time period T=8s and 10s, stretching grows rapidly especially for T=10s.

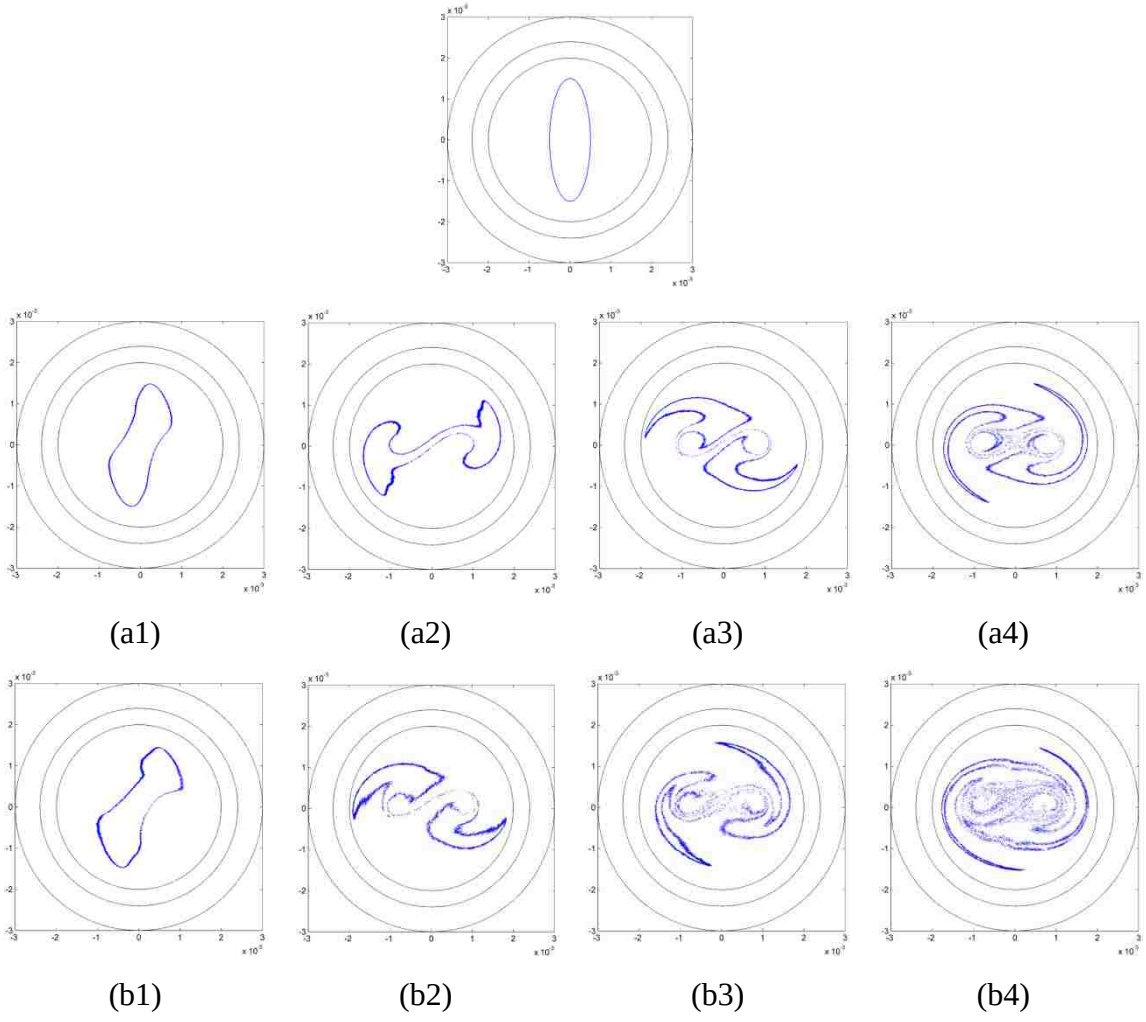

Figure 3.31. Elliptic material line deformation evolution for different time period T. (a): T=1s, (b): T=2s, (c): T=4s, (d): T=5s, (e): T=8s, (f): T=10s. (1-4) represents t=T, 5T, 10T and 20T successively. The upmost is the initial condition of the material line.

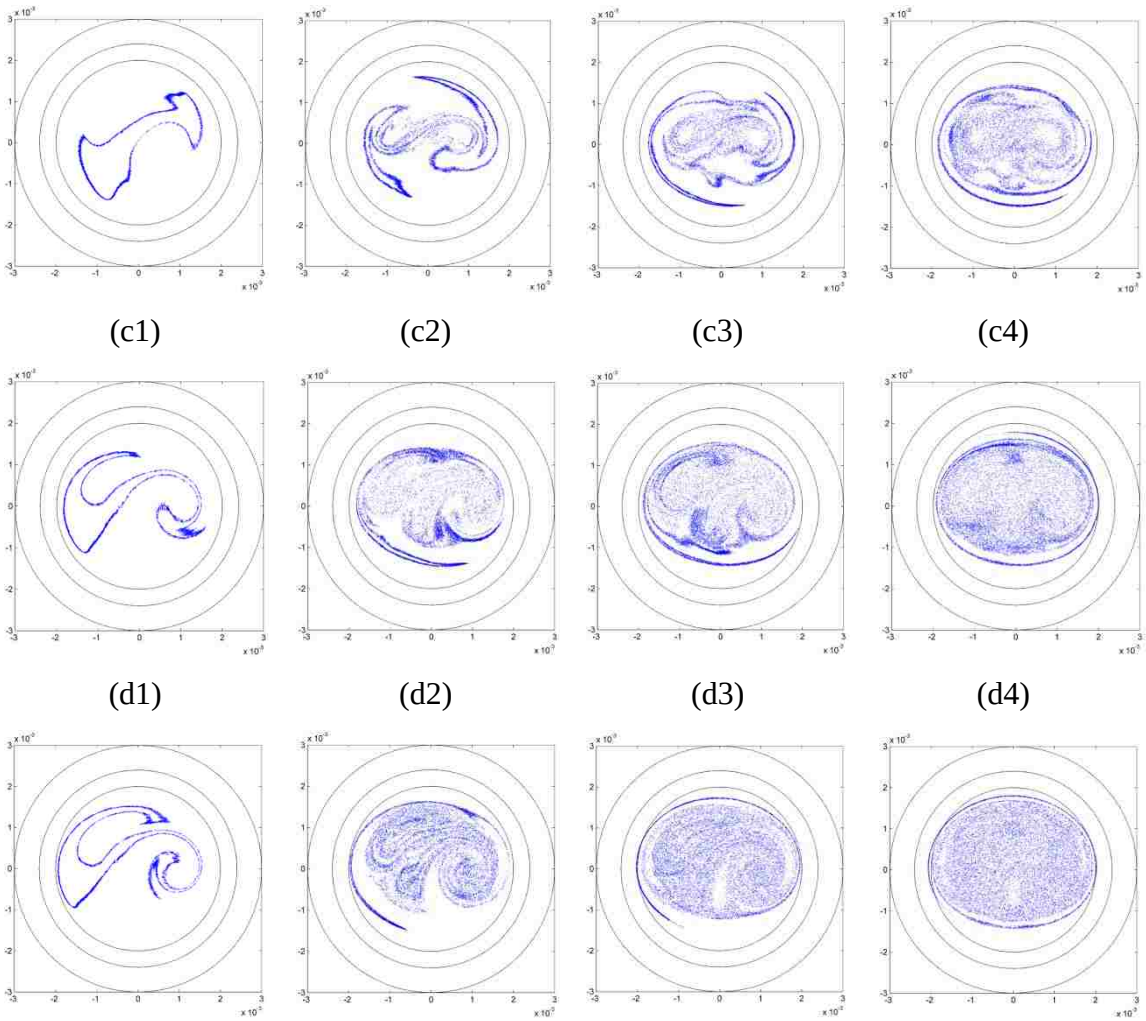

(c1) (c2) (c3) (c4)

(d1) (d2) (d3) (d4)

(e1) (e2) (e3) (e4)

Figure 3.31. Elliptic material line deformation evolution for different time period *T*. (a): *T*=1s, (b): *T*=2s, (c): *T*=4s, (d): *T*=5s, (e): *T*=8s, (f): *T*=10s. (1-4) represents *t*=*T*, 5*T*, 10*T* and 20*T* successively. The upmost is the initial condition of the material line (cont.).

3.2.3.6 Stretching plots. As we discussed, the early stage for mixing is that the fluid elements must be stretched and folded efficiently in order to decrease the width of the fluid elements to a specific level. And one character of chaotic motion is the exponential growth of initial conditions or in another word, an asymptotic divergence of initial conditions. Therefore, it is reasonable to expect that the vectors initially seeded into the flow domain can be stretched to a length several orders of magnitude greater than

their initial length if there is a chaotic flow. And, people should be interested to know where the most stretching occurs since these places are where the most efficient mixing could happen.

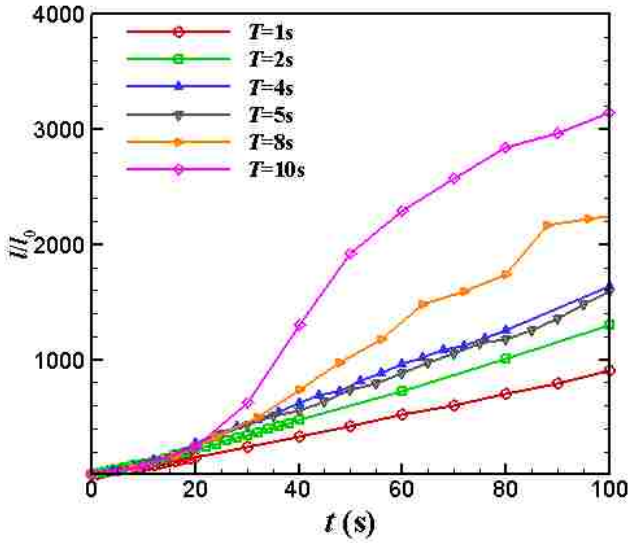

Figure 3.32. Temporal evolution of stretching of material line with different time periods *T*.

In order to determine the stretching in the flow domain, consider an infinitesimal fluid element [18]. The stretching of the infinitesimal arbitrary vector on that fluid element then can be computed if we know the deformation tensor. The deformed vector *dx* at time *t* is given by

$$dx(t) = F(t) \cdot dx_0 \tag{3.15}$$

where dx_0 is the initial vector on that fluid element, and $F(t)$ is the deformation tensor which can be solved from the partial differential equation below

$$\dot{F} = (\nabla \mathbf{V})^T \cdot F \tag{3.16}$$

where at t=0, $F(t=0)$ is an identity matrix, and **V** is the velocity vector. By doing so, the stretching on that fluid element at time t can be defined as the ratio of the length magnitude of dx and dx_0,

$$\lambda = \|dx\| / \|dx_0\| \tag{3.17}$$

From Eqn. (3.16) we find that the deformation tensor follows the Lagrangian view point, because the infinitesimal fluid element moves to a new position after the next time step dt, and the time dependent deformation tensor $F(t)$ is computed upon the gradient of velocity vector locally. Therefore, we should determine λ through numerous discrete points in the flow domain. To do that, first we discretize the flow domain into 200×200 of the 30μm side length cells and then seed a large amount of passive particles homogeneously into the flow domain and then to compute the stretching on each particle. In each cell, we can count the number of particles in it and then average the mean stretching to approximate the stretching value for this cell. Furthermore, the cell size we discretize here is small enough so that the flow properties (e.g. velocity) in each can be assumed to be constant. Therefore we can assume a homogeneous stretching in each cell as well.

In this study, 70,000 passive particles with arbitrary vectors are initially seeded into the flow domain at plane z=0.4mm. After several time periods, each vector on each particle has been stretched and the corresponding ratio of the length magnitude λ can be computed through eqns. (3.15-3.17). It is worthy to noticing that we can plot how much a point initially located in cell will stretch or how much a point currently located in a particular cell has stretched [18]. Here in this work, we present the stretching by showing λ as a function of initial location. In other words, here we only plot the stretching value after several periods on each particle on its initial position, no information of final position of each particle is shown. Once we obtain the average λ in each cell, the root mean square value of λ on the whole surface is also computed. Figure 3.33 below shows the temporal evolution of λ_{rms} with different T for the same 10 periods in a semi-log plot. As expected, when increasing the time period T, the root mean square of the stretching ratio increases exponentially.

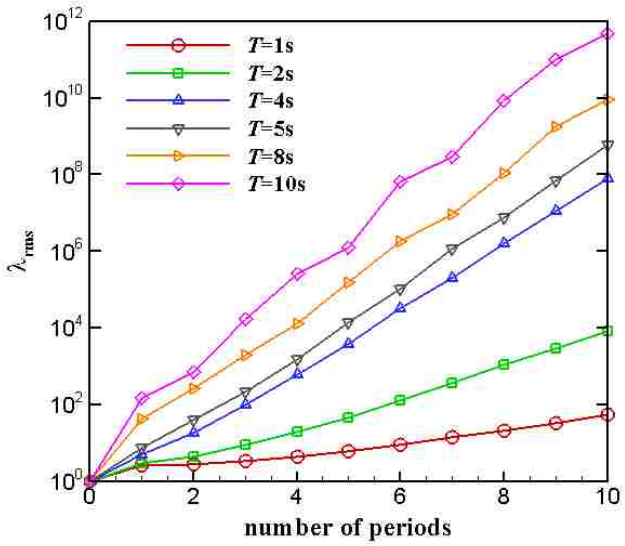

Figure 3.33. Temporal evolution of λ_{rms} with different time periods T for 10 periods.

Figure 3.34 shows the stretching plots along with their corresponding species concentration maps for T=1s, 4s, 8s and 10s. The results show that the stretching is highly non-uniformly distributed in the flow domain. From the comparisons, we find very good agreements between the stretching plots and species concentration maps even compared with the material line deformation figures in Figure 3.31. From these figures, one can find that for all four cases, most stretching occur in the middle of the flow domain, or let's say close to the disk electrodes. This is understandable because we have the largest velocity magnitude near the disk electrodes (please see Figure 3.25 (b)) for the velocity magnitude profile). As a result, we have the largest stretching around these areas and smallest stretching near the wall in contrary. From Figure 3.34 (a) for case T=1s at its 10^{th} period, along with the relevant root mean square stretching ratio value presented in Figure 3.33, we find that the stretching in this case is quite small, even the fluid elements around the disk electrodes have not been stretched and folded enough to start mixing. Even though we running this case for a longer time will not improve the stretching nor mixing since from Figure 3.33 we find that the slope of line T=1s is comparably flat, and the species concentration map in Figure 3.28 also demonstrates that. For case T=4s at its 10^{th} period in (b), the stretching extent has been improved and the

two species start to mix with each other from the central area. For cases T=8s and 10s at their 5^{th} periods in (c) and (d), the red colored areas in the stretching plots are increasing which indicates great stretching and folding there and two species are mixed very well in these areas which is well reflected in the corresponding species concentration maps. These results here well demonstrate that the first stage for a good mixing is to stretch the fluid elements sufficiently.

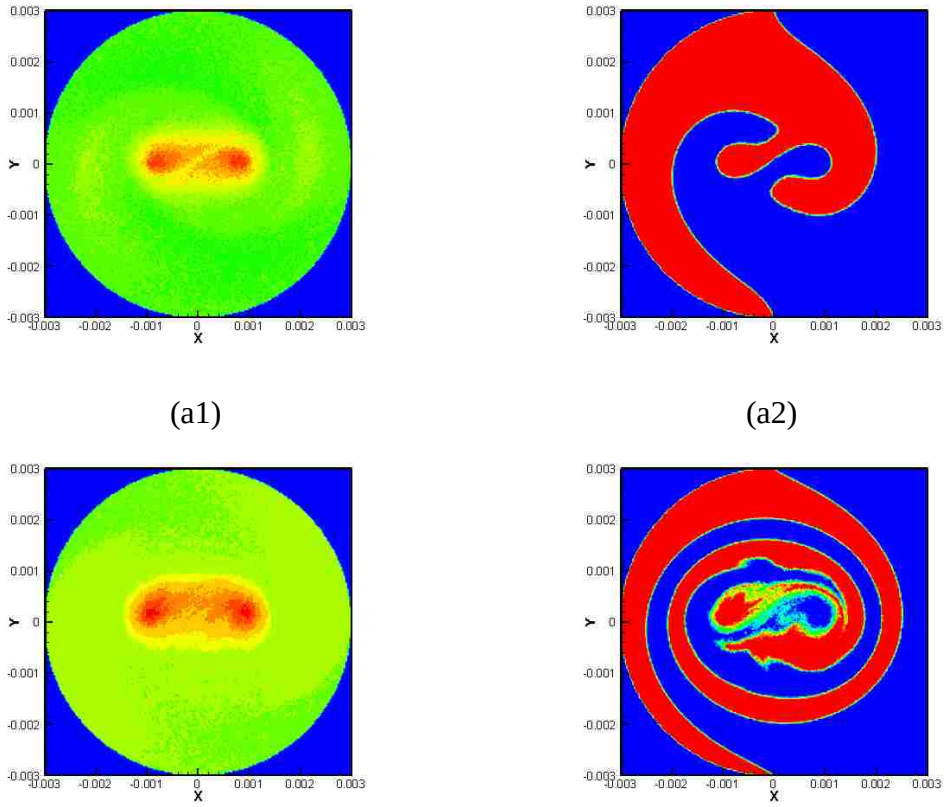

(a1) (a2)

(b1) (b2)

Figure 3.34. Stretching plots and the corresponding species concentration maps. (a): T=1s at t=10T, (b): T=4s at t=10T, (c): T=8s at t=5T and (d): T=10s at t=5T. To create the stretching maps, the stretching ratio value is calculated in each cell, and a cutoff value is chosen above which the stretching is considered large and any cell with stretching ratio value larger than this value is colored red. Obviously, for different cases, the cutoff values are chosen different.

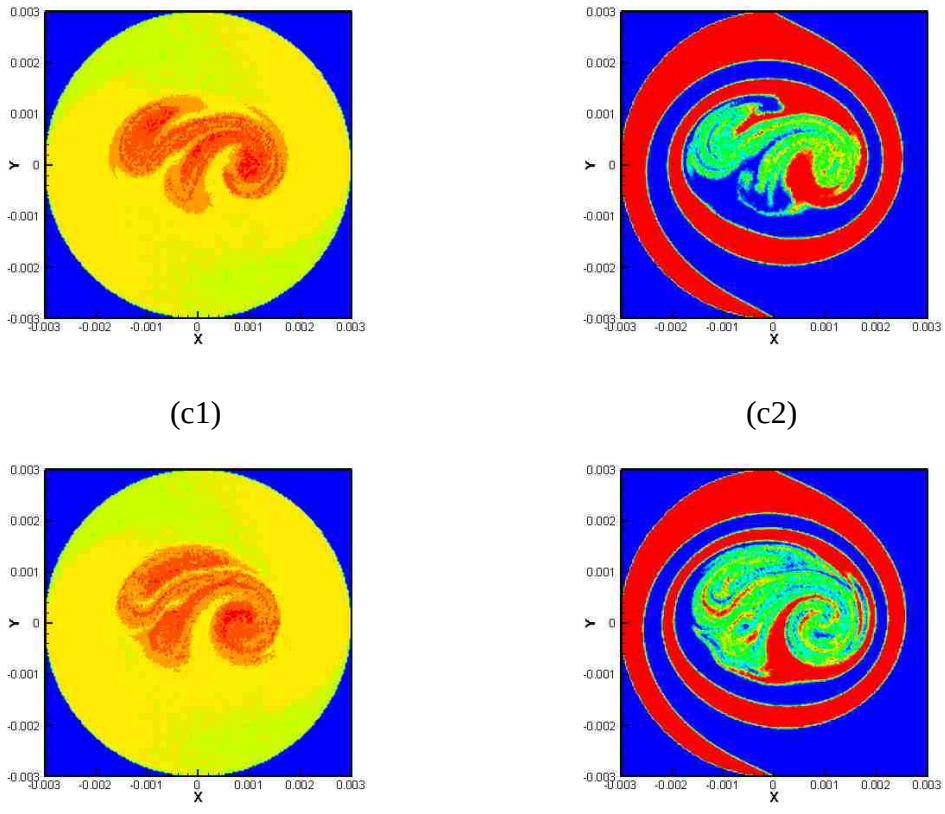

(c1) (c2)

(d1) (d2)

Figure 3.34. Stretching plots and the corresponding species concentration maps. (a): T=1s at t=10T, (b): T=4s at t=10T, (c): T=8s at t=5T and (d): T=10s at t=5T. To create the stretching maps, the stretching ratio value is calculated in each cell, and a cutoff value is chosen above which the stretching is considered large and any cell with stretching ratio value larger than this value is colored red. Obviously, for different cases, the cutoff values are chosen different (cont.).

3.2.3.7 More on chaotic advection under scheme 2. The numerical results show that the "blinking vortex" model can be achieved by using the electromagnetic force in a disk-ring microfluidic device. Similar results are found between our simulations and the experiments from Aref's and Bau's work. The alternatingly switching on and off scheme absolutely is a simple but efficient way to provide an unsteady quasi-two-dimensional Stokes flow which can create the chaotic motions. The time period T in this scheme is an important parameter to distinguish the regular and chaotic motions. For small T, the flow motion is regular which is reflected by its regular curves shown in the

corresponding Poincaré map. And the particle concentration map also reveals the poor mixing performance even after a long repeating time. Material lines stretching and deformation results show for small *T*, the material line is not able to spread throughout the whole domain and two material lines with different initial locations are not able to mix with each other neither. All these three numerical experiments demonstrate that small *T* brings out a regular flow motion and the outcome is a poor mixing performance. By increasing *T*, the motion becomes more chaotic, the particle markers in the corresponding Poincaré maps begin to scatter from inside to outside and spread to reach the whole domain. However, two islands occur for some specific *T*. Results show that no mixing is allowed in these islands though the general mixing performance is improved. Continuing to increase *T* gives an even better uniformly distributed Poincaré map, and more efficiently stretching can be obtained. As a result, a good mixing performance can be achieved.

As we mentioned, the "blinking vortex" model is a simple way to generate the chaotic motion. It is very reasonable to expect an even more chaotic motion along with the corresponding mixing performance by implementing more complicated alternating scheme [21-24]. Fortunately, this can be achieved easily in MHD micro devices since by judiciously selecting the positions of the electrodes and the alternatingly switching schemes, people can manipulate the flow as they want. Here the alternating scheme 2 (eqn. 3.10) is used to obtain more complicated secondary flows. Instead of just moving the "agitators" from left to right alternatively, now two counter-rotating flows are generated and they are successively repeated horizontally and vertically. The typical velocity vectors are shown in Figure 3.26. Figure 3.35 shows the Poincaré map, particle concentration map and the corresponding species concentration distribution at t=160s. From the particle concentration map and the species concentration contours, it is clear that we have an even better mixing performance than that in case T=10s of the "blinking vortex" model. And the mixing area now is enlarging to almost the whole domain while only a small region on the left up corner is mixed. From these facts, we can also find that this four disks and ring scheme have a better mixing performance than those results in the "blinking vortex" model. For the "blinking vortex" model, only two electrodes are involved, which indicates that the particles motions will be confined in a narrow ellipse.

Though Poincaré map shows that eventually, the particles can reach the whole domain in that case, it may cost an extremely long time for the system to achieve that status. However, in real life mixing, we want the good mixing to be achieved as fast as possible in the whole devices rather than only some regions inside the devices. Therefore, the four disks-ring scheme we have here absolutely has its own advantage due to its large mixing area within a short time. However, the choices for the number and locations of the electrodes, magnitude and orientation of the magnetic field intensity, type of electrolytes and the alternating scheme provide a large set of options to choose form. Narrowing down the selections from the vast array of the options would become an optimal problem for the specific LOAC application which will not be addressed in this work. The presented results here suggest that the even more complex flow structures and better mixing performances can be created by straight forward extensions of the technique used in this study. However, other aspects such as energy consumption, feasibility of fabrications and cost should be also taken into account when designing these kinds of micro stirrers.

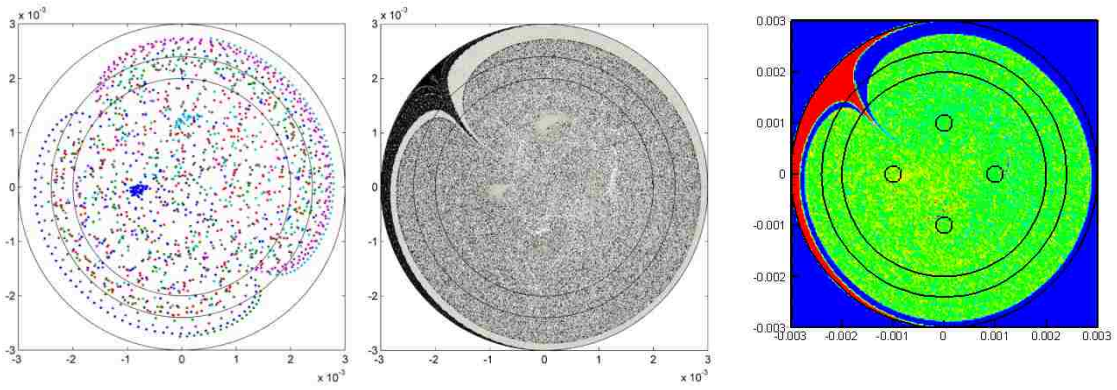

(a) (b) (c)

Figure 3.35. (a): Poincaré map, (b): particle concentration map, (c): species concentration contour at t=160s. Four disks, Scheme 2, T=4s.

3.2.3.8 Features revealed by 3D simulations of the Navier-Stokes Equations.

It'd be helpful to compare our results to Dufour et al [25] and highlight similarities and

differences. They also used a shallow cylindrical cavity, but of a larger radius (17.5 mm), and the electrodes were non-intrusively placed on the cavity floor. Based on the cavity and the electrode dimensions, their device can be classified as mm-scale. Their Reynolds number is of the same order (~1) as ours. Their time periods and mixing times are an order higher compared to ours. As to the model itself, they used the linearized Stokes flow model, whereas we used the full Navier-Stokes model. Their magnetic flux density is 0.05T whereas ours is 0.36T. There is also another major difference between the works of Dufour et al [25] and ours in the electric potential boundary conditions. They used an electrode potential of 0.4 V in their simulations, whereas we used 0.04V after accounting for the steep double layer drop. Considering that the conductivities are similar (~1 S/m), the total current should scale as electrode area under the same potential boundary conditions. The kinematic viscosity of their electrolyte solution is ~3.6 times that of ours. The maximum velocity in their work is larger by a factor of 10. They took into account the variation of the z-component of the magnetic flux density B_z with radius. Since the radius of the cavity in our case is only 3 mm, we used a constant value for the magnetic flux density component B_z. Isaac et al [8] have shown that including all the three components of the magnetic field when it is non-uniform and not pointing along the symmetry axis significantly affects the flow field.

Our results show that efficient mixing is possible in microscale devices with time periods of potential switching and elapsed time, a surrogate for a lab-on-a-chip response time, an order of magnitude less than reported by Dufour et al [25]. The main reason for the shortening of the mixing time is the choice of the number of disk electrodes, their placement and the switching schemes. As suggested by previous investigators, unsteady, three-dimensional flow fields lead to better mixing compared to unsteady two-dimensional flow fields, even though the latter is more amenable to visual interpretation and comparison to Hamiltonian systems. As in other optimization problems involving geometric parameters, optimizing system parameters for mixing in microfluidics is challenging due to the large number of parameters such as actuator eccentricity, number of actuators, and switching schemes. Nevertheless the present MHD-based mixing schemes are promising due to its simplicity and the ability to provide actuation without relying on mechanical stirring.

3.2.4. Conclusions. In this study, three-dimensional numerical simulations are conducted to investigate the mixing performance enhancement by chaotic advection by using MHD in a disk-ring microfluidic device. The externally applied potential and the magnetic flux density, 1V and 0.36T, respectively, are smaller compared to those in other works, and the maximum velocity is also correspondingly smaller (~0.5mm/s vs. 10mm/s), it is still possible for the described MHD microfluidic cell to achieve good mixing by creating chaotic advection. By switching on and off two disks (working electrodes), flow pattern similar to that in the "blinking vortex" model has been created. For small periods, the flow patterns are regular and the mixing performance is poor. By increasing the period, more chaotic motion can be generated, thus improving the stretching and deformation of material lines and enhancing mixing performance. By having two pairs of electrodes switched according to the prescribed scheme, more complex chaotic advection has been generated that led to enhanced mixing. The simple on/off switching scheme with two working electrodes is a simple but efficient way to provide an unsteady two-dimensional Stokes flow which can create chaotic motion. The time period T in this scheme is an important parameter that dictates whether the flow will be regular or chaotic. For small T, the motion is regular which is reflected by its regular curves shown in the corresponding Poincaré map. The particle concentration maps of the small T cases also reveal the poor mixing performance even after many switching cycles. By increasing T, the motion becomes more chaotic, and the particle markers in the corresponding Poincaré maps begin to scatter from inside to outside and spread to the whole domain. However, two islands form for some specific T values. Results show that little mixing occurs in these islands though the general mixing performance is improved. Continuing to increase T results in an even more uniformly distributed Poincaré map, and greater stretching of the material lines. As a result, mixing performance improves.

It is shown that greater chaotic motion along with the corresponding increase in mixing performance can be achieved by implementing more elaborate potential switching schemes and electrode placement. Instead of just cycling between the two disk electrode "agitators" with a given period, two counter-rotating flows are generated and the sequence is repeated by alternatively activating two disk electrode pairs. The four-disk

scheme we have presented has significant advantage due to the large mixing regions achieved within a short time.

The choices for the number and locations of the electrodes, magnitude and orientation of the magnetic flux density, type of electrolyte and the switching scheme, provide a large set of options to choose from. Narrowing down the selections from the vast array of options would become an optimal problem for the specific LOAC application which is not be addressed in this work. The results presented here suggest that even more complex flow structures leading to better mixing performances can be created by straight forward extensions of the technique used in this study. However, other aspects such as energy consumption, feasibility of fabrications and cost should be also taken into account when designing MHD micro stirrers. Though excellent works on MHD mixing by chaotic advection have been reported previously by other researchers, our present work brings additional insights facilitated by the power of CFD simulations, high resolution graphics and powerful post-processing of the simulation results. The present work lays out a promising approach to gain insight into the complex optimal problem of designing the LOAC device to optimize mixing and flow control.

4. MODELING AND SIMULATIONS OF CONDUCTING POLYMER MODIFIED ELECTRODE

4.1. OVERVIEW

This chapter presents the work on modeling conducting polymer modified electrode in microscale. Section two presents the transmission line circuit model we use to model the conducting polymer film. Section three presents CA, CV and CP responses from the model, and compares them with the existing experimental results. Section four and five give the results of MHD flow on rectangular and circular conducting polymer modified electrodes, respectively.

4.2. MATHEMATICAL MODELS

4.2.1. Overview. This section briefly describes the basic chemical reaction that occurs inside conducting polymer films and the transmission line circuit model. By applying an electrical potential, the polymer film can be switched between its conducting/oxidized state and neutral/reduced state with the faradaic current flowing in/out of the film [38]. Meanwhile, in the bulk solution, the ions from the supporting electrolyte moves into or out of the polymer film to maintain the electroneutrality inside the film. Eqn. (4.1) below represents in symbolic form the heterogeneous reaction inside the polymer film.

$$P^+X^- + e^- \Leftrightarrow P^0 + X^- \tag{4.1}$$

where P^+X^- and P^0 stand for the conducting/oxidized state and neutral/reduced state of the conducting polymer, respectively, e^- is the electron and X^- is the anion from supporting electrolyte. In the bulk solution, the electric current is due to the ionic current arising from the ions of the supporting electrolyte. Figure 4.1 below illustrates the reduction reaction of the conducting polymer film with NaCl as supporting electrolyte in the bulk solution. Therefore, the anion X^- in Eqn. (4.1) in symbolic form is Cl^-. More information regarding the electrochemical reaction of electroactive sites of the conducting polymer film can be found in literature [33].

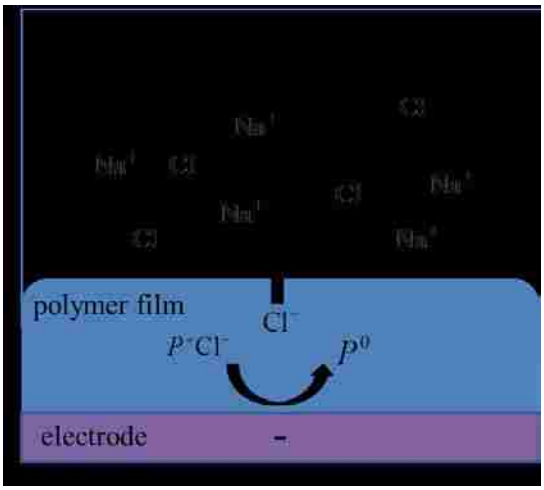

Figure 4.1. Reduction reaction of conducting polymer film with NaCl as supporting electrolyte [33].

4.2.2. Transmission Line Circuit Model of Rectangular Polymer Film. The full mathematical model of this system involves electron transfer at electrode/film interface, ions and electron transport inside the conducting film and ion transfer at film/electrolyte interface which is very complicated [40]. In this study, we rely on the transmission line circuit model to study the electrochemical behavior of conducting polymer [42]. In Shoa and Madden's work, they used capacitors and ionic resistance to equalize the ionic transport along the polymer thickness direction, and use the electronic resistance to achieve the potential drop along the polymer length direction. Also they assumed that the length is much longer than the width, therefore the potential drop across the width is negligible. By doing so, they derived 1D and 2D analytical expressions of total impedance of rectangular conducting polymer modified electrodes. The 1D and 2D analytical impedances in Laplace domain are shown below.

$$Z_{1-\mathrm{D}}(s) = \sqrt{R_i Z_c} \cdot \coth\left(\sqrt{\frac{R_i}{Z_c}} \cdot h\right)$$
$$Z_{2-\mathrm{D}}(s) = \sqrt{R_e Z_{1\text{-D}}} \cdot \coth\left(\sqrt{\frac{R_e}{Z_{1\text{-D}}}} \cdot L\right) \tag{4.2}$$

where $R_i = 1/(\sigma_i wL)$ is the ionic resistance per thickness, $Z_c = 1/(sC_v wL)$ is the impedance of the capacitor per thickness, $R_e = 1/(\sigma_e wh)$ is the electronic resistance per unit length and *w*, *L* and *h* are the width, length and thickness of the rectangular conducting polymer film. s is the Laplace variable and σ_i, σ_e and C_v are three parameters which represent the ionic conductivity, electronic conductivity and volumetric capacitance, respectively. Sketches of the 1D and 2D equivalent circuit are shown in Figure 4.2.

(a)

(b)

Figure 4.2. (a) 1D transmission line circuit, (b) 2D transmission line circuit for a rectangular polymer modified electrode. R_i and *C* represent ionic resistance and capacitance respectively.

Once the impedance from Eqn. (4.2) is obtained, the CA, CP and CV responses can be calculated by Inverse Laplace transformation. For example, under a potential step condition, if a potential difference $V(t) = V_0$ is applied, we first rewrite the potential difference in Laplace domain which is given by $V(s) = V_0 / s$, and then the current response in Laplace domain can be written as $i(s) = (V_0 / s) / Z_{1-D}(s)$ if we use 1D impedance. Finally, the time dependent current response can be obtained from inverse Laplace transform ($i(s)$ to $i(t)$). The Matlab code for the inverse Laplace transform can be found in Appendix. E. It should be mentioned that the potential step V_0 we apply to the polymer modified electrode is the potential difference between the electrode and the solution adjacent to it. Therefore, the electrical double layer effect is included in the transmission line circuit model and the potential difference in the bulk solution is neglected due to the presence of an excess of supporting electrolyte [45]. More information can be found in Shao and Madden's work [42].

4.2.3. Extension of Transmission Line Circuit Model to Circular Electrode. In Shao and Madden's work, the original transmission line model is only suitable for a rectangular polymer modified electrode. In this section, we extend the 2D transmission line circuit model to circular electrode. Similarly, we assume that the ionic transport takes place in the direction of polymer thickness while electronic transport occurs in the radial direction. Accordingly, we discretize the disk into one small disk in the center and several bands with different areas. Between each pair of bands, an imaginary resistance Re is connected to achieve potential drop in radial direction. The 2D equivalent circuit model for disk electrodes is presented in Figure 4.3.

According to the sketch in Figure 4.3, let's say we discretize the disk into one small disk in the center and four bands (n=5) which has the impedance of Z_j (j=1,2,…5) respectively. Where

$$Z_{1-D}(s) = \sqrt{R_i Z_c} \cdot \coth\left(\sqrt{\frac{R_i}{Z_c}} \cdot h\right) \tag{4.3}$$

However, for disk electrode, here R_i an Z_c are different for each band due to the difference of the area. The areas (j = 1) of the small disk and each band (j = 2, 3 , 4, 5) are

$$A_i(j) = \begin{cases} \pi r_j^{\,2}, & j = 1 \\ \pi(r_j^{\,2} - r_{j-1}^{\,2}), & j = 2,3\ldots5 \end{cases} \tag{4.4}$$

Figure 4.3. 2D transmission circuit model for a disk electrode.

Therefore,

$$R_i(j) = \frac{1}{\sigma_i A_i(j)}, \quad Z_c(j) = \frac{1}{sC_v A_i(j)} \tag{4.5}$$

The equivalent circuit in Figure 4.3 now can be treated as equivalent resistance of ladder that can be redrawn as Figure 4.4 below.

Figure 4.4. Equivalent ladder circuit.

Thus, the total equivalent impedance can be calculated numerically from Figure 4.4. Where, R_e is the electronic resistance along the radial direction which can be obtained,

$$R_e(j) = \frac{dr}{\sigma_e A_e(j)}, \quad A_e(j) = 2\pi r(j)\,\mathrm{h}, \quad j = 1, 2, \ldots 4 \tag{4.6}$$

4.2.4. Charging and Recharging of Conducting Polymer. Though a higher electric current can be achieved by using conducting polymer modified electrode because of the highly concentrated electroactive species inside the film, the trade-off is the short duration of electric current due to the limited amount of charge present in the polymer film at saturation limit, especially in microelectrodes. Therefore, it is very crucial to monitor and predict the charging process in order to avoid over-oxidization of the film.

Mathematically, the electric current is equal to the charge transfer rate

$$i = \frac{dQ}{dt} \tag{4.7}$$

where i is the total electric current in [A], t is the time and Q is the total charge in coulombs (c)present in the polymer film at time t . Once the electric current i is obtained from the transmission line circuit model, the charging/discharging time can be calculated from integrating Eqn. (4.7). The charging time thus obtained can be used to determine a cut-off criterion for charging which will avoid over-oxidation. In order to sustain the electric current for a longer time, one can flip the current direction after the cut-off time or cut-off potential is reached to recharge the film. A cyclic discharging-charging process can be used to sustain continuous operation. Other approaches such as increasing the thickness of the polymer film so as to increase the maximum charge level are also applicable. However, these approaches are beyond the scope of this dissertation and will be addressed in future work.

4.3. MODEL VALIDATION

4.3.1. Rectangular Electrode. In this section, CA (chronoamperometry), CP (chronopotentiometry) and CV (cyclic voltammetry) responses are obtained for a rectangular conducting polymer modified electrode to validate the transmission line circuit model to compare them to existing experimental results.

For validation, a long rectangular microband electrode is used. The length and width of the microband electrode are 25mm and 560μm, respectively. We select poly(3,4-ethylenedioxythiophene) (PEDOT) as the polymer material to compare our calculation with the experiment [33]. The computational parameters we use for the conducting polymer in transmission line circuit model are listed in Table 4.1. For different conducting polymers, the values of ionic conductivity, electronic conductivity and volumetric capacitance are different and they need to be determined carefully from experiments. Experimentally, the thickness of the polymer film is determined by the number of growth cycles or the deposition time during its preparation. The selection of the thickness h = 10μm in our simulations is based on experiments [44, 50]. Further, we assume that the bulk solution is filled only with water and NaCl supporting electrolyte. Since there is no redox pair in solution, no redox reaction takes place in the bulk solution.

Table 4.1. Computational data for rectangular polymer modified electrode

Ionic conductivity σ_i	0.022 S/m [50]
Electronic conductivity σ_e	8000 S/m
Volumetric capacitance C_v	8×10^8 F/m^3
Film thickness *h*	10 μm

Figure 4.5 below presents the CA (Fig. 4.5a), CV (Fig. 4.5b), CP (Fig. 4.5 c and d) responses of PEDOT modified electrode in 0.1M NaCl solution, respectively. From the CA responses in Figure 4.5a, we see that the electric current is initially high (~4 mA) and then quickly decreases to a very small value (~10μA at 5s). This behavior of the electric current is quite similar to the experimental CA response [33]. Figure 4.5b shows the typical CV response of a PEDOT modified electrode. The CV sweeps from -0.6V to 06V with a sweeping rate of 0.05V/s. The *i-E* curve from the CV has a rectangle-like shape which is the characteristics of double layer charging.

Figures 4.5c and 4.5d show the results of CP (chronopotentiometry) responses. Figure 4.5c is for case i=-25μA and Fig. 4.5d is for case i=-400μA. In the CP experiments [33], the potential increased approximately linearly with time, and a cut-off potential of 1.2V was set to prevent over-oxidation of the PEDOT film. The corresponding cut-off times are 75s for i=-25μA and 3.2s for i=-400μA. In our model, in order to predict how long the electric current (or MHD pumping) can be sustained before the film is completely oxidized, a cut-off time τ needs to be determined. By integrating the CA response in Figure 4.5a to a time long enough to be considered the time to reach oxidation limit, we can estimate the total charge of the conducting polymer film. From Fig. 4.5a, we choose this integration time as 20s and the corresponding charge *Q*=-1.49mC. Then, under constant charging, the cut-off time τ can be calculated by dividing the total charge by the applied current since the accumulated charge is proportional to the elapsed time under constant current charging. In our calculation, for i=-25μA and i=-400μA, the cut-off times thus calculated are τ =59.6s and 3.725s, respectively. Figures 4.5c and 4.5d show that the voltage vs. time plot is nearly linear. Therefore, a cut-off potential can be used to terminate charging to avoid over-oxidation. A cut-off potential

of ~1V correspond to the above cut off times, which is close to the cut off voltage of 1.2V used in the experiment [33].

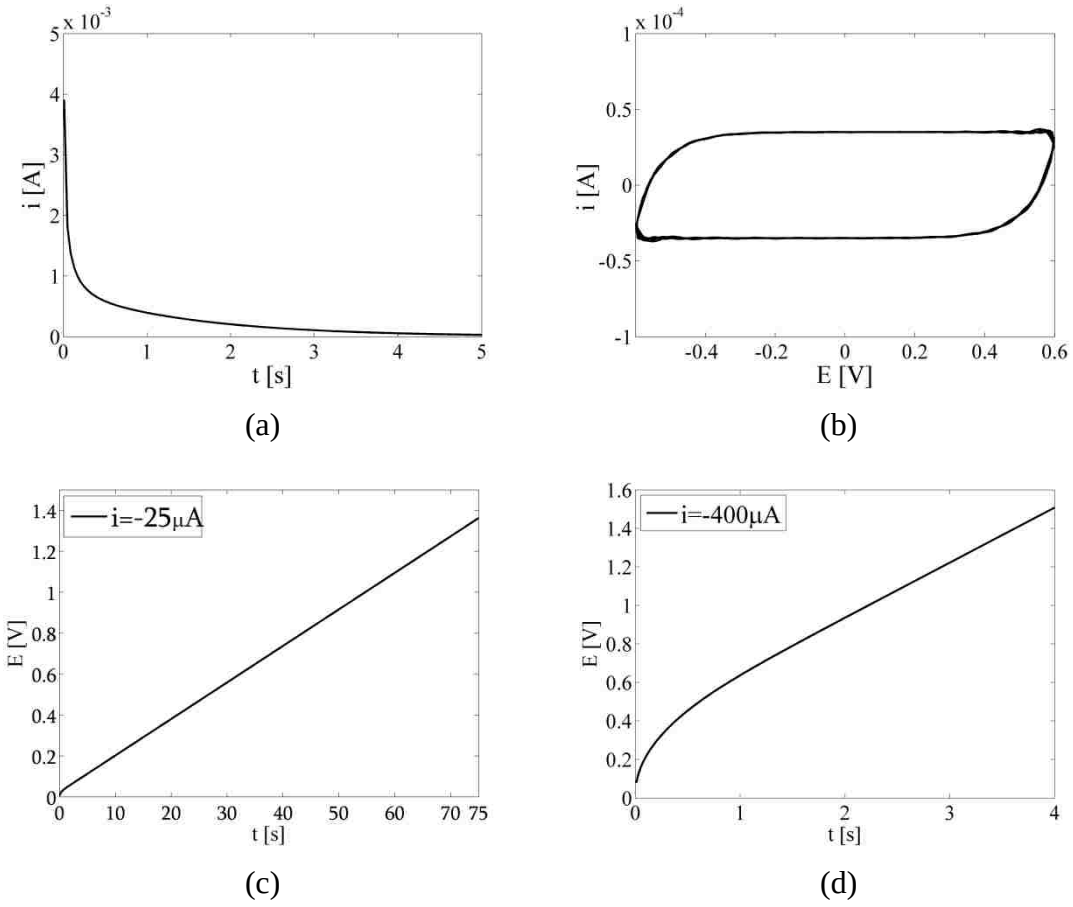

Figure 4.5. (a) CA response with V_0=1V; (b) CV response, from -0.6V to 0.6V with a sweeping rate ν=0.05V/s; (c) CP response with i=-25μA; and (d) CP response with i=-400μA.

4.3.2. Circular Electrode. In this subsection, we present the results of our extension of transmission line circuit model for the circular electrode and compare our results with other models and experimental data.

Bobacka's group conducted a series of experiments to study the electrochemical properties of PEDOT polymer film over a 3mm diameter disk electrode in different electrolytes and presented their equivalent circuit model [44]. Therefore, it is quite

convenient for us to use their experimental data to validate our model with their equivalent circuit model and experimental results. The equivalent circuit of Bobacka's group is shown in Figure 4.6.

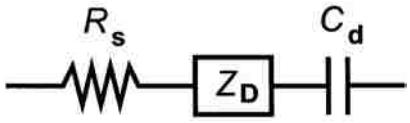

Figure 4.6. Equivalent circuit from Bobacka's group [44].

Where R_s, Z_D and C_d represent the solution resistance, Warburg diffusion element and capacitance respectively. The capacitance C_d is an additional electronic capacitance that was introduced to better represent experimental results. The total impedance of the equivalent circuit is

$$Z_{\text{total}} = \frac{1}{sC_d} + R_s + Z_D \tag{4.8}$$

where $Z_D = (\tau_D / C_D)\coth(jw\tau_D)^{1/2} / (jw\tau_D)^{1/2}$, s is the Laplace variable. The parameters used are listed below in Table 4.2. Once the total impedance Z_{total} is obtained, the i-E response can be calculated using inverse Laplace transformation.

Table 4.2. Parameters using in Bobacka's model [44]

[KCl]/M	R_s /Ω	τ_D /s	C_D /mF	R_D / Ω	C_d /μF
0.1	122	0.08	2.11	38	238

For the transmission line circuit model, we need to know the volumetric capacitance C_v, ionic conductivity σ_i, the film thickness and the electronic conductivity σ_e. Among them, the ionic conductivity σ_i can be found in the literature [50], σ_e is

dependent on different types of polymers which can be estimated, and the volumetric capacitance C_v can be calculated through Bobacka's experimental results. In Bobacka's experiment, the total capacitance consists of two parts, the Warburg capacitance C_D and the polymer bulk capacitance C_d, using which the volumetric total capacitance can be obtained,

$$C_v = (1/C_D + 1/C_d)^{-1} / (\pi r^2 h) \tag{4.9}$$

Then, the parameters we use for the transmission line circuit model are all obtained and are listed in Table 4.3.

Table 4.3. Parameters using in Transmission line circuit model for disk electrode

Ionic conductivity σ_i	0.022 S/m [50]
Volumetric capacitance C_v	3×10^7 F/m^3
Film thickness h	1 μm

CA and CV responses between the transmission line circuit model and Bobacka's model are presented below in Figure 4.7. The supporting electrolyte is 0.1M NaCl solution. Good agreements are found between two models. However, in Bobacka's model, the equivalent circuit is only suitable to their experimental data especially for specific electrode size and polymer thickness. The transmission line circuit model shows the advantage of modeling different shape and size of the polymer modified electrode.

4.4. MHD FLOW ON MICROBAND POLYMER MODIFIED ELECTRODES

4.4.1. Geometry. A shallow cuboid cell with two long rectangular electrodes deposited on the bottom which serves as working and auxiliary/quasi-reference electrodes respectively is used in this paper. The dimension of the cell is 40mm×12mm×0.75mm.

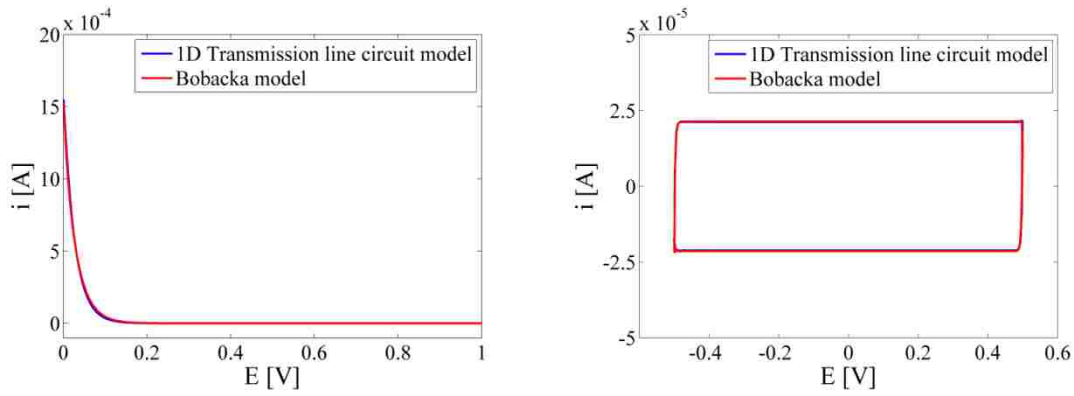

(a) (b)

Figure 4.7. (a) CA response, V_0=0.2V; (b) CV response, potential is sweeping from -0.5V to 0.5V with a sweeping rate of 0.1V/s.

The length and width of the microband electrode are 25mm and 560µm respectively. Figure 4.8 below shows the cell geometry. Magnetic flux density B which is in -z direction is also shown there. The two electrodes are placed symmetrically about *x* axis and the distance between them is 5.6mm.

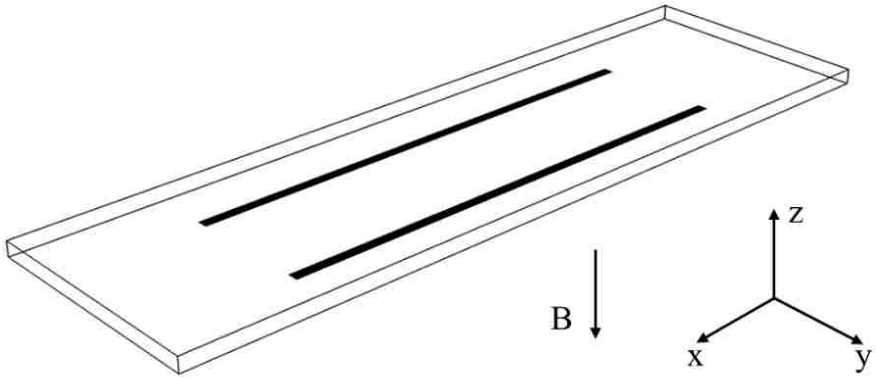

Figure 4.8. Cell geometry and magnetic flux density B.

4.4.2. Simulation Setup. Another advantage of using conducting polymer modified electrode in MHD pumping and mixing is that it simplifies the mathematical modeling of electric current in the bulk solution. Because the redox species are confined inside the polymer film, there is no redox reaction taking place in the bulk solution. Therefore, the electric current in the solution with supporting electrolyte can be modeled using Eqn. (2.2) which only takes the migration effect into account. In this work, the electrical conductivity σ is assumed to be constant everywhere in the bulk solution which contains 0.1M NaCl supporting electrolyte. The total electric current on the active electrode which is used to setup for the boundary conditions should be equalized to the value obtained from transmission line model for either controlled potential or controlled current method. That means, once we obtained the electric current response from the transmission line circuit model, this current is used as specific flux boundary conditions in CFD simulations and the electrical potential ϕ can be obtained by solving Laplace equation (Eqn. (2.4)) in the whole domain. Once the electrical potential ϕ is obtained, the electric current in the bulk solution can be calculated from Eqn. (2.2). In this paper, we find the electrical conductivity σ=1.264 S/m in solution with 0.1M NaCl supporting electrolyte. The density and dynamic viscosity of the bulk solution are 1000 kg/m^3 and 0.001 kg/m/s in our simulations.

4.4.2.1 Governing equations, initial and boundary conditions. The governing equations are the same as those in the previous chaotic mixing part which includes the Navier-Stokes with Lorentz force term (Eqn. (2.14)), and divergence free of velocity (Eqn. (2.13)). The electric current is modeled with Eqn. (2.2) without diffusion and convection terms which has been mentioned.

Two types of methods: controlled potential method and controlled current method are used in this study. Apparently, the corresponding boundary conditions are different from each other.

For controlled potential method which is corresponding to the CA (chronoamperometry) response, we first obtain the electric current response from the transmission line circuit model under the applied potential. And then, we can obtain the current flux on the active electrode. The current flux boundary condition is shown below,

$$\nabla\phi\big|_n = -\frac{i(t)}{\sigma A} \tag{4.10}$$

Where, ϕ is the electrical potential, $\bar{n}$ is the normal vector of the active electrode, $i(t)$ is the electric current response from the transmission line circuit model under the applied potential, σ is the electrical conductivity of the bulk solution, and A is the area of the active electrode. Since the electric current response is a time-dependent function (Figures 4.5 (a) and 4.6 (a)), the current flux boundary condition $\nabla\phi$ is also a time-dependent function. Therefore, a time-dependent UDF function is needed to achieve the boundary condition Eqn. (4.10).

For controlled current method which is corresponding to the CP (chronopotentiometry) response, we can directly use the constant applied current as our boundary condition,

$$\nabla\phi\big|_n = -\frac{i_0}{\sigma A} \tag{4.11}$$

here, i_0 is the applied current which is a constant value in controlled current case.

Zero current flux ($\nabla\phi = 0$) boundary condition is specified on all surfaces except the active electrodes. For the hydrodynamic boundary condition, the no-slip boundary condition is used at the walls. For the simulation of transient phenomena, we start with the fluid initially at rest, and therefore the velocity components everywhere in the solution are set to zero.

4.4.3. Results.

4.4.3.1 Controlled potential method. For controlled potential method, an electric potential of V_0=1V is applied between two PEDOT modified microband electrodes. Since both electrodes are polymer modified, the equivalent circuit model can be treated as two transmission line in series [42]. Therefore, the half cell impedance with a potential step of 0.5V and -0.5V at each electrode respectively is solved. Once the time dependent current density is obtained on both electrodes as CA response, the value is used as specific flux boundary conditions in Fluent as described in the previous section. The rest of boundaries are set to be insulating wall. Figure 4.9 below presents the electric equal-potential lines and ionic current flux in the middle horizontal plane of the cell and

Figure 4.10 presents the electric equal-potential lines and ionic current lines in the cross section plane at x=0. From the figures, we find the current flows from the upper electrode to the lower one, by coupling with the external magnetic flux density B which is in –z direction, Lorentz force and thus fluid flow that exerts and moves from left to right is expected as shown in Figure 4.11. In this case, two counter-rotating flow is generated and therefore the pumping function is accomplished in the region between two electrodes which is shown in Figure 4.11. It is worthy to noticing that by applying different voltages on different electrodes with specific positions, multipurpose flow control can be achieved in different microfluidic devices which are reported previously [27-32]. Figure 4.12 shows the electric current at electrode surface and the maximum velocity magnitude in the computational domain against time *t*. The electric current starts with a high initial value (~2 mA) and then decreases quickly over time. A maximum velocity (~550 μm/s) is achieved within 0.1s and then decreases to small value (~10μm/s) just like the current behaves. This phenomenon indicates that controlled potential method can provide a rapid but short term pumping. In experiment [33], a maximum speed (~590 μm/s) is achieved in 0.167s which also validates our model.

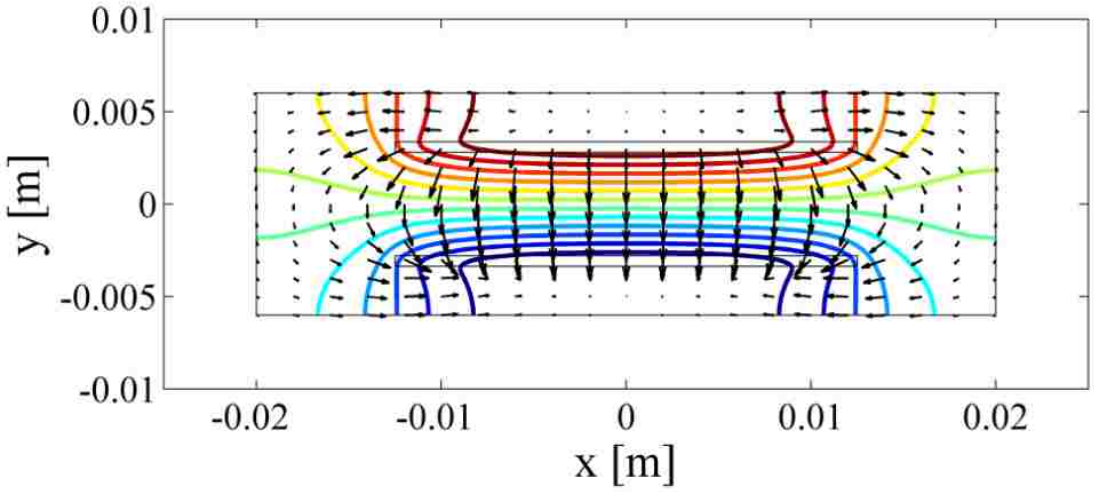

Figure 4.9. Electric equal-potential lines (color coded) and ionic current flux (black vectors) at middle horizontal plane for controlled potential method with V_0=1V.

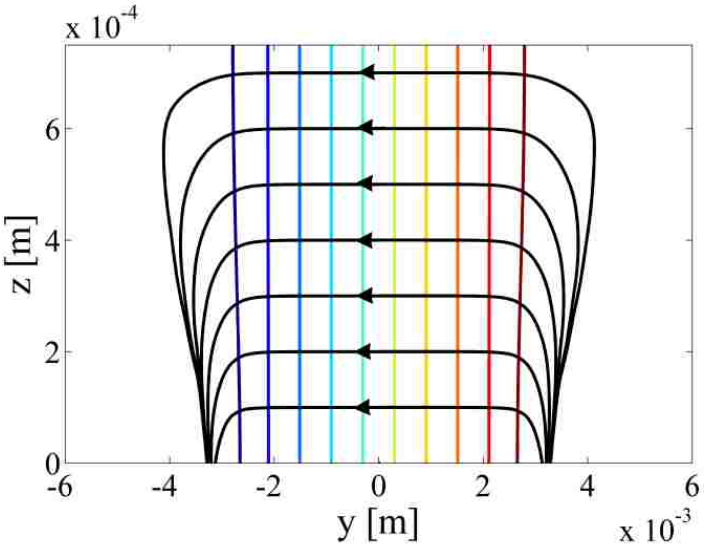

Figure 4.10. Electric equal-potential line (color coded) and ionic current lines (black lines) at cross section plane x=0. The z direction is exaggerated to get a better view.

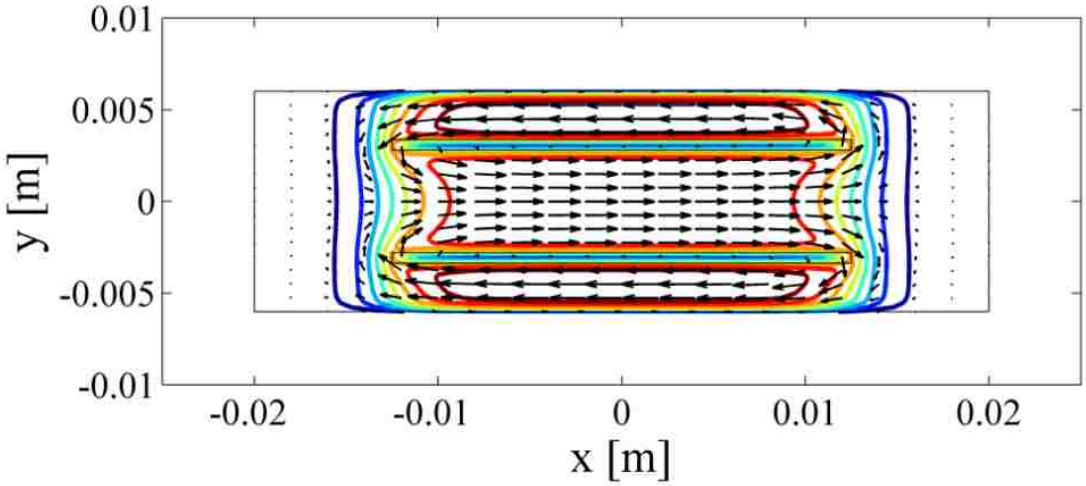

Figure 4.11. Velocity vector at middle horizontal plane for controlled potential method with V_0=1V. Velocity magnitude contours are color coded and velocity vectors are in black.

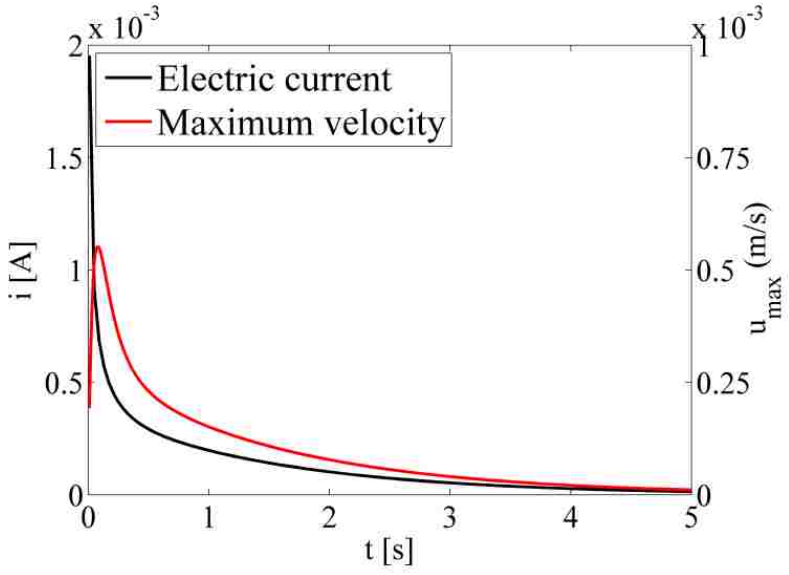

Figure 4.12. Time evolution of electric current and maximum velocity magnitude for controlled potential method with V_0=1V.

4.4.3.2 Controlled current method. For controlled current method, a constant current, for example i=-50μA is connecting between two PEDOT modified microband electrodes. The electric current is then directly used for the specific flux boundary conditions at the electrode surface and zero flux for other insulating walls. The flow velocity increases at the beginning from zero and then immediately reaches a steady value at 36.7 μm/s for i=-50μA. Though steady fluid speed is less than the maximum fluid speed in controlled potential method, a longer pumping duration is allowed in controlled current method as long as a cut-off potential/or cut-off time τ is set to prevent from film over-oxidization. Figure 4.13 shows the steady velocity magnitude and cut-off time τ for different applied current. It is clear that the flow velocity is linearly proportional to the applied current in MHD systems. Therefore, in order to accomplish a strong pumping, larger applied current is favorable. However, by increasing the applied current, the charge of conducting polymer film is consumed more quickly which eventually causes a shorter pumping duration. Therefore the dilemma of the pumping speed and duration should be considered carefully in different applications. However, controlled current method is still superior to the controlled potential method because the

steady fluid speed and controllable pumping time. Figure 4.14 shows the velocity profile along z direction and y direction under controlled current method.

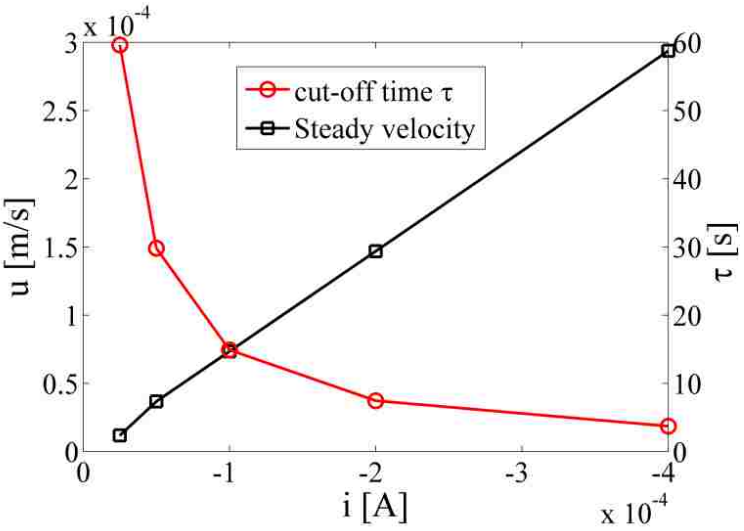

Figure 4.13. Steady flow velocity and cut-off time τ versus applied current.

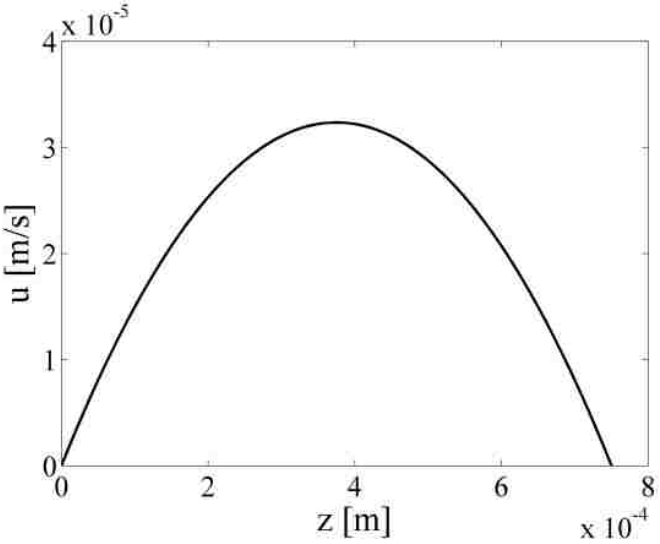

(a)

Figure 4.14. Velocity profile along z direction and y direction under controlled current method, *i*=-50μA at *t*=1s.

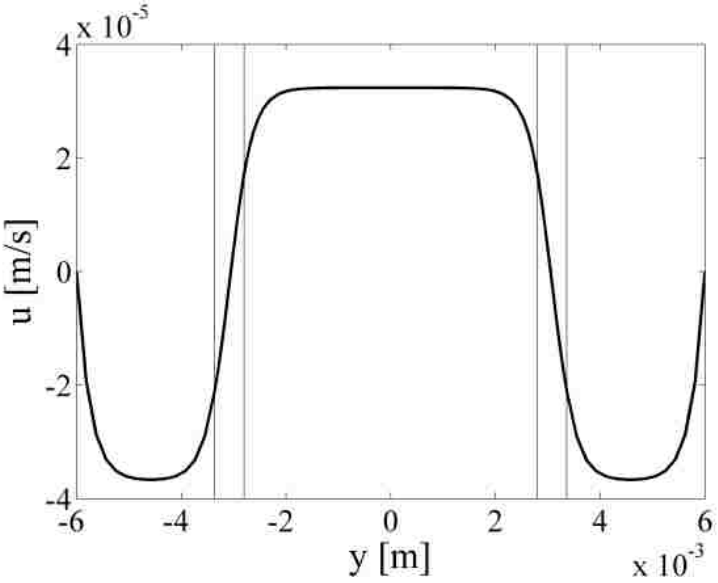

(b)

Figure 4.14. Velocity profile along z direction and y direction under controlled current method, *i*=-50μA at *t*=1s (cont.).

4.5. MHD FLOW ON DISK AND RING POLYMER MODIFIED ELECTRODE

4.5.1. Overview. In this section, parametric studies of MHD flow on disk and ring polymer modified electrodes are conducted. In order to shorten the computational cost, two dimensional asymmetric swirl model is used instead of the full three dimensional geometry with good agreements between these two. The parametric studies include four kinds of geometries: (1) Disk/ring, (2) Ring/ring, (3) Disk/ring/ring and (4) Ring/ring/ring for different flow manipulation purposes. And for the first disk/ring case, different parameters are studied as follows,

(a) Doubling the current for a fixed geometry, cell dimensions and B,

(b) Doubling |B| for a fixed geometry, cell dimensions and current,

(c) Doubling cell height and doubling the current,

(d) Doubling electrode dimensions, cell dimensions, and current for a fixed magnetic field,

(e) Doubling the width of ring electrodes and radius of the disk electrode while maintaining the same gap width for a fixed current,

(f) Doubling the gap between electrodes for a fixed current.

4.5.2. Geometry Configurations. The geometry presented here is a disk/ring configuration, where the radius of the disk is 800μm, width of the ring is 400μm and with a height of 620μm. The three dimensional configuration and the corresponding 2D axisymmetric swirl model are shown below in Figure 4.15. In Figure 4.15 (a), the red and blue parts are disk (working electrode) and ring (counter electrode), and the green one is the corresponding computational domain in 2d axisymmetric swirl model. Figure 4.15 (b) depicts the schematic view of the 2d axisymmetric swirl model geometry, where the computational domain rotates along the *x* axis.

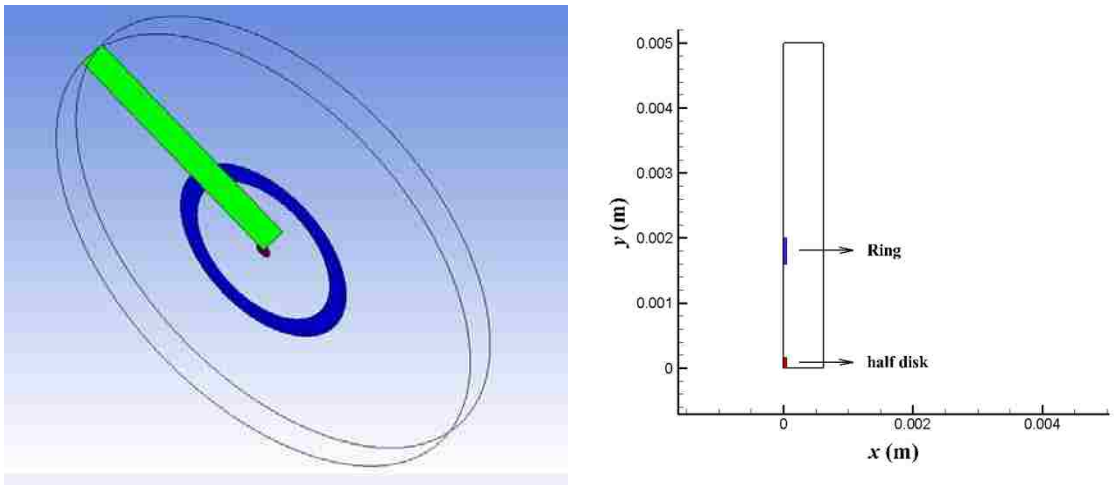

(a) (b)

Figure 4.15. 3D geometry of disk/ring configuration, disk (red), blue (ring) and green (corresponding 2D axisymmetric swirl geometry); (b): The corresponding schematic view of two dimensional axisymmetric swirl model.

The electrolyte we use in this series of simulations is 0.1 M NaCl solution, which has an electric conductivity of σ=1.264 s/m. A total applied current of 5μA is applied on the working electrode/disk and a zero potential boundary condition is applied on the ring. As a result, the current flux should be flowing from the ring to disk. The magnetic field is applied in –*x* direction, which has an intensity of 0.37 T. In this case, the Lorentz force

should induce a clockwise flow motion, and in 2d axisymmetric swirl model the flow direction should flow out of the domain. In order to study the other three configurations, we prescribe that the width of the ring and the gap are both 400μm and the radius of the disk is 800 μm. Figure 4.16 shows the corresponding 2D axisymmetric swirl model for each configuration. All the conditions and parameters are set as the same as those in the previous section.

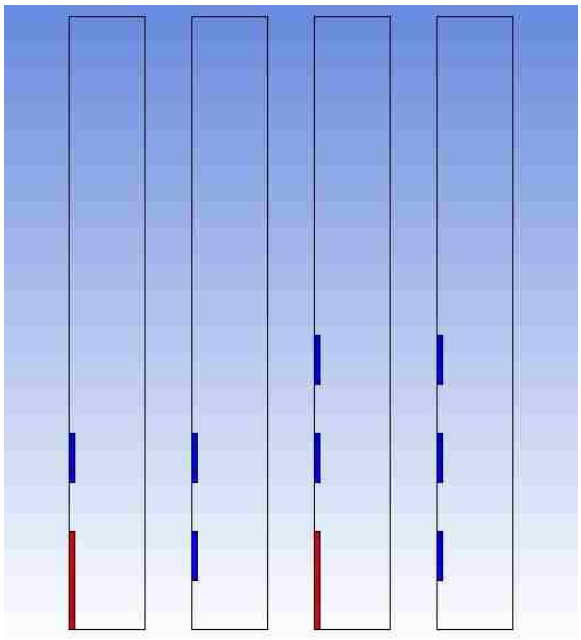

(a) (b) (c) (d)

Figure 4.16. 2D axisymmetric swirl configurations for each case. (a) Disk/ring, (b) Ring/ring, (c) Disk/ring/ring and (d) Ring/ring/ring. Red area: disk, blue area: ring.

4.5.3. Simulation Setup. In this part, controlled current method is used to study the MHD induced flow in these disk/ring electrode cases. Therefore, the constant specific current flux (Eqn. (4.11)) is used as boundary conditions at active electrodes and all surfaces except the electrodes are kept as zero current flux ($\nabla\phi = 0$). The governing equations are the same as those in the previous sections as well.

4.5.4. Results. In this part, controlled current method is used to study the MHD induced flow in these disk/ring electrode cases. Therefore, the constant specific current flux (Eqn. (4.11)) is used as boundary conditions at active electrodes and all surfaces except the electrodes are kept as zero current flux ($\nabla\phi = 0$). The governing equations are the same as those in the previous sections as well.

4.5.4.1 Disk/ring configuration. This part presents the results in disk/ring configuration. The radius of the disk is 800μm and the gap between the disk and ring is 400μm. A total current of 5μA is imposed on the disk (working electrode), as a result the current flux should be from the ring to the disk and cause a clockwise motion. Simulation result shows that the flow speed initially increases and finally achieves to a steady state, and the maximum velocity is about 19.8μm/s.

Figure 4.17 presents the electrical potential contours, and ionic current flux distribution. Figure 4.18 shows the ionic current density profile and Lorentz force density profile at x=0.1mm above the baseline at t=2s. The figures show that there is a tiny current flux with an opposite direction exterior to the main path outside the ring.

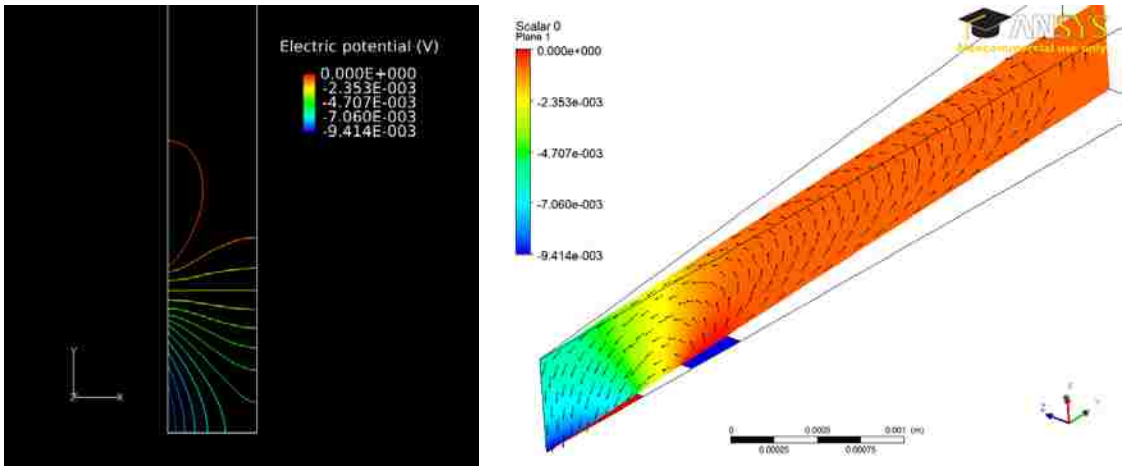

(a) (b)

Figure 4.17. (a) Electric potential contours; and (b) ionic current flux distributions. Disk/ring model.

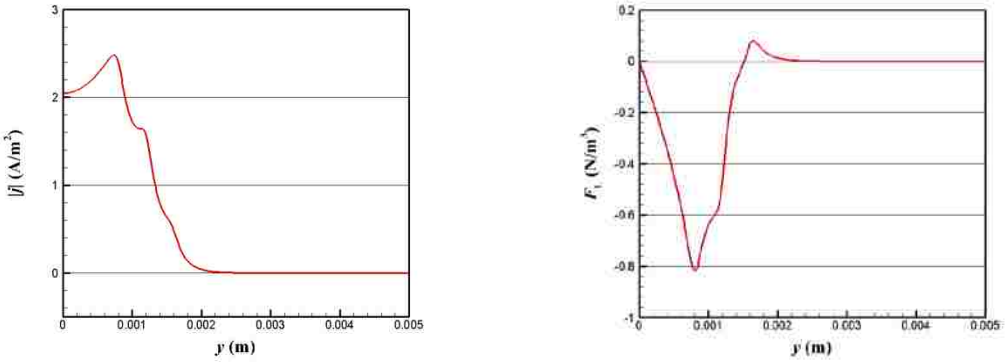

(a) (b)

Figure 4.18. (a) Ionic current density profile, and (b) Lorentz force density profile at x=0.1 mm at *t*=2s. Disk/ring model, i=5μA.

The Lorentz force profile in Figure 4.18 (b) also demonstrates that because the tiny current generates a small Lorentz force which has an opposite direction against the main Lorentz force. This tiny current flux initially will lead to a reversed flow against the main flow motion at the outer edge of the ring. However it disappears finally due to the viscous effect. Figure 4.19 which shows the tangential velocity profile at *x*=0.1mm at *t*=0.02s and 2s proves that behavior.

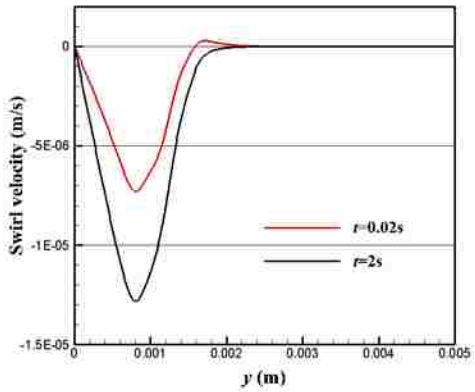

Figure 4.19. Tangential velocity profile at x=0.1 mm at *t*=0.02s (red) and *t*=2s (black). Disk/ring case, i=5μA.

4.5.4.1.1 Doubling the current for a fixed geometry, cell dimension and |B|.

In this subsection, the applied current is doubled to 10μA and other parameters are remaining the same. Simulation shows that the maximum velocity now is 39.6μm/s is also doubled. Figure 4.20 below shows the maximum velocity evolution over time, velocity magnitude, current density and Lorentz force density at x=0.1mm at t=2s. From the figures, we can see that by doubling the applied current, the current density is doubled, so is the Lorentz force. And as a result, the velocity magnitude is doubled, which is in commonly agreement in MHD flow.

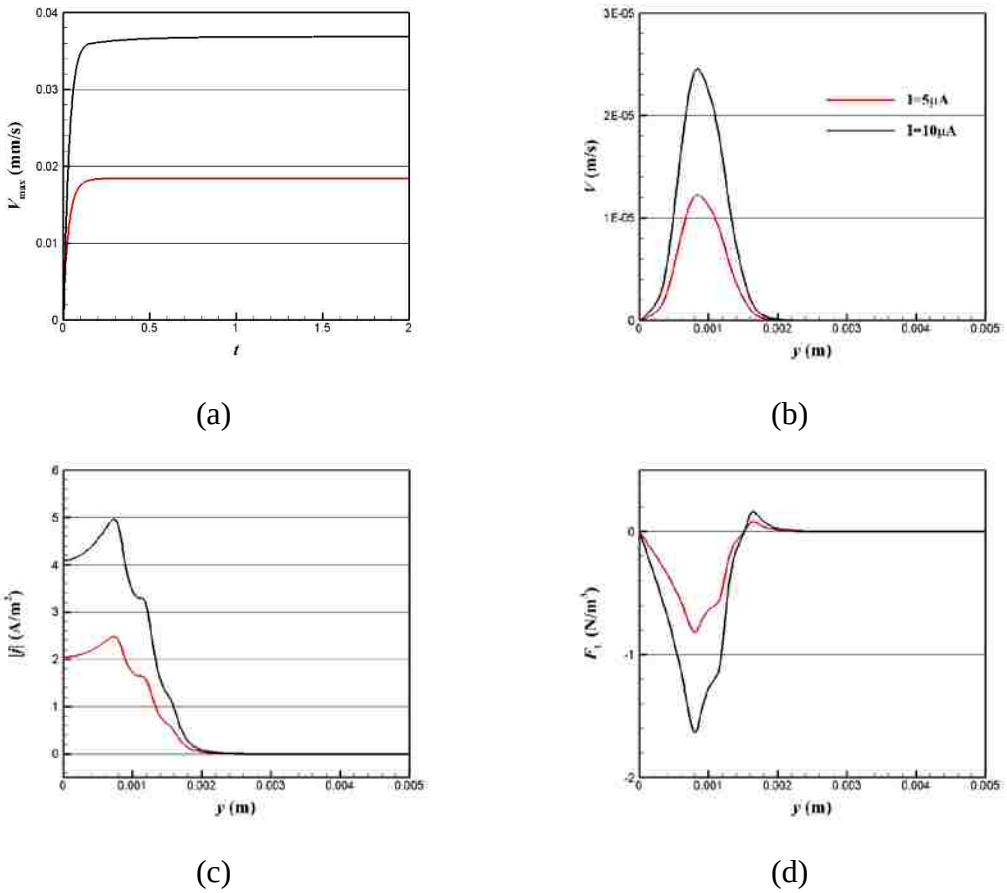

Figure 4.20. (a) Maximum velocity evolution over time, (b) velocity magnitude at x=0.1mm at t=2s, (c) ionic current density at x=0.1mm at t=2s, and (d) Lorentz force density at x=0.1mm at t=2s. Red line: original case, and black line: doubling applied current.

4.5.4.1.2 <u>Doubling |B| for a fixed geometry, cell dimension and applied current</u>. In this subsection, the magnetic flux density |B| is doubled. Due to the fact that the Lorentz force is proportional to the magnetic flux density B, the Lorentz force density and the velocity magnitude should be doubled as well, however the current density should remain the same. Figure 4.21 below shows the maximum velocity evolution over time, velocity magnitude, current density and Lorentz force density at x=0.1mm at t=2s. From the figures, we can find that the Lorentz force is doubled, but the current density remains the same. As a result, the velocity is doubled as well.

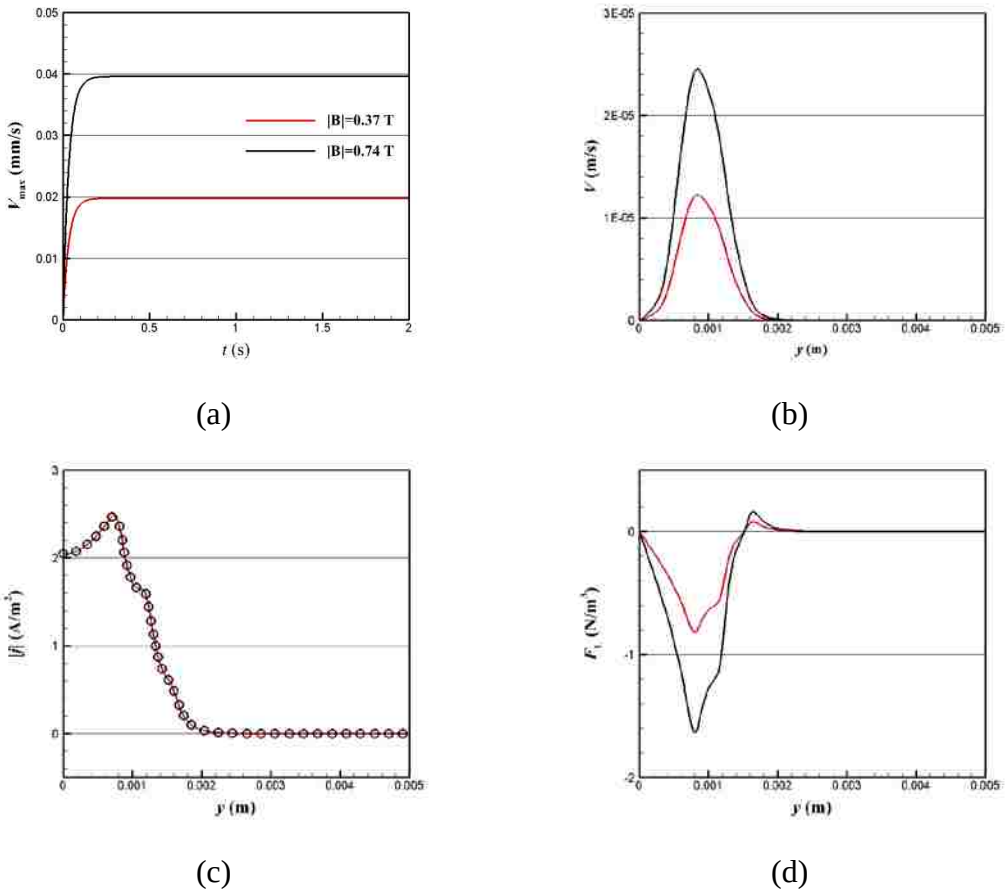

Figure 4.21. (a) maximum velocity evolution over time, (b) velocity magnitude at x=0.1mm at t=2s, (c) ionic current density at x=0.1mm at t=2s, and (d) Lorentz force density at x=0.1mm at t=2s. Red line: original case, and black line or circle: doubling magnetic flux density |B|.

4.5.4.1.3 <u>Doubling cell height and doubling the current</u>. In this subsection, the cell height and the applied current are doubled. Now, the cell height is set to be 1240μm and input current is 10μA. The maximum velocity in this case now is 50.7μm/s which is higher than that when just doubling the current. The net ionic current density across the gap cross section is, initial case: 1.284 A/m^2 and this case 1.289 A/m^2.

Figure 4.22 below presents the maximum velocity evolution over time, velocity magnitude, current density and Lorentz force density at x=0.1mm at t=2s. From these results, we can find that the maximum velocity is higher than that when just doubling the applied current. It is clear that, when doubling the applied current, the current density is doubled. However, in this case, the cell height is doubled as well, which means that the current density decreases by a factor of 2. Therefore, in fact, the current density should be the same as that in the original case. However, Lorentz force is a body force. Although the current density is same, so is the Lorentz force density, the magnitude of Lorentz force is increased by the lager cell volume. This finally increases the MHD flow speed.

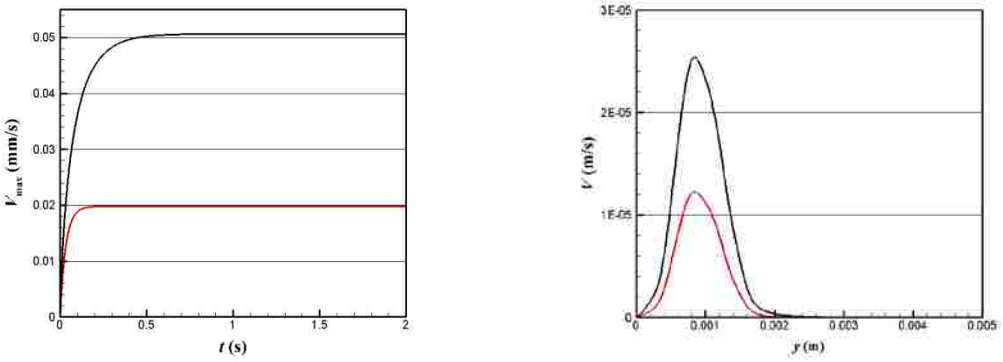

(a) (b)

Figure 4.22. (a) Maximum velocity evolution over time, (b) velocity magnitude at x=0.1mm at t=2s, (c) ionic current density at x=0.1mm at t=2s, and (d) Lorentz force density at x=0.1mm at t=2s. Red line: original case, and black line: doubling cell height and applied current.

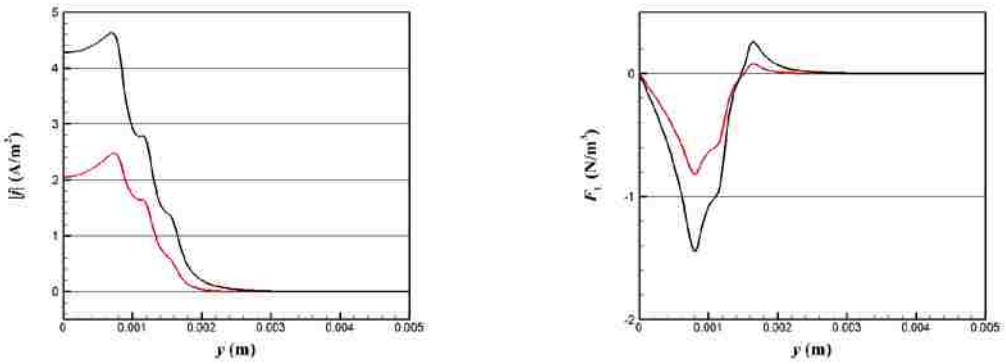

(c) (d)

Figure 4.22. (a) Maximum velocity evolution over time, (b) velocity magnitude at x=0.1mm at t=2s, (c) ionic current density at x=0.1mm at t=2s, and (d) Lorentz force density at x=0.1mm at t=2s. Red line: original case, and black line: doubling cell height and applied current (cont.).

4.5.4.1.4 <u>Doubling cell dimension and applied current</u>. In this case, the cell size and applied current are doubled. The maximum velocity can be reached to 39.6μm/s. Figure 4.23 shows the maximum velocity evolution over time, velocity magnitude, current density and Lorentz force density at x=0.1mm at t=2s. Since Lorentz force is a body force, therefore, by increasing the cell dimension, the magnitude of the Lorentz force increases. As a result, the maximum velocity increases.

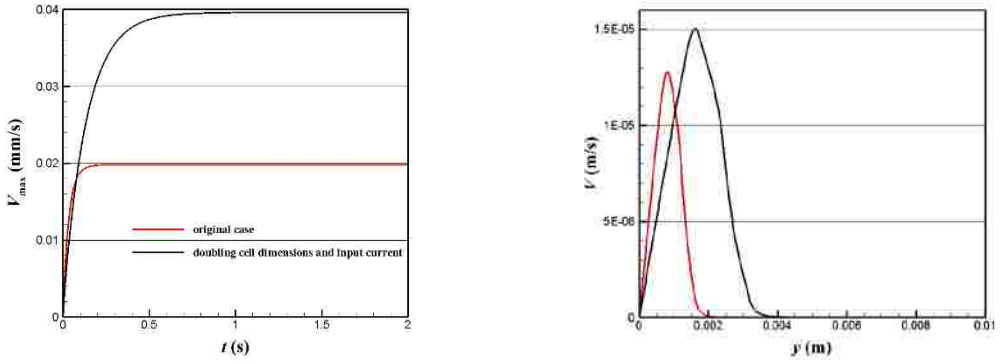

(a) (b)

Figure 4.23. (a) maximum velocity evolution over time, (b) velocity magnitude at x=0.1mm at t=2s, (c) ionic current density at x=0.1mm at t=2s, and (d) Lorentz force density at x=0.1mm at t=2s. Red line: original case, and black line: doubling cell size and applied current.

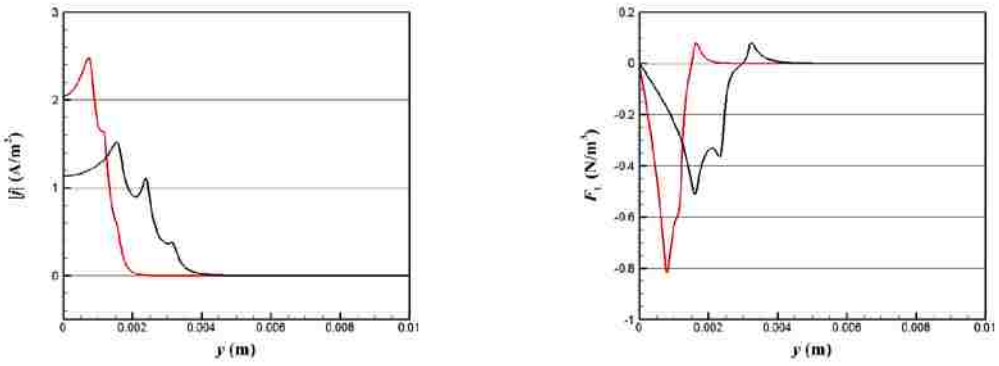

(c) (d)

Figure 4.23. (a) maximum velocity evolution over time, (b) velocity magnitude at x=0.1mm at t=2s, (c) ionic current density at x=0.1mm at t=2s, and (d) Lorentz force density at x=0.1mm at t=2s. Red line: original case, and black line: doubling cell size and applied current (cont.).

4.5.4.1.5 <u>Doubling the width of ring electrode while maintaining the width of gap.</u> In this case, the width of ring electrode is doubled. The maximum velocity for this case is 11.8μm/s. Because of the large electrode area, the ionic current density decreases near the electrode, so does the Lorentz force magnitude. As a result, the velocity decreases. Figure 4.24 blow presents the maximum velocity evolution over time, velocity magnitude, current density and Lorentz force density at x=0.1mm at t=2s.

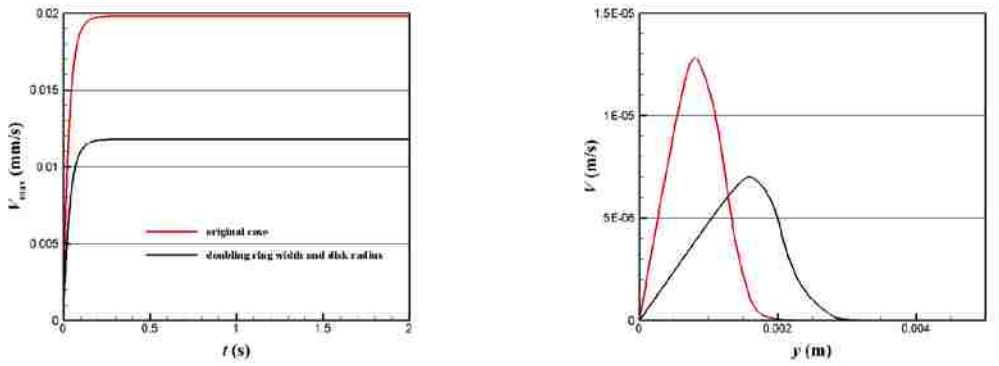

(a) (b)

Figure 4.24. (a) maximum velocity evolution over time, (b) velocity magnitude at x=0.1mm at t=2s, (c) ionic current density at x=0.1mm at t=2s, and (d) Lorentz force density at x=0.1mm at t=2s. Red line: original case, and black line: doubling width of ring.

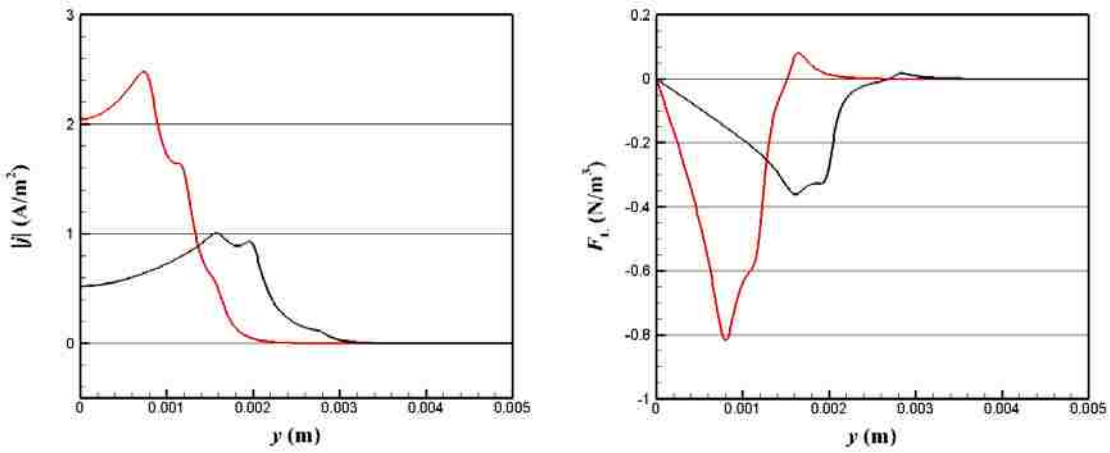

(c) (d)

Figure 4.24. (a) maximum velocity evolution over time, (b) velocity magnitude at x=0.1mm at t=2s, (c) ionic current density at x=0.1mm at t=2s, and (d) Lorentz force density at x=0.1mm at t=2s. Red line: original case, and black line: doubling width of ring (cont.).

4.5.4.1.6 <u>Doubling the gap between the electrode</u>. In this case, the gap between the disk and ring is doubled to 800μm. Result shows that the maximum velocity is very close to that in the original case. Figure 4.25 presents the maximum velocity evolution over time, velocity magnitude, current density and Lorentz force density at x=0.1mm at t=2s. From the result, we can find that the width of the gap does not influence the current density, Lorentz force very much. And as a result, the flow speed does not change much.

4.5.4.2 Ring/ring geometry. The model configuration is shown in Figure 4.16 (b). The width of the two rings and the gap between them are all 400μm. An applied current of 5μA is applied on the inner ring which is served as the working electrode. The maximum velocity can be reached to 18.4 μm/s.

Figure 4.26 shows the electrical potential contours, the ionic current flux distributions, Lorentz force density at x=0.1mm at t=2s and tangential velocity magnitude at x=0.1mm at t=0.02s and 2s. The results show that the ionic flux flows from the outer ring to the inner ring which generates a clockwise motion between two rings. It also shows there are two tiny ionic current fluxes inside the inner ring and outside the outer

ring in Figure 4.26 (b) which generates two counter-clockwise flow motion against the flow in the gap (see Lorentz force density in (c)). Figure 4.26 (d) shows the tangential velocity profile at x=0.1mm at t=0.02s and 2s. Though the two small current fluxes can generate two flows against the main flow motion initially, however the viscous effect can smooth them gradually. Finally, this ring/ring configuration can generate an overall clockwise motion which is similar to that in disk/ring configuration.

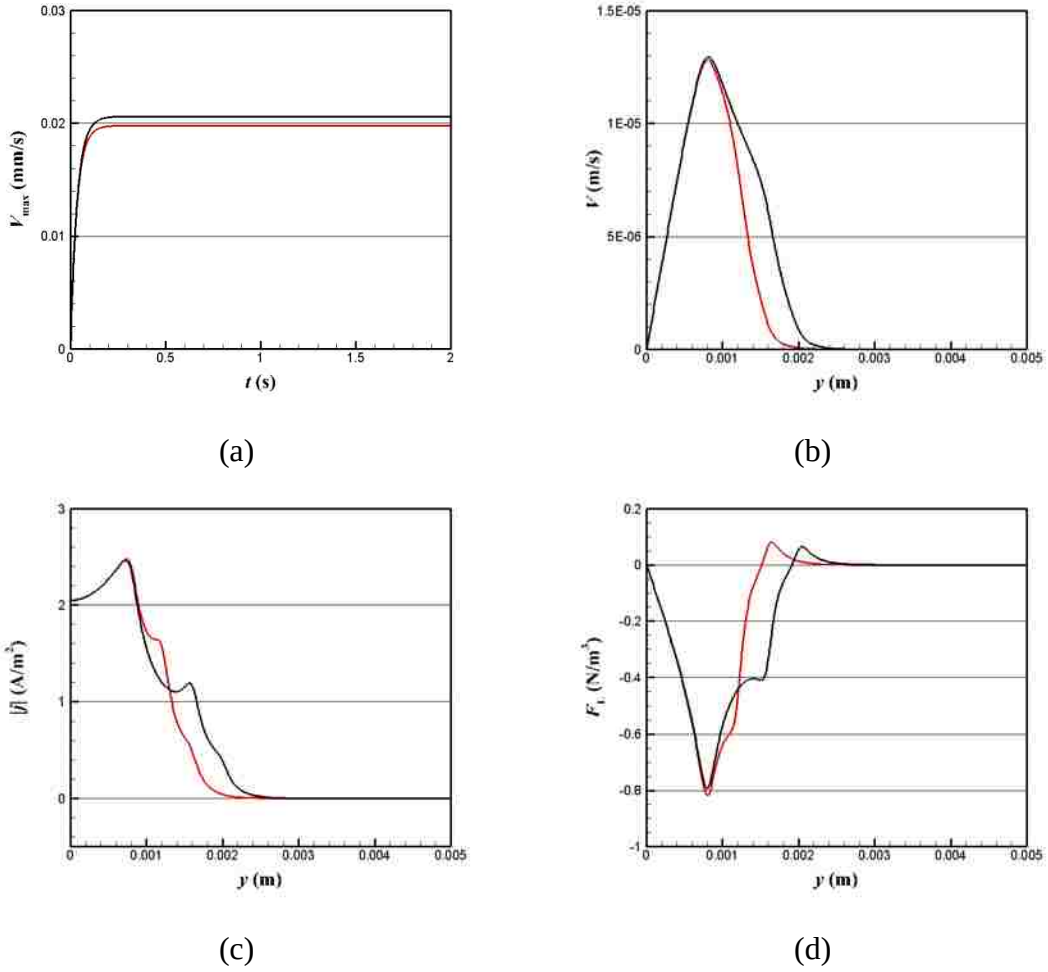

Figure 4.25. (a) maximum velocity evolution over time, (b) velocity magnitude at x=0.1mm at t=2s, (c) ionic current density at x=0.1mm at t=2s, and (d) Lorentz force density at x=0.1mm at t=2s. Red line: original case, and black line: doubling width of ring.

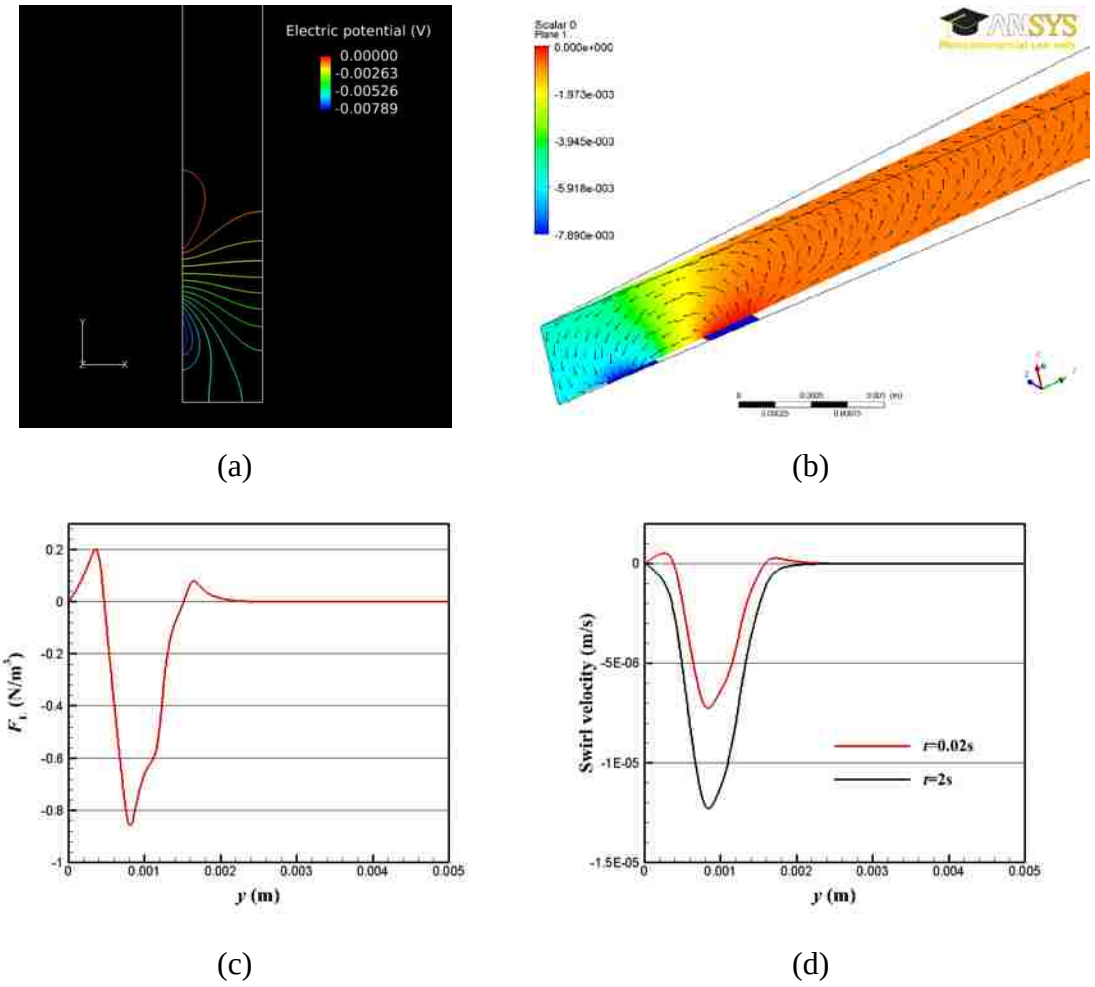

Figure 4.26. (a) Electrical potential contours, (b) ionic current flux distribution. (c) Lorentz force density profile at x=0.1mm at *t*=2s, and (d) Tangential velocity profile at *x*=0.1mm at *t*=0.02s (red) and *t*=2s (black). Ring/ring model.

4.5.4.3 Disk/ring/ring geometry. The model configuration is shown in Figure 4.16 (c). The width of the two rings and the gap between them are 400µm while the radius of disk is 800µm. A current of 5µA is applied on disk and outer ring which are served as the working electrodes. The maximum velocity of this case can be reached to 19.3µm/s.

Figure 4.27 shows the electrical potential contours, the ionic current flux distributions, Lorentz force density at *x*=0.1mm at *t*=2s and tangential velocity magnitude at *x*=0.1mm at *t*=0.02s and 2s. Figure 4.27 (b) shows there is a tiny ionic current flux

outside the outer ring as well. Figure 4.27 (d) shows the tangential velocity profile at x=0.1mm at t=0.02s and 2s. From these results we can find that the disk/ring/ring can control fluid flowing in opposite directions. And the velocity magnitude in the inner gap is large than that in the outer gap because the current flux density and Lorentz force in the inner gap is larger due to the smaller electrode area of inner ring. The flow motion induced by the tiny current flux is smoothed out by the viscous effect which is similar to the previous case as we have discussed.

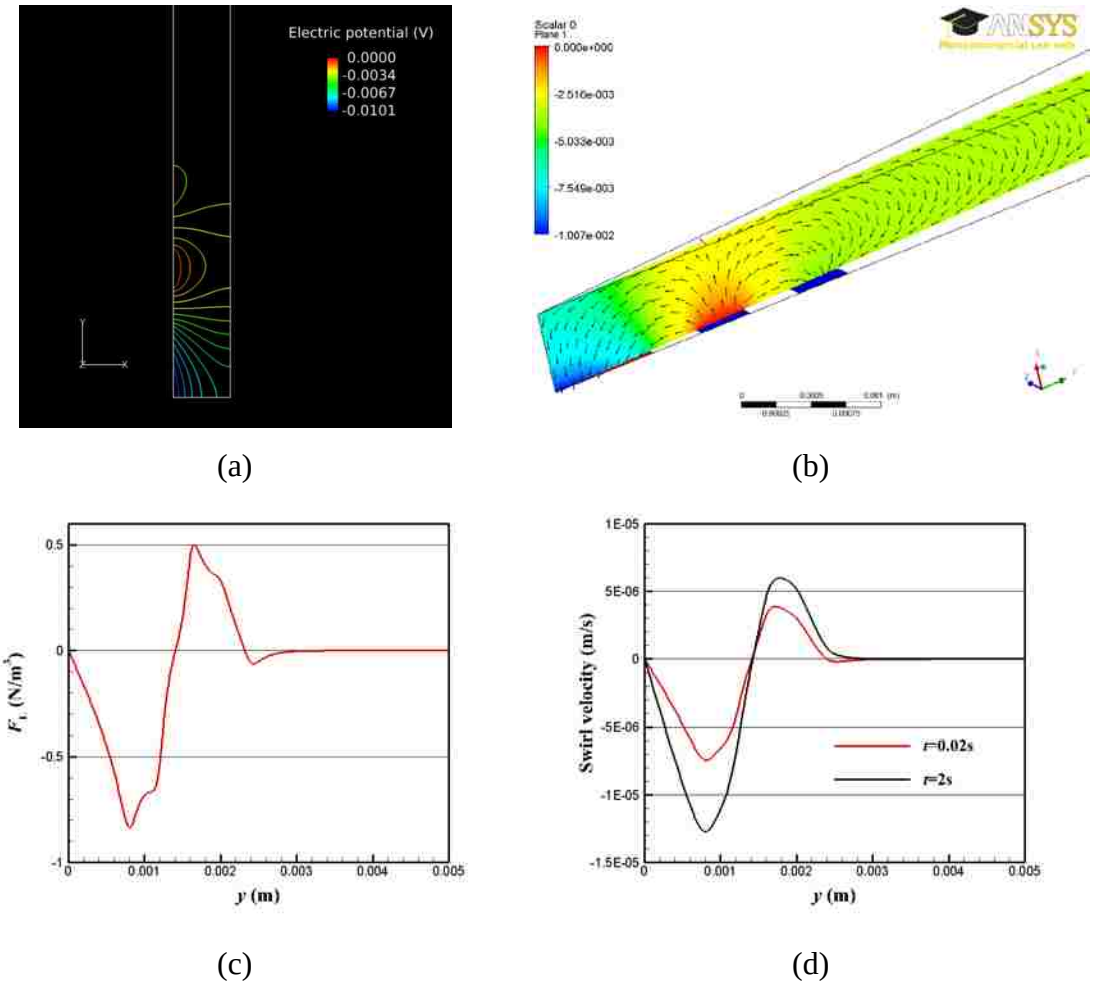

Figure 4.27. (a) Electrical potential contours, (b) ionic current flux distribution. (c) Lorentz force density profile at x=0.1mm at t=2s, and (d) Tangential velocity profile at x=0.1mm at t=0.02s (red) and t=2s (black). Disk/ring/ring model.

4.5.4.4 Ring/ring/ring geometry. The model configuration is shown in Figure 4.16 (d). The width of each ring and the gap between them are 400μm while the inner radius of the first ring is 400μm. A constant current of 5μA is applied on the inner and outer ring which are served as the working electrodes. The maximum velocity of this case can be reached to 17.8 μm/s.

Figure 4.28 shows the electrical potential contours, the ionic current flux distributions, Lorentz force density at x=0.1mm at t=2s and tangential velocity magnitude at x=0.1mm at t=0.02s and 2s. Figure 4.28 (b) shows that there are two tiny ionic current fluxes inside the inner ring and outside the outer ring. Figure 4.28 (d) shows the tangential velocity profile at x=0.1mm at t=0.02s and 2s. From these results we can find that the ring/ring/ring case can control fluid flowing in opposite directions as well. The motion induced by the tiny current flux can be smoothed out by the viscous effect as we have discussed. The ring/ring/ring configuration has a similar MHD flow motion as the disk/ring/ring one. However, in the early stage, small opposite flow motions can be achieved inside the inner ring and outside the outer ring.

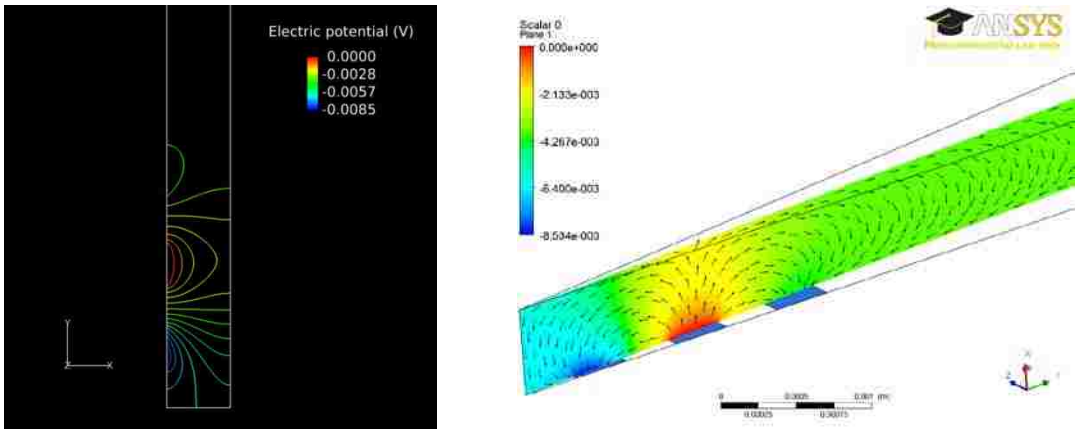

(a) (b)

Figure 4.28. (a) Electrical potential contours, (b) ionic current flux distribution. (c) Lorentz force density profile at x=0.1mm at t=2s, and (d) Tangential velocity profile at x=0.1mm at t=0.02s (red) and t=2s (black). Ring/ring/ring model.

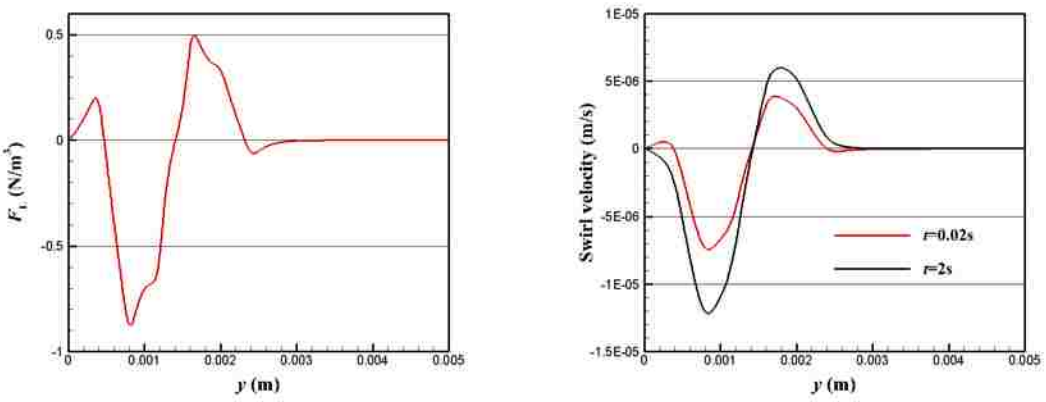

(c) (d)

Figure 4.28. (a) Electrical potential contours, (b) ionic current flux distribution. (c) Lorentz force density profile at x=0.1mm at *t*=2s, and (d) Tangential velocity profile at *x*=0.1mm at *t*=0.02s (red) and *t*=2s (black). Ring/ring/ring model (cont.).

4.5.5. Summary. In this section, different disk and ring geometries are studied to achieve different MHD flow motions for various flow manipulation purposes. Besides, parametric studies on the disk/ring configuration are conducted to investigate the impacts of applied current, magnetic flux density, and cell size on the MHD flow speed. Table 4.4 presents results for different configurations. All cases are subjected to a 5μA constant applied current here. From the results, we can find that both disk/ring and ring/ring configurations can generate a clockwise motion. Although in ring/ring case, the tiny current flux inside the inner ring can generate a small counter clockwise motion in the early stage, it finally is smoothed out by the viscous effect. Both disk/ring/ring and ring/ring/ring can generate a counter-swirling flow, with a clockwise motion inside and a counter clockwise motion outside. These two configurations can be used for specific flow control application.

Table 4.5 presents the results from parameter variations for the disk/ring configuration. Originally, a constant current of 5μA is applied on the ring electrode. From these results, we find that the flow speed is doubled by doubling the applied current, magnetic flux density which is easy to understand. When doubling the cell height and applied current simultaneously, the flow speed increases a lot since both separately

increases the Lorentz force magnitude. By increasing the width of ring electrode, the flow speed decreases because of the decrease of the current density. And by increasing the gap between the disk and ring does not affect the flow speed very much. These results gives us a thorough insight of how the cell size, current and magnetic flux density influence the MHD flow speed. More theoretical work including the non-dimensional analysis of the Navier-Stoke equation with Lorentz force term is required to better understand them.

Table 4.4. Flow motion and maximum flow speed for different configurations

Configuration	Maximum flow speed	Flow motion
Disk/ring	19.8μm/s	Clockwise motion
Ring/ring	18.4μm/s	Clockwise motion
Disk/ring/ring	19.3μm/s	Clockwise motion between disk and inner ring, counter clockwise motion between inner and outer ring
Ring/ring/ring	17.8μm/s	Clockwise motion between inner ring and middle ring, counter clockwise motion between middle and outer ring

Table 4.5. Results from parameter variations for the disk/ring configuration

Parameter variations	Maximum flow speed
Original case (i=5μA)	19.8μm/s
Doubling applied current (i=10μA)	39.6μm/s
Doubling magnetic flux density	39.6μm/s
Doubling cell height and applied current	50.7μm/s

Table 4.5. Results from parameter variations for the disk/ring configuration (cont.)

Doubling cell size and applied current	39.6μm/s
Doubling the width of ring electrode	11.8μm/s
Doubling the gap between disk and ring	20.4μm/s

4.6. CONCLUSION

In this chapter, we present the mathematical model and CFD simulations of MHD arising from redox reactions at conducting polymer modified electrodes. By relying on transmission line circuit model, the typical CA (chronoamperometry), CP (chronopotentiometry) and CV (cyclic voltammetry) responses of the conducting polymer can be obtained, and good agreements are achieved compared with the experiments and equivalent circuit models. Results show that the conducting polymer-supporting electrolyte combination has advantage over bare metal electrodes with low concentrated redox species in solution in generating higher electric current. By using either controlled potential and controlled current methods, MHD flow at microband conducting polymer modified electrodes in microfluidic cells can be achieved. For controlled potential method, electric current starts with a large value (~2mA) which causes an impressive flow speed (~500μm/s) with potential difference of 1V between two polymer modified microband electrodes, and then both electric current and flow speed decrease over time within 5s. The fluid flow can be manipulated more precisely under controlled current method. A steady but smaller flow speed (~37.6μm/s) is achieved with i=-50μA, but with a longer sustainable duration (~29.8s). Due to the limited maximum charge that can be held by the conducting polymer film, the pumping duration is inversely proportional to the applied current. Therefore, for a larger applied current (~400μA), pumping can be sustained for a shorter duration (~3.725s). However different strategies can be adopted for different applications. Parametric studies are also conducted on disk and ring geometries with different flow manipulation purposes. Results indicate the feasibility for using conducting polymer modified electrode to achieve multipurpose flow manipulations. Furthermore, several techniques such as film discharging-recharging can be used to extend the pumping, which will be addressed in future work. Also more

work is needed to understand how the size of the electrode, polymer film type and cell geometry affect the performance of pumping in such a system. Parametric study shows conducting polymer modified electrode has advantage in manipulating fluid flow for different purposes. Though many excellent working regarding either electrochemistry of conducting polymers or MHD pumping and mixing in microfluidics has been reported, our study builds the bridge between the electrochemistry of conducting polymer films and CFD simulations to predict redox MHD pumping at conducting polymer modified electrodes in microfluidics.

5. CONCLUSION AND FUTURE WORK

In this dissertation, 2D and 3D, transient CFD simulations are conducted to study pumping and mixing in microfluidics driven by Lorentz force. Results show that, by using on-off scheme switching scheme, a “blinking vortex” structure can be generated with the existence of chaotic advection so as to improve the mixing performance in a shallow cylindrical cell. The period T plays an important role in generating chaotic advection. With larger T, more chaotic advection is created in the cell, and then to enhance the mixing performance. In order to create even more chaotic advection, more pairs of electrodes can be activated by using judicious control.

Also, flow pumping using Lorentz force is demonstrated in a shallow cuboid microfluidic cell. Transmission line circuit model is used and extended to investigate the electrochemical properties of conducting polymer modified electrodes. By using conducting polymer modified electrodes, the electric current generated in the supporting electrolyte is shown to be higher than that using bare metal electrodes, and has advantages of avoiding bubble generation and electrode degradation. Therefore, conducting polymer modified electrodes provide a potential approach to manipulate the flow by using MHD effect in microfluidics. However, more work is needed to establish a comprehensive mathematical model so that one can fully understand the ion and electron transport mechanisms inside the polymer film.

This dissertation establishes CFD simulation of MHD flow as a robust tool to study pumping and mixing in a microfluidic cell. The techniques developed in the present work are also applicable in MHD flow control in microfluidics. In microfluidic flow control, a major goal is to precisely manipulate a small amount of fluid sample, for example, moving a small droplet to a specific location. It is possible to rely on Lorentz force coupled with the interfacial tension to move the droplet. More work is needed to further address this topic.

APPENDIX A.

UDF CODE FOR TWO DIMENSIONAL CHAOTIC ADVECTION

In this appendix, UDF code is presented for solving the two-dimensional chaotic advection in Fluent in section 3.1. This UDF includes the source term of Lorentz force, time dependent boundary conditions, and calculation of mixing quality over the whole 2D plane.

```
//Electric field is solved using UDS and setting flux function and transient
function to none.
//Date 12/28/2013:
//modified for migration current studies. KCl solution

#include"udf.h"
#include"sg.h"


#define RGAS  8.314     /* universal gas constant in J/mol-K */
#define T     298.0     /* temperature (K) */

#define B_z   1.75      /* magnetic field intensity x,y,z-components (Tesla)  */

/* Species numbers. Must match order in Fluent panel */


//User-defined memory for storing source terms (x and y momentum)
#define UDM0 0
#define UDM1 1
//
#define UDM2 2  /*User-defined memory for storing electrode current (x and y term)
*/
#define UDM3 3
#define UDM4 4  /*User-defined memory for storing the current magnitude*/



real  m_current, ele_current, voltage, voltage2, st0, alpha;  /* Overpotential and
electrode current declared as global variables */


DEFINE_PROFILE(time_dependent_voltages, thread, position)  /*time-dependent
voltage 1*/
{
       face_t f;
       real t = CURRENT_TIME;
       real pi = 3.14159265359;
       begin_f_loop(f, thread)
{
       voltage = 0.04*sin(pi*t/4.0);

       F_PROFILE(f, thread, position) = voltage;
}
       end_f_loop(f, thread)
}


DEFINE_SOURCE(x_momentum_source,c,t,dS,eqn)
{
```

```
        real source;
        real B_field;
        real NV_VEC(mcur_den);                /* migration current */
        real NV_VEC(curr_density);         /* current density */
        real density, kappa;

        B_field = B_z;
        density = C_R(c,t);              /* density  */

        /* conductivity of 1 mM KCl solution (S/m), for 0.1 M, k=1.290*/
        kappa = 1.290;
        /* Migration current (see Eq. 4.1.14 and 4.1.16, Bard and Faulkner)*/
        /* UDS solution gives the electric field quantitites */

        mcur_den[0] = -kappa*C_UDSI_G(c,t,0)[0];
        mcur_den[1] = -kappa*C_UDSI_G(c,t,0)[1];

        curr_density[0] = mcur_den[0];
        curr_density[1] = mcur_den[1];

            /*Store source terms in UDM */

            C_UDMI(c,t,0) = curr_density[1]*B_field;
            C_UDMI(c,t,1) = -curr_density[0]*B_field;

                  /*Strore current density in UDM*/

               C_UDMI(c,t,2) = curr_density[0];
               C_UDMI(c,t,3) = curr_density[1];

                  /*Calculate and store the current magnitude*/
               C_UDMI(c,t,4) = NV_MAG(curr_density);

        source = C_UDMI(c,t,0);
        dS[eqn] = 0.0;
        return source;
}

DEFINE_SOURCE(y_momentum_source,c,t,dS,eqn)
{
        real source;
            /* Use stored Lorentz force term from x_momentum_source function */
        source = C_UDMI(c,t,1);
        dS[eqn] = 0.0;
        return source;
}

DEFINE_ADJUST(current,d)    /*calculate the current near the working eletrode*/
{
        face_t f;
        real NV_VEC(mcur_den);         /* migration current */
        real NV_VEC(curr_density), NV_VEC(A);
        real  density, kappa;

              /* zone ID for membrane wall-11 zone from Fluent boundary Conditions
panel */
        int wrkele_ID = 5;   /* From boundary conditions panel */
```

```
            /* getting pointer to thread associated with zone ID number for
boundary zone. */
       Thread *t = Lookup_Thread(d,wrkele_ID);  /* face thread */
       /* Initialize currents */
       ele_current=0.0;

       begin_f_loop(f,t)
                    /* loop over all faces in a given face thread */
       {
          cell_t c0 = F_C0(f,t);  /* cell next to wall face  */
          Thread *t0 = t->t0;     /*     */
              density = C_R(c0,t0);       /* density  */

              /* Conductivity */
              kappa = 1.290;
              /* Migration current (see Eq. 4.1.14 and 4.1.16, Bard and
Faulkner)*/
       mcur_den[0] = -kappa*C_UDSI_G(c0,t0,0)[0];
       mcur_den[1] = -kappa*C_UDSI_G(c0,t0,0)[1];

       curr_density[0] =  mcur_den[0];
       curr_density[1] =  mcur_den[1];

              F_AREA(A,f,t);
       /* Calculate cell face currents = sum (curr_density.DOT.faceArea. The
negative
       sign is included because the area vector is positive pointing outward. See
Fluent UDF manual*/
              m_current      += -NV_DOT(mcur_den,A);
              ele_current    += -NV_DOT(curr_density,A);
       }
       end_f_loop(f,t)
}


DEFINE_ON_DEMAND(st_zero)      /*calculate the mixing quality over the entire
domain*/
{
       Domain *d;
       real volume,vol_tot=0.0;
       real massfrc=0.0;
       real gavg=0.0;
       real stsqr=0.0;

       Thread *t;
       cell_t c;
       d = Get_Domain(1);

       /*this loop is to calculate the average concentration*/
       thread_loop_c(t,d)
       {
       begin_c_loop(c,t)
       {
       volume = C_VOLUME(c,t);
       vol_tot += volume;
       massfrc = F_YI(c,t,1);
       gavg += massfrc*volume;
       }
```

```
        end_c_loop(c,t)
        }

        gavg /= vol_tot;

        /*this loop is to calculate the mixing quality*/
        thread_loop_c(t,d)
        {
        begin_c_loop(c,t)
        {
        volume = C_VOLUME(c,t);
        massfrc = F_YI(c,t,1);
        stsqr += (massfrc-gavg)*(massfrc-gavg)*volume;
        }
        end_c_loop(c,t)
        }

        st0 = stsqr;
}



DEFINE_EXECUTE_AT_END(cur_time)
{
        FILE *fp1;
        fp1 = fopen("current.dat","a");
        fprintf(fp1,"%f      %f     %f\n",CURRENT_TIME, ele_current, voltage);
        fclose(fp1);

}


DEFINE_EXECUTE_AT_END(mixing_quality)
{
        Domain *d;
        real volume,vol_tot=0.0;
        real massfrc=0.0;
        real gavg=0.0;
        real stsqr=0.0;

        Thread *t;
        cell_t c;
        d = Get_Domain(1);

        /*this loop is to calculate the average concentration*/
        thread_loop_c(t,d)
        {
        begin_c_loop(c,t)
        {
        volume = C_VOLUME(c,t);
        vol_tot += volume;
        massfrc = F_YI(c,t,1);
        gavg += massfrc*volume;
        }
        end_c_loop(c,t)
        }

        gavg /= vol_tot;
```

```
        /*this loop is to calculate the mixing quality*/
        thread_loop_c(t,d)
        {
        begin_c_loop(c,t)
        {
        volume = C_VOLUME(c,t);
        massfrc = F_YI(c,t,1);
        stsqr += (massfrc-gavg)*(massfrc-gavg)*volume;
        }
        end_c_loop(c,t)
        }

        alpha = 1.0-stsqr/st0;

        {
        FILE *fp2;
        fp2 = fopen("mixing_quality.dat","a");
        fprintf(fp2,"%f      %f     %f\n",CURRENT_TIME, alpha, st0);
        fclose(fp2);
        }
}


DEFINE_EXECUTE_AT_END(maxv_time)
{
        Domain *d;
        Thread *t;
        real vmax=0.0;
        real NV_VEC(vel);
        real vv;

        cell_t c;
        d = Get_Domain(1);     /* mixture domain if multiphase */

        /*calculate the maximum velocity*/
        thread_loop_c(t,d)
        {
        begin_c_loop(c,t)
        {
        vel[0] = C_U(c,t);
        vel[1] = C_V(c,t);
        vv = NV_MAG(vel);
        if (vv > vmax || vmax == 0.0) vmax = vv;
        }
        end_c_loop(c,t)
        }

        {
        FILE *fp;
        fp = fopen("maxvelocity.dat","a");
        fprintf(fp,"%f       %f     %f\n",CURRENT_TIME, vmax*1000.0);
        fclose(fp);
        }
}
```

APPENDIX B.

STOKES FLOW IN FLUENT

Due to the fact that Fluent cannot deal with the Stokes flow directly, we use some tricks to solve the Stokes flow in Fluent. The main idea is to use three UDS (user define scalars) to equalize the velocity components in momentum equation. More details are presented in this appendix.

Generally, Stokes equation can be written as,

$$\rho\frac{\partial\vec{V}}{\partial t}=-\nabla P+\mu\nabla^2\vec{V}+\vec{f} \tag{B1}$$

Where $\vec{f}$ is Lorentz force which is $\vec{f}=j\times B$.

While UDS equation in Fluent is in form,

$$\frac{\partial\rho\phi_k}{\partial t}+\frac{\partial}{\partial x_i}\left(\rho u_i\phi_k-\Gamma_k\frac{\partial\phi_k}{\partial x_i}\right)=S_{\phi_k} \tag{B2}$$

where the second and third term on the left side of equation are convection and diffusion term respectively. The single term on the right side is source term.

Therefore, if we drop off the pressure gradient term in Stokes equation (B1) which is very small in microfluidics, we can use three UDS equations to equalize the Stokes equation. In our simulations, we specify three UDS without the convective term to construct the Stokes equation,

$$\begin{cases}\dfrac{\partial\rho\phi_1}{\partial t}+\dfrac{\partial}{\partial x_i}\left(-\Gamma\dfrac{\partial\phi_1}{\partial x_i}\right)=f_x\\[2ex]\dfrac{\partial\rho\phi_2}{\partial t}+\dfrac{\partial}{\partial x_i}\left(-\Gamma\dfrac{\partial\phi_2}{\partial x_i}\right)=f_y\\[2ex]\dfrac{\partial\rho\phi_3}{\partial t}+\dfrac{\partial}{\partial x_i}\left(-\Gamma\dfrac{\partial\phi_3}{\partial x_i}\right)=f_z\end{cases} \tag{B3}$$

Where ϕ_1, ϕ_2 and ϕ_3 are the three components of velocity vector, $\phi_1=u$, $\phi_2=v$ and $\phi_3=w$. As a result, the flow velocity magnitude can be calculated by $|V|=\sqrt{\phi_1^2+\phi_2^2+\phi_3^2}$. Γ, the diffusion coefficient in UDS equation now is the dynamic viscosity μ in Stokes flow.

APPENDIX C.

UDF CODE FOR THREE DIMENSIONAL CHAOTIC ADVECTION

This appendix provides the UDF code for three dimensional chaotic advection in section 3.2 in Fluent. The UDF includes source term of Lorentz force in momentum equation, time-dependent boundary conditions and integration of stretching plot.

```
#include"udf.h"
#include"sg.h"


#define B_x   0      /* magnetic field intensity x,y,z-components (Tesla)  */
#define B_y   0.0
#define B_z   0.36
#define T_p   4.0

/* Species numbers. Must match order in Fluent panel */


//User-defined memory for storing source terms
#define UDM0 0
#define UDM1 1
#define UDM2 2
//
#define UDM3 3  /*User-defined memory for storing electrode current */
#define UDM4 4
#define UDM5 5
#define UDM6 6


real  m_current, ele_current, voltageA, voltageB, voltageC, voltageD; /*

int parID[90000];                   /*store the particle ID of the corresponding
vector on it*/
float Mvector[90000][3];            /*initial vector on each particle*/
float par[90000][3];                /*particle x, y coordinates and local
stretching rate*/
float deform[90000][4];              /*deformation tensor*/


DEFINE_PROFILE(t_voltageA, thread, position)  /*time-dependent voltage A*/
{
       face_t f;
       real t = CURRENT_TIME;
       int d;
       begin_f_loop(f, thread)
{
       d = floor(2.0*t/T_p);
       if (d%2 == 0)
              voltageA = 0.04;
       else
              voltageA = 0.0;

       F_PROFILE(f, thread, position) = voltageA;
}
       end_f_loop(f, thread)
}
```

```
DEFINE_PROFILE(t_voltageB, thread, position)  /*time-dependent voltage B*/
{
	face_t f;
	real t = CURRENT_TIME;
	int d;
	begin_f_loop(f, thread)
{
	d = floor(2.0*t/T_p);
	if (d%2 == 0)
		voltageB = 0.0;
	else
		voltageB = 0.04;

	F_PROFILE(f, thread, position) = voltageB;
}
	end_f_loop(f, thread)
}


DEFINE_PROFILE(t_voltageC, thread, position)  /*time-dependent voltage C*/
{
	face_t f;
	real t = CURRENT_TIME;
	int d;
	begin_f_loop(f, thread)
{
	d = floor(2.0*t/T_p);
	if (d%2 == 0)
		voltageC = -0.04;
	else
		voltageC = 0.0;

	F_PROFILE(f, thread, position) = voltageC;
}
	end_f_loop(f, thread)
}


DEFINE_PROFILE(t_voltageD, thread, position)  /*time-dependent voltage D*/
{
	face_t f;
	real t = CURRENT_TIME;
	int d;
	begin_f_loop(f, thread)
{
	d = floor(2.0*t/T_p);
	if (d%2 == 0)
		voltageD = 0.0;
	else
		voltageD = -0.04;

	F_PROFILE(f, thread, position) = voltageD;
}
	end_f_loop(f, thread)
}


DEFINE_SOURCE(x_momentum_source,c,t,dS,eqn)
```

```
{
        real source;
        real NV_VEC(B_field);       /* Declare B-field as a vector */
        real NV_VEC(mcur_den);             /* migration current */
        real NV_VEC(curr_density);         /* current density */
        real density, kappa;

        B_field[0] = B_x;
        B_field[1] = B_y;
        B_field[2] = B_z;
        density = C_R(c,t);  /* density  */

        /* conductivity of NaCl  solution (S/m), for 0.1 M, k=1.290*/
        kappa = 1.29;
        /* Migration current (see Eq. 4.1.14 and 4.1.16, Bard and Faulkner)*/
        /* UDS solution gives the electric field quantitites */

        mcur_den[0] = -kappa*C_UDSI_G(c,t,0)[0];
        mcur_den[1] = -kappa*C_UDSI_G(c,t,0)[1];
        mcur_den[2] = -kappa*C_UDSI_G(c,t,0)[2];

        curr_density[0] = mcur_den[0];
        curr_density[1] = mcur_den[1];
        curr_density[2] = mcur_den[2];

            /*Store source terms in UDM */

            C_UDMI(c,t,0) = NV_CROSS_X(curr_density,B_field);
            C_UDMI(c,t,1) = NV_CROSS_Y(curr_density,B_field);
            C_UDMI(c,t,2) = NV_CROSS_Z(curr_density,B_field);

                  /*Strore current density in UDM*/

               C_UDMI(c,t,3) = curr_density[0];
               C_UDMI(c,t,4) = curr_density[1];
               C_UDMI(c,t,5) = curr_density[2];

                  /*Calculate and store the current magnitude*/
               C_UDMI(c,t,6) = NV_MAG(curr_density);

        source = C_UDMI(c,t,0);
        dS[eqn] = 0.0;
        return source;
}

DEFINE_SOURCE(y_momentum_source,c,t,dS,eqn)
{
        real source;
            /* Use stored Lorentz force term from x_momentum_source function */
        source = C_UDMI(c,t,1);
        dS[eqn] = 0.0;
        return source;
}

DEFINE_SOURCE(z_momentum_source,c,t,dS,eqn)
{
        real source;
           /* Use Lorentz force term from x_momentum_source function */
```

```
        source = C_UDMI(c,t,2);
        dS[eqn] = 0.0;
        return source;
}

DEFINE_ADJUST(current,d)
{
        face_t f;
        real NV_VEC(mcur_den);         /* migration current */
        real NV_VEC(curr_density);
        real NV_VEC(A);
        real A_ele = 0.0;            /* Initialize Electrode area */
        real kappa = 1.29;           /* S/m */

/* zone ID for membrane wall-5 zone from Fluent boundary Conditions panel */
        int ID = 7;
/* getting pointer to thread associated with zone ID number for boundary zone.
membrane mesh.3 */
        Thread *t = Lookup_Thread(d,ID);  /* face thread */
        ele_current = 0.0;

        begin_f_loop(f,t)
        /* loop over all faces in a given face thread */
        {
            cell_t c0 = F_C0(f,t);  /* cell next to wall face  */
            Thread *t0 = t->t0;     /*     */

/* Migration current (see Eq. 4.1.14 and 4.1.16, Bard and Faulkner)*/
        mcur_den[0] = -kappa*C_UDSI_G(c0,t0,0)[0];
        mcur_den[1] = -kappa*C_UDSI_G(c0,t0,0)[1];
        mcur_den[2] = -kappa*C_UDSI_G(c0,t0,0)[2];

        curr_density[0] =  mcur_den[0];
        curr_density[1] =  mcur_den[1];
        curr_density[2] =  mcur_den[2];

        F_AREA(A,f,t);
/* Calculate electrode current = sum (curr_density.DOT.Area  */
        ele_current += NV_DOT(curr_density,A);
/* Calculate electrode area  */
        A_ele += NV_MAG(A);

        }
        end_f_loop(f,t)
}


DEFINE_EXECUTE_AT_END(exe_at_end)
{
        FILE *fp1;
        fp1 = fopen("current.dat","a");
        fprintf(fp1,"%f      %f     %f\n",CURRENT_TIME, ele_current*1.0e6,
voltageA);
        fclose(fp1);

}
```

```
DEFINE_EXECUTE_AT_END(maxv_time)
{
	Domain *d;
	Thread *t;
	real vmax=0.0;
	real NV_VEC(vel);
	real vv;

	cell_t c;
	d = Get_Domain(1);	/* mixture domain if multiphase */

	/*calculate the maximum velocity*/
	thread_loop_c(t,d)
	{
	begin_c_loop(c,t)
	{
	vel[0] = C_U(c,t);
	vel[1] = C_V(c,t);
	vel[2] = C_W(c,t);
	vv = NV_MAG(vel);
	if (vv > vmax || vmax == 0.0) vmax = vv;
	}
	end_c_loop(c,t)
	}

	{
	FILE *fp;
	fp = fopen("maxvelocity.dat","a");
	fprintf(fp,"%f	%f  %f\n",CURRENT_TIME, vmax*1000.0);
	fclose(fp);
	}
}


DEFINE_EXECUTE_AT_END(particle_position)
{
	real x,y,z;
	real u,v,w;
	Particle *p;
	Injection *Ilist;
	Injection *I;
	Ilist = Get_dpm_injections();

	if (fmod(CURRENT_TIME, T_p) == 0.0)
	{
	FILE *fp;
	char whoru[80];
	sprintf(whoru,"positions%6.1f.out",CURRENT_TIME);
	fp = fopen(whoru, "a");

	loop(I,Ilist)
	{
	loop(p,I->p)
	{
		int id = p->part_id;
		x = P_POS(p)[0];
		y = P_POS(p)[1];
		u = P_VEL(p)[0];
```

```
                v = P_VEL(p)[1];
#if RP_3D
                z = P_POS(p)[2];
                w = P_VEL(p)[2];
#endif
#if RP_3D
                fprintf(fp,"%i %f %e %e %e %e %e %e \n", id, CURRENT_TIME, x, y, z,
u, v, w);
#else
                fprintf(fp,"%i %f %e %e %e %e \n", id, CURRENT_TIME, x, y, u, v);
#endif
        }
        }
        fclose(fp);
        }
}


/*subroutine to read the random original vectors on each particle*/
DEFINE_ON_DEMAND(read_original_vectors)
{
        FILE *fp;
        int n=90000;
        int i=0;
    Message("Reading UDF data from data file...\n");
        fp = fopen("random.dat", "r");

        for (i = 0 ; i < n ; i++)
        {
                fscanf(fp, "%e %e
%e\n",&Mvector[i][0],&Mvector[i][1],&Mvector[i][2]);

                /*initialize the deformation tensor on each particle*/
                deform[i][0]=1.0;
                deform[i][1]=0.0;
                deform[i][2]=0.0;
                deform[i][3]=1.0;

        }
        fclose(fp);

}


/*Calculate the rlamba (stretching ratio) on each particle*/
DEFINE_EXECUTE_AT_END(stretching_ratio)
{
        Thread *tc;
        cell_t c;

        int k=0;
        real dudx,dudy,dvdx,dvdy;
        float rk[4][6];         /*Cash-Karp fifth order Runger-Kutta coefficients*/
        real h0,h1,h2,h3;
        real dt=CURRENT_TIMESTEP;
        real dx,dy;

        Particle *p;
```

```
        Injection *Ilist;
        Injection *I;
        Ilist = Get_dpm_injections();


/*loop over all the particles in the domain*/
        loop(I,Ilist)
        {
        loop(p,I->p)
        {
                int id = p->part_id;
                k += 1;
                parID[k-1] = id;              /*store the particle ID*/
                par[k-1][0]=P_POS(p)[0];      /*store the x coordinate*/
                par[k-1][1]=P_POS(p)[1];      /*store the y coordinate*/

/*find the cell thread in which the particle is*/
                c = P_CELL(p);
                tc = P_CELL_THREAD(p);
                dudx=C_U_G(c,tc)[0];
                dudy=C_U_G(c,tc)[1];
                dvdx=C_U_G(c,tc)[0];
                dvdy=C_U_G(c,tc)[1];

/*Fifth order Runger-Kutta method to solve the Deformation matrix for each
particle*/
/*The four equations are shown below:*/
/*dF11/dt=dudx*F11+dvdx*F21*/
/*dF12/dt=dudx*F12+dvdx*F22*/
/*dF21/dt=dudy*F11+dvdy*F21*/
/*dF22/dt=dudy*F12+dvdy*F22*/
/*If we suppose F11=y1, F12=y2, F21=y3, F22=y4, the four equations become:*/
/* dy1/dt=dudx*y1+dvdx*y3, dy2/dt=dudx*y2+dvdx*y4, dy3/dt=dudy*y1+dvdy*y3 and
dy4/dt=dudy*y2+dvdy*y4 */

/*k1 coefficients*/
                rk[0][0]=dudx*deform[k-1][0]+dvdx*deform[k-1][2];
                rk[1][0]=dudx*deform[k-1][1]+dvdx*deform[k-1][3];
                rk[2][0]=dudy*deform[k-1][0]+dvdy*deform[k-1][2];
                rk[3][0]=dudy*deform[k-1][1]+dvdy*deform[k-1][3];

/*k2 coefficients*/
                h0=deform[k-1][0]+rk[0][0]*dt/5.0;    /*y1'*/
                h1=deform[k-1][1]+rk[1][0]*dt/5.0;    /*y2'*/
                h2=deform[k-1][2]+rk[2][0]*dt/5.0;    /*y3'*/
                h3=deform[k-1][3]+rk[3][0]*dt/5.0;    /*y4'*/

                rk[0][1]=dudx*h0+dvdx*h2;
                rk[1][1]=dudx*h1+dvdx*h3;
                rk[2][1]=dudy*h0+dvdy*h2;
                rk[3][1]=dudy*h1+dvdy*h3;

/*k3 coeffcients*/
                h0=deform[k-1][0]+3.0*rk[0][0]*dt/40.0+9.0*rk[0][1]*dt/40.0;
                h1=deform[k-1][1]+3.0*rk[1][0]*dt/40.0+9.0*rk[1][1]*dt/40.0;
                h2=deform[k-1][2]+3.0*rk[2][0]*dt/40.0+9.0*rk[2][1]*dt/40.0;
                h3=deform[k-1][3]+3.0*rk[3][0]*dt/40.0+9.0*rk[3][1]*dt/40.0;
```

```
                rk[0][2]=dudx*h0+dvdx*h2;
                rk[1][2]=dudx*h1+dvdx*h3;
                rk[2][2]=dudy*h0+dvdy*h2;
                rk[3][2]=dudy*h1+dvdy*h3;

/*k4 coefficients*/
                h0=deform[k-1][0]+3.0*rk[0][0]*dt/10.0-
9.0*rk[0][1]*dt/10.0+6.0*rk[0][2]*dt/5.0;
                h1=deform[k-1][1]+3.0*rk[1][0]*dt/10.0-
9.0*rk[1][1]*dt/10.0+6.0*rk[1][2]*dt/5.0;
                h2=deform[k-1][2]+3.0*rk[2][0]*dt/10.0-
9.0*rk[2][1]*dt/10.0+6.0*rk[2][2]*dt/5.0;
                h3=deform[k-1][3]+3.0*rk[3][0]*dt/10.0-
9.0*rk[3][1]*dt/10.0+6.0*rk[3][2]*dt/5.0;

                rk[0][3]=dudx*h0+dvdx*h2;
                rk[1][3]=dudx*h1+dvdx*h3;
                rk[2][3]=dudy*h0+dvdy*h2;
                rk[3][3]=dudy*h1+dvdy*h3;

/*k5 coefficients*/
                h0=deform[k-1][0]-11.0*rk[0][0]*dt/54.0+5.0*rk[0][1]*dt/2.0-
70.0*rk[0][2]*dt/27.0+35.0*rk[0][3]*dt/27.0;
                h1=deform[k-1][1]-11.0*rk[1][0]*dt/54.0+5.0*rk[1][1]*dt/2.0-
70.0*rk[1][2]*dt/27.0+35.0*rk[1][3]*dt/27.0;
                h2=deform[k-1][2]-11.0*rk[2][0]*dt/54.0+5.0*rk[2][1]*dt/2.0-
70.0*rk[2][2]*dt/27.0+35.0*rk[2][3]*dt/27.0;
                h3=deform[k-1][3]-11.0*rk[3][0]*dt/54.0+5.0*rk[3][1]*dt/2.0-
70.0*rk[3][2]*dt/27.0+35.0*rk[3][3]*dt/27.0;

                rk[0][4]=dudx*h0+dvdx*h2;
                rk[1][4]=dudx*h1+dvdx*h3;
                rk[2][4]=dudy*h0+dvdy*h2;
                rk[3][4]=dudy*h1+dvdy*h3;

/*k6 coefficients*/
                h0=deform[k-
1][0]+1631*rk[0][0]*dt/55296+175*rk[0][1]*dt/512+575*rk[0][2]*dt/13824+44275*rk[0]
[3]*dt/110592+253*rk[0][4]*dt/4096;
                h1=deform[k-
1][1]+1631*rk[1][0]*dt/55296+175*rk[1][1]*dt/512+575*rk[1][2]*dt/13824+44275*rk[1]
[3]*dt/110592+253*rk[1][4]*dt/4096;
                h2=deform[k-
1][2]+1631*rk[2][0]*dt/55296+175*rk[2][1]*dt/512+575*rk[2][2]*dt/13824+44275*rk[2]
[3]*dt/110592+253*rk[2][4]*dt/4096;
                h3=deform[k-
1][3]+1631*rk[3][0]*dt/55296+175*rk[3][1]*dt/512+575*rk[3][2]*dt/13824+44275*rk[3]
[3]*dt/110592+253*rk[3][4]*dt/4096;

                rk[0][5]=dudx*h0+dvdx*h2;
                rk[1][5]=dudx*h1+dvdx*h3;
                rk[2][5]=dudy*h0+dvdy*h2;
                rk[3][5]=dudy*h1+dvdy*h3;

/*final solution of deformation tensor*/
                deform[k-1][0] +=
(2825*rk[0][0]/27648+18575*rk[0][2]/48384+13525*rk[0][3]/55296+277*rk[0][4]/14336+
rk[0][5]/6)*dt;
```

```
              deform[k-1][1] +=
(2825*rk[1][0]/27648+18575*rk[1][2]/48384+13525*rk[1][3]/55296+277*rk[1][4]/14336+
rk[1][5]/6)*dt;
              deform[k-1][2] +=
(2825*rk[2][0]/27648+18575*rk[2][2]/48384+13525*rk[2][3]/55296+277*rk[2][4]/14336+
rk[2][5]/6)*dt;
              deform[k-1][3] +=
(2825*rk[3][0]/27648+18575*rk[3][2]/48384+13525*rk[3][3]/55296+277*rk[3][4]/14336+
rk[3][5]/6)*dt;

/*new vector on each particle after stretching*/
/* dx=F*dx0 */
              dx=deform[k-1][0]*Mvector[k-1][0]+deform[k-1][1]*Mvector[k-1][1];
              dy=deform[k-1][2]*Mvector[k-1][0]+deform[k-1][3]*Mvector[k-1][1];

/*calculate the stretching ratio on each particle and output*/
              par[k-1][2]=sqrt(dx*dx+dy*dy)/Mvector[k-1][2];

              /*output the results*/
              if (fmod(CURRENT_TIME, T_p) == 0.0)
              {
              FILE *fp;
              char whoru[80];
              sprintf(whoru,"time%6.1f.out",CURRENT_TIME);
              fp = fopen(whoru, "a");
              fprintf(fp,"%e %e %e\n",par[k-1][0],par[k-1][1],par[k-2][2]);
              fclose(fp);
              }

       }
       }


}


DEFINE_EXECUTE_AT_END(udm_rlambda)
{
       Thread *c_t;
       cell_t c;

       int num_part=0;
       int parcel_trapped=0;
       float number_in_parcel=0.0;

       Particle *p;
       Injection *Ilist;
       Injection *I;
       Ilist = Get_dpm_injections();

       loop(I,Ilist)
       {
       loop(p,I->p)
       {
              int id = p->part_id;
              c = P_CELL(p);
              c_t = P_CELL_THREAD(p);
              parcel_trapped+=1;
```

```
                num_part=p->number_in_parcel;
        }
        }

        Message("num_part: %d\n",num_part);
        Message("parcel_trapped: %d\n",parcel_trapped);
        Message("number_in_parcel: %f\n",number_in_parcel);

}
```

APPENDIX D.

FORTRAN CODE FOR CONCENTRATION OF NUMERICAL PARTICLES

In this appendix, Fortran code for calculating the concentration of numerical particles in section 3.2 is present.

```
      program main
      implicit double precision (a-h,o-z)
      dimension pc(200,200,3)      !particle coordinates in each box pc
      dimension ibox(4,40500)      !box matrix, store local box vertices
      dimension p(2,40500)  !store the global mesh nodes coordinates of each box
      dimension p0(1000000,3),p1(1000000,3)
      dimension xver(4),yver(4)
      parameter(pi=3.14159265359)


!partition and particle informations
      n=200       !number of partitions each side
      nl=n+1      !number of mesh nodes per side
      nlt=nl*nl   !number of total mesh nodes
      nb=n*n      !number of total boxes in the domain
      nt0=250873
      nt1=251678

!mesh geometry information
      rleft=-3.0d-03
      right=3.0d-03
      top=3.0d-03
      bottom=-3.0d-03

      h1=(right-rleft)/dfloat(n)
      h2=(top-bottom)/dfloat(n)

!setup p matrix
      do i=1,nl
      do j=1+(i-1)*nl,i*nl
      p(1,j)=rleft+dfloat(i-1)*h1
      p(2,j)=bottom+dfloat(j-(i-1)*nl-1)*h2
      enddo
      enddo

      open(unit=1,file='p_matrix.dat')
      do i=1,nlt
      write(1,100) p(1,i), p(2,i)
      enddo
      close(1)
100   format(e12.5,1x,e12.5)

!setup the box matrix which stores the local index of vertices of each box
      do i=1,n
      do j=1+(i-1)*n,i*n
      ibox(1,j)=j+(i-1)
      ibox(2,j)=ibox(1,j)+nl
      ibox(3,j)=ibox(2,j)+1
      ibox(4,j)=ibox(1,j)+1
      enddo
      enddo
```

```
      open(unit=2,file='box_matrix.dat')
      do i=1,nb
      write(2,200) ibox(1,i),ibox(2,i),ibox(3,i),ibox(4,i)
      enddo
200   format(i6,1x,i6,1x,i6,1x,i6)
      close(2)

!read two particle injections
      open(unit=3,file='materialline1.his')
      do i=1,nt0
      read(3,*) t,p0(i,1),p0(i,2),p0(i,3)
      enddo
      close(3)

      open(unit=4,file='materialline2.his')
      do i=1,nt1
      read(4,*) t,p1(i,1),p1(i,2),p1(i,3)
      enddo
      close(4)

!main program, loop over all elements
      open(unit=5,file='result.dat')
      write(5,*) 'VARIABLES="X","Y","n0","n1","c"'
      write(5,*) 'ZONE T="1", I=200, J=200, DATAPACKING=POINT'
      open(unit=6,file='mixing_quality.dat')
      write(6,*) 'VARIABLES="T","delta","alpha"'

      temp=0.0d0
      delta0=0.25d0*pi*rleft**2.0d0      !standard deviation at t=0
      ds=h1*h2                           !area of each grid box
      nbt=0          !number of box in which include at least two particles

c count the number of box
      do i=1,nb
      do k=1,4
      xver(k)=p(1,ibox(k,i))
      yver(k)=p(2,ibox(k,i))
      enddo
      call find_particles(p0,nt0,p1,nt1,xver,yver,xc,yc,n0,n1,c)
      if((n0.eq.0).and.(n1.eq.0)) then
      elseif((n0.eq.0).or.(n1.eq.0)) then
      else
      nbt=nbt+1
      endif
      enddo
      write(6,500) nbt,dfloat(nbt)*ds
500   format(i6,1x,e12.6)


      do i=1,nb
      do k=1,4
      xver(k)=p(1,ibox(k,i))
      yver(k)=p(2,ibox(k,i))
      enddo
      call find_particles(p0,nt0,p1,nt1,xver,yver,xc,yc,n0,n1,c)
      write(5,300) xc,yc,n0,n1,c

      if((n0.eq.0).and.(n1.eq.0)) then
```

```
      else
      temp=temp+((c-0.5d0)**2.0d0)*ds
      endif

      enddo

      delta=temp
      alpha=1.0d0-delta/delta0
      write(6,400) t,delta,alpha

      close(5)
300   format(f12.6,1x,f12.6,1x,i6,1x,i6,1x,f12.6)
400   format(f12.6,1x,e12.6,1x,f12.6)

      end program


c
c     subroutine to calculate the concentration inside the box
c
      subroutine find_particles(p0,nt0,p1,nt1,xver,yver,xc,yc,n0,n1,c)
      implicit double precision (a-h,o-z)
      dimension xver(4),yver(4)
      dimension p0(1000000,3),p1(1000000,3)

      rleft=xver(1)
      right=xver(3)
      bottom=yver(1)
      top=yver(3)
      xc=(rleft+right)/2.0d0
      yc=(top+bottom)/2.0d0

      n0=0
      do i=1,nt0
      x=p0(i,1)
      y=p0(i,2)
      if((x.gt.rleft).and.(x.lt.right).and.(y.gt.bottom).and.(y.lt.top))
     *then
      n0=n0+1
      else
      endif
      enddo

      n1=0
      do i=1,nt1
      x=p1(i,1)
      y=p1(i,2)
      if((x.gt.rleft).and.(x.lt.right).and.(y.gt.bottom).and.(y.lt.top))
     *then
      n1=n1+1
      else
      endif
      enddo

      if ((n1.eq.0).and.(n0.eq.0)) then
      c=0.0d0
      else
      c=dfloat(n0)/dfloat(n0+n1)
```

```
endif

return
end
```

APPENDIX E.

INVERSE LAPLACE TRANSFORM FOR TRANSMIISON LINE CIRCUIT MODEL

In this appendix, Matlab code of inverse Laplace transform for calculation CA, CP and CV responses in section 4.2 is presented.

```
% main
clear all;
clc;

syms s

% control parameters
N=21;                    % mesh grid in length direction
Nt=501;                  % number of time space node

% film parameters
Cv=8e8;                  % volumetric capacitance [F/m^3]
sigma_i=2.2e-2;          % ionic conductivity in polymer
sigma_e=8e3;             % electronic conductivity
h=10e-6;                 % thickness of the polymer
wid=560e-6;              % width of the polymer film
len=2.5e-2;              % length o the film
Ai=wid*len/2;            % half Area per thickness
Ae=wid*h;                % Area per length
Re=1/Ae/sigma_e;         % electronic resistance
Ri=1/Ai/sigma_i;         % ionic resistance
dy=len/2/(N-1);
y=zeros(N,1);            % mesh grid
for i=1:N
    y(i)=(i-1)*dy;
end

% Model impedance
Zc=1/s/Cv/Ai;
Z_1D=sqrt(Ri*Zc)*coth(sqrt(Ri/Zc)*h);

Z_2D=sqrt(Re*Z_1D)*coth(sqrt(Re/Z_1D)*len/2);


%-------------------------------------------------------------------------
----
% potential step 1.0V
V0=1;

V_s=V0/s;

ft=zeros(N,Nt);    % rows stores the length, columns stores time

% loop over the length
for i=N:N

F=(V_s/Z_2D)*(exp(sqrt(Re/Z_1D)*y(i))-exp(-
sqrt(Re/Z_1D)*y(i)))/(exp(sqrt(Re/Z_1D)*len/2)-exp(-
sqrt(Re/Z_1D)*len/2));
F=char(F);
```

```
[t,ft(i,:)]=INVLAP(F,0.01,20,Nt,6,89,129);   % 2D

end



calculate the current density profile along length
jy=zeros(N,1);
for k=1:N
    di=fourth_order_central_differentce(ft(:,Nt/2),k);
    jy(k)=di/dy/wid;
end

figure(1);plot(t,2*ft(N,:),'r-');
axis([0 5 0 5e-3]);

M=2*ft(N,:)';
save('icurrent.dat', 'M', '-ASCII');

%integrate i over t to get the total charge
QC=0;
for i=1:Nt-1
    dt=t(i+1)-t(i);
    QC = QC + 0.5*(2*ft(N,i)+2*ft(N,i+1))*dt;
end

display(QC);


%-------------------------------------------------------------------------
----
% cyclic voltammograms -0.6V-0.6V, scan rate=0.05 V/s
Tp=48;               % time period in second
n=4;                 % number of periods
temp1=exp(-Tp*s)*(0.05+exp(Tp*s/2)*(-0.05+0.6*s)+0.6*s)/s^2;
temp2=(0.05+exp(-Tp*s/2)*(-0.05-0.6*s)-0.6*s)/s^2;
V_s=(temp1+temp2)/(1-exp(-Tp*s));

F1=V_s/Z_2D;
F1=char(F1);
F2=V_s/Z_1D;
F2=char(F2);

[t1,ft1]=INVLAP(F1,0.01,n*Tp,1000,6,89,129);
[t2,ft2]=INVLAP(F2,0.01,n*Tp,1000,6,89,129);
Nt=length(t2);
V_t=zeros(Nt,1);      % Applied potential in t space


for i=1:Nt

    d=floor(t1(i)/(Tp/2));
    if mod(d,2)==0
        V_t(i)=0.05*(t1(i)-d*(Tp/2))-0.6;
```

```
        %V_t(i)=0.005*(t1(i)-d*(Tp/2))-0.455;
    else
        V_t(i)=-0.05*(t1(i)-(d-1)*(Tp/2))+1.8;
        %V_t(i)=-0.005*(t1(i)-(d-1)*(Tp/2))+2.705;
    end


end

figure(1);hAx=plotyy(t1,2*ft1,t1,V_t);xlabel('t [s]');ylabel(hAx(1),'i
[A]');ylabel(hAx(2),'E [V]');
figure(2);plot(V_t,2*ft1,'r-',V_t,ft2*len,'b-');xlabel('E
[V]');ylabel('i [A]');title('cyclic voltammogram');
legend('2_D model','1_D model','location','northwest');


%-------------------------------------------------------------------------
----
% constant applied current
i0=400e-6/2;

i_s=i0/s;

F1=i_s*Z_2D;
F1=char(F1);
F2=i_s*2*Z_1D/len;
F2=char(F2);

[t1,ft1]=INVLAP(F1,0.01,4,200,6,59,109);
[t2,ft2]=INVLAP(F2,0.01,4,200,6,59,109);

figure(1);plot(t1,ft1,'r-',t2,ft2,'b-');xlabel('t [s]');ylabel('E
[V]');title('fixed current');
axis([0 4 0 1.6]);
legend('2_D model','1_D model');


% INVLAP - Numerical Inversion of Laplace Transforms
function [radt,ft]=INVLAP(Fs,tini,tend,nnt,a,ns,nd);
% Fs is formula for F(s) as a string
% tini, tend are limits of the solution interval
% nnt is total number of time instants
% a, ns, nd are parameters of the method
% if not given, the method uses implicit values a=6, ns=20, nd=19
% it is recommended to preserve a=6
% increasing ns and nd leads to lower error
% an example of function calling
% [t,ft]=INVLAP('s/(s^2+4*pi^2)',0,10,1001);
% to plot the graph of results write plot(t,ft), grid on, zoom on
FF=strrep(strrep(strrep(Fs,'*','.*'),'/','./'),'^','.^');
if nargin==4
  a=6; ns=20; nd=19;  end;    % implicit parameters
radt=linspace(tini,tend,nnt); % time vector
if tini==0  radt=radt(2:1:nnt);  end;  % t=0 is not allowed
tic                % measure the CPU time
```

```
for n=1:ns+1+nd                % prepare necessary coefficients
   alfa(n)=a+(n-1)*pi*j;
   beta(n)=-exp(a)*(-1)^n;
end;
n=1:nd;
bdif=fliplr(cumsum(gamma(nd+1)./gamma(nd+2-n)./gamma(n))./2^nd;
beta(ns+2:ns+1+nd)=beta(ns+2:ns+1+nd).*bdif;
beta(1)=beta(1)/2;
for kt=1:nnt                   % cycle for time t
   tt=radt(kt);
   s=alfa/tt;                  % complex frequency s
   bt=beta/tt;
   btF=bt.*eval(FF);           % functional value F(s)
   ft(kt)=sum(real(btF));      % original f(tt)
end;
toc
```

BIBLIOGRAPHY

[1] Haeberie S, and Zengerie R. “Microfluidic platforms for lab-on-a-chip applications,” *Lab Chip*, 7(9) 2007 1094-110.

[2] H.A. Stone, A.D. Stroock, and A. Ajdari. “Engineering Flows in Small Devices,” *Annual Review of Fluid Mechanics*, 36 2004 381-411, DOI: 10.1146/annurev.fluid.36.050802.122124.

[3] S.W. Jones, O.M. Thomas, and H. Aref. “Chaotic advection by laminar flow in a twist pipe,” *J. Fluid Mech*. 209 1989 335-357.

[4] R.H. Liu, K. V. Sharp, M. G. Olsen, M. A. Stremler, J. Santiago, R. J. Adrian, H. Aref, and D. J. Beebe. “A passive three-dimensional ‘C-shape’ helical micromixer,” *J. Microelecgtromech. Syst*. 9(190) 2000 190-7.

[5] A. Yamagishi, T. Inaba and Y. Yamaguchi. “Chaotic analysis of mixing enhancement in steady laminar flows through multiple pipe bends,” *Int J heat Mass Transf*. 50 2007 1238-1247.

[6] N. Nguyen. “Micro-magnetofluidics: interactions between magnetism and fluid flow on the microscale,” *Microfluid Nanofluid*. 12 2012 1-16.

[7] P.A. Davidson. *An Introduction to Magnetohydrodynamics*. Cambridge University Press Cambridge, UK, 2001.

[8] K.M. Isaac, C. Gonzales and D. Sen. “Modeling of redox electrochemical MHD and three-dimensional CFD simulations of transient phenomena in microfluidic cells,” *Microfluid Nanofluid*. 17(5) 2014 943-985.

[9] N. Leventis, M. Chan, X. Gao, M. Canalas and P. Zhang. “Electrochemistry with stationary disk and ring-disk millielectrodes in magnetic fields,” *J. Phys, Chem B.* 102(18) 1998 3512-3522.

[10] D. Sen, K.M. Isaac and N. Leventis. “Investigation of transient redox electrochemical MHD using numerical simulations,” *Int J heat Mass Transf*. 54(25) 2011 5368-5378.

[11] M. C. Weston and I. Fritsch. “Manipulating fluid flow on a chip through controlled-current redox magnetohydrodynamics,” *Sensors and Actuators B:* Chemical. 173 2012 935–944.

[12] S. Qian and H.H Bau. “Magentohydrodynamic flow of Redox electrolyte,” *Physics of Fluids*. 17(6) 2005 067105-067105-12.

[13] C. Eckart. “An analysis of the stirring and mixing processes in incompressible fluids,” *J. Mar. Res*. 7(265) 1948.

[14] G.K. Batchelor. “Small-scale variation of convected quantities like temperature in turbulent fluid Part 1. General discussion and the case of small conductivity,” *J. Fluid Mech*. 5(1) 1959 113-133.

[15] H. Aref. “The development of chaotic advection,” *Physics of Fluids*. 14(4) 2002 1315-1325.

[16] H. Aref. “Stirring by chaotic advection,” *J. Fluid Mech*. 143 1983 1-21.

[17] H. Aref. “Chaotic advection in a Stokes flow,” *Physics of Fluids*. 29(11) 1986 3515-3521.

[18] P.D. Swanson and J.M. Ottino. “A comparative computational and experimental study of chaotic mixing of viscous fluids,” *J. Fluid Mech*. 213 1990 227-249.

[19] J. Chaiken, R. Chevray, M. Tabor and Q.M. Tan. “Experimental study of Lagrangian turbulence in a Stokes flow,” *Proc. R. Soc. Lond. A* 408 1986 165-174.

[20] W.L. Chien, H. Rising and J.M. Ottino. “Laminar mixing and chaotic mixing in several cavity flows,” *J. Fluid Mech*. 170 1986 355-377.

[21] M. Yi, S. Qian and H.H Bau. “A magnetohydrodynamic chaotic stirrer,” *J. Fluid Mech*. 468 2002 153-177.

[22] S. Qian, J. Zhu and H.H Bau. “A stirrer for magnetohydrodynamically controlled minute fluidic networks,” *Physics of Fluids*. 14(10) 2002 3584-3592.

[23] S. Qian and H.H Bau. “Magnetohydrodynamic stirrer for stationary and moving fluids,” *Sensors and Actuators B.* 106 2005 859-970.

[24] L. Rossi, D. Doorly and D. Kustrin. “Lamination and mixing in three fundamental flow sequences driven by electromagnetic body forces,” *Physical Review E*. 86 2012 026313-1-14.

[25] S. Dufour, G. Vinsard, J.P. Mota and E. Saatdjian. “Mixing by chaotic advection in a magneto-hydrodynamic driven flow,” *Physics of Fluids*. 25(10) 2013 102001-102001-16.

[26] S. Gopalakrishnan and A. Thess. “Electromagetically induced chaotic mixing in a pipe mixer,” *Chemical Engineering Science*. 65 2010 6282-6291.

[27] F. Yuan and K.M. Isaac. “A study of MHD-induced mixing in microfluidics using CFD simulations,” *Micro and Nanosystems*. 6(3) 2014 178-192.

[28] A.V. Lemoff, A.P. Lee. “An AC magnetohydrodynamic micropump,” *Sensors and Actuators B.* 63(3) 2000 178-185.

[29] S. Qian, J. Zhu and H.H. Bau. “A stirrer for magnetohydrodynamically controlled minute fluidic network,” *Physics of Fluids*. 14(10) 2002 3584-3592.

[30] M.C. Weston, C.K. Nash and I. Fritsch. “Redox-Magnetodynamic microfluidics without channels and compatible with electrochemical detection under immunoassay conditions,” *Anal Chem*. 82(17) 2010 7068-7072.

[31] E.C. Anderson, M.C. Weston and I. Fritsch. “Investigations of redox magnetohydrodynamic fluid flow at microelectrode arrays using microbeads,” *Anal. Chem*. 82(7) 2010 2643-2651.

[32] S. Qian, and H.H Bau. “Magnetohydrodynamic flow of redox electrolyte,” *Physics of Fluids*. 17(6) 2005 067105-067105-12.

[33] C.K. Nash, and I. Fritsch. “Poly(3.4-ethylenedioxythiophene)-modified electrodes for microfluidics pumping with redox-magnetohydrodynamics (MHD): improving compatibility for broader applications by eliminating addition of redox species to solution,” *Anal. Chem*. 2016 88(3) 1601-1609.

[34] Y. Long, M. Li, C. Gu, M. Wan, J. Duvail, Z. Liu, and Z. Fan. “Recent advances in synthesis physical properties and applications of conducting polymer nanotubes and nanofibers,” *Progress in Polymer Sci*. 36(10) 2011 1415-1442.

[35] Q. Yang, S. Pang, and K. Yung. “Study of PEDOT-PSS in carbon nanotube/conducting polymer composites as supercapacitor electrodes in aqueous solution,” *Journal of Electroanalytical Chemistry*. 728 2014 140-147.

[36] G.A. Snook, P. Kao, and A.S. Best. “Conducting-polymer-based supercapacitor devices and electrodes,” *Journal of power sources*. 196(1) 2011 1-12.

[37] L. Groenendall, F. Jonas, D. Freitag, H. Pielartzik, and J.R. Reynolds. “Poly(3.4-ethylenedioxythiophene) and its derivatives: past, present and future,” *Advanced Materials*. 12 2000 481-494.

[38] J. Heinze, B.A. Frontana-Uribe, and S. Ludwigs. “Electrochemistry of conducting polymers-persistent models and new concepts,” *Chem. Rev*. 110 2010 4724-4771.

[39] E. Laviron. “A multilayer model for the study of space distributed redox modified electrodes,” *Journal of Electroanalytical Chemistry and Interfacial Electrochemistry*. 112(1) 1980 1-9.

[40] T. Yeu, T.V. Nguyen, and R.E. White. “A mathematical model for predicting cyclic voltammograms of electronically conductive polypyrrole,” *Journal of the Electrochemical Society*. 1998 1971-1976.

[41] T.F. Otero, H. Grande, and J. Rodriquez. “Role of conformational relaxation on the voltammetric behavior of polypyrrole experiments and mathematical model,” *J. Phys. Chem. B.* 101 1997 8525-8533.

[42] T. Shoa, D.S. Yoo, K. Walus, and D.W. Madden. “A Dynamic Electromechanical Model for Electrochemically Driven Conducting polymer Actuators,” *IEEE/ASME Transaction Mechatronics*. 16(1) 2011.

[43] S.W. Feldberg. “Effect of uncompensated resistance on the cyclic voltammetric response of an electrochemically reversible surface-attached redox couple: uniform current and potential across the electrode surface,” *Journal of Electroanalytical Chemistry*. 624 2008 45-51.

[44] J. Bobacka, A. Lewenstam, and A. Ivaska. “Electrochemical impedance spectroscopy of oxidized poly (3,4-ethylenedioxythiophene) film electrodes in aqueous solutions,” *Journal of electroanalytical chemistry*. 489 2000 17-27.

[45] A.J. Bard, and L.R. Faulkner. *Electrochemical Methods Fundamentals and Applications*, 2nd edition, John Wiley & Sons, New York, USA, 2001.

[46] ANSYS FLUENT13.0 User's Guide Release 13.0, ANSYS, Inc.® 2011.

[47] Bai. X, Isaac, K.M., Banerjee, R. Klein, D. Breig, W. Oliver, L. “Modeling and simulation of n-butane adsorption/desorption in a carbon canister,” *SAE World Congress*. 2004-01-1680.

[48] Banerjee, R, Isaac. K.M. “An algorithm to determine mass transfer rate form a pure liquid surface using VOF multiphase model,” *Int J Engine Res*. *5*(1) 2004 23-37.

[49] Janakiraman. A, Isaac. K.M, Whitefield. P, Hagan. D. “A numerical thermophoretic model for nanoparticle deposition in an aerosol sampling probe,” In: 17th computational fluid dynamics conference procedings, AIAA, Toronto, Canada, June 6-9, 2005; AIAA, 2005-5351.

[50] G. Li, and P.G. Pickup. “Ion transport in poly(3,4-ethylenedioxythiophene)-poly(styrene-4-sulfonate,” *Phys. Chem. Chem. Phys*. 2 2000 1255-1260.

[51] N. Yang, and C.G. Zoski. “Polymer Films on Electrodes: Investigation of Ion Transport at Poly(3,4-ethylenedioxythiophene) films by Scanning Electrochemical Microscopy,” *Langmuir*. 22 2006 10338-10347.

VITA

Fangping Yuan was born in Shanghai, China on July 26th, 1987. He received his bachelor degree in Physics from Shanghai University in 2009. In 2013, he received his master degree in Fluid Mechanics from Shanghai Institute of Applied Mathematics and Mechanics. He joined the Mechanical and Aerospace Engineering department at Missouri University of Science and Technology in August 2012 and received his Ph.D. in Aerospace Engineering in December 2016. His research focuses on CFD simulations of microscale transport and electrochemistry, Magnetohydrodyanmics (MHD).